








Impact of massive binary star and cosmic evolution on gravitational wave observations I: black hole–neutron star mergers

Floor S. Broekgaarden ^{1,★} Edo Berger,¹ Coenraad J. Neijssel,^{2,3,4} Alejandro Vigna-Gómez ⁵,
Debatri Chattopadhyay ^{3,6}, Simon Stevenson ^{3,6}, Martyna Chruslinska ⁷, Stephen Justham,^{8,9,10,11}
Selma E. de Mink ^{1,10,11} and Ilya Mandel ^{2,3,4}

¹Center for Astrophysics | Harvard & Smithsonian, 60 Garden Street, Cambridge, MA 02138, USA

²Monash Centre for Astrophysics, School of Physics and Astronomy, Monash University, Clayton, Victoria 3800, Australia

³The ARC Center of Excellence for Gravitational Wave Discovery, OzGrav, Hawthorn VIC 3122, Australia

⁴Birmingham Institute for Gravitational Wave Astronomy and School of Physics and Astronomy, University of Birmingham, Birmingham B15 2TT, UK

⁵DARK, Niels Bohr Institute, University of Copenhagen, Jagtvej 128, DK-2200, Copenhagen, Denmark

⁶Center for Astrophysics and Supercomputing, Swinburne University of Technology, Hawthorn VIC 3122, Australia

⁷Institute of Mathematics, Astrophysics and Particle Physics, Radboud University Nijmegen, PO Box 9010, NL-6500 GL Nijmegen, the Netherlands

⁸School of Astronomy & Space Science, University of the Chinese Academy of Sciences, Beijing 100012, China

⁹National Astronomical Observatories, Chinese Academy of Sciences, Beijing 100012, China

¹⁰Anton Pannekoek Institute for Astronomy and GRAPPA, University of Amsterdam, Postbus 94249, NL-1090 GE Amsterdam, the Netherlands

¹¹Max-Planck-Institut für Astrophysik, Karl-Schwarzschild-Straße 1, D-85741 Garching, Germany

Accepted 2021 September 14. Received 2021 September 13; in original form 2021 March 4

ABSTRACT

Mergers of black hole–neutron star (BHNS) binaries have now been observed by gravitational wave (GW) detectors with the recent announcement of GW200105 and GW200115. Such observations not only provide confirmation that these systems exist but will also give unique insights into the death of massive stars, the evolution of binary systems and their possible association with gamma-ray bursts, r -process enrichment, and kilonovae. Here, we perform binary population synthesis of isolated BHNS systems in order to present their merger rate and characteristics for ground-based GW observatories. We present the results for 420 different model permutations that explore key uncertainties in our assumptions about massive binary star evolution (e.g. mass transfer, common-envelope evolution, supernovae), and the metallicity-specific star formation rate density, and characterize their relative impacts on our predictions. We find intrinsic local BHNS merger rates spanning $\mathcal{R}_m^0 \approx 4\text{--}830 \text{ Gpc}^{-3} \text{ yr}^{-1}$ for our full range of assumptions. This encompasses the rate inferred from recent BHNS GW detections and would yield detection rates of $\mathcal{R}_{\text{det}} \approx 1\text{--}180 \text{ yr}^{-1}$ for a GW network consisting of LIGO, Virgo, and KAGRA at design sensitivity. We find that the binary evolution and metallicity-specific star formation rate density each impacts the predicted merger rates by order $\mathcal{O}(10)$. We also present predictions for the GW-detected BHNS merger properties and find that all 420 model variations predict that $\lesssim 5$ per cent of the BHNS mergers have BH masses $m_{\text{BH}} \gtrsim 18 M_{\odot}$, total masses $m_{\text{tot}} \gtrsim 20 M_{\odot}$, chirp masses $\mathcal{M}_c \gtrsim 5.5 M_{\odot}$, and mass ratios $q_f \gtrsim 12$ or $q_f \lesssim 2$. Moreover, we find that massive NSs with $m_{\text{NS}} > 2 M_{\odot}$ are expected to be commonly detected in BHNS mergers in almost all our model variations. Finally, a wide range of ~ 0 per cent to 70 per cent of the BHNS mergers are predicted to eject mass during the merger. Our results highlight the importance of considering variations in binary evolution and cosmological models when predicting, and eventually evaluating, populations of BHNS mergers.

Key words: (transients:) black hole–neutron star mergers – gravitational waves – stars: evolution.

1 INTRODUCTION

The ground-based gravitational wave (GW) interferometers of the LIGO, Virgo, and KAGRA (LVK) network (Lück et al. 2010; Somiya 2012; Aso et al. 2013; Acernese et al. 2015; LIGO Scientific Collaboration 2015; Dooley et al. 2016) observed GWs from binary black hole (BHBH) and binary neutron star (NSNS) mergers in their first observing runs (Abbott et al. 2019, 2020a, d, 2021b; Zackay et al. 2019a, b; Nitz et al. 2020; Venumadhav et al. 2020). With the recent

announcement of the first two observations of mergers between a black hole and neutron star (BHNS), GW200105, and GW200115 (Abbott et al. 2021d), all three of these GW flavours have now been detected. In addition, the recent GW catalogues (GWTC-2 and GWTC-2.1, Abbott et al. 2021a, b, c) presented several GWs where a BHNS source has not yet been ruled out, including GW190814 (Abbott et al. 2020e; Huang et al. 2020; Zhou, Li & Li 2020), GW190425 (Abbott et al. 2020d; Han et al. 2020; Kyutoku et al. 2020), and the low signal-to-noise candidates GW190426_152155 and GW190917, but none of these candidates present a confident BHNS detection.

The detection of BHNS mergers is of broad interest as they could be used to measure the Hubble constant and other cosmological

* E-mail: fsbroekgaarden@gmail.com

parameters to greater distances than NSNS mergers (Schutz 1986; Nissanke et al. 2010; Cai & Yang 2017; Vitale & Chen 2018; Feeney et al. 2021), may help constrain the neutron star (NS) equation of state (Duez et al. 2010; Lackey et al. 2012; Kawaguchi, Shibata & Tanaka 2020), and may help study the rate of heavy element production (Goriely, Bauswein & Janka 2011; Just et al. 2015). In addition, they are theorized to be r -process enrichment sites (e.g. Lattimer & Schramm 1974, 1976; Rosswog et al. 1999; Freiburghaus, Rosswog & Thielemann 1999) and are possibly accompanied by electromagnetic counterparts such as kilonovae (e.g. Li & Paczyński 1998; Barnes & Kasen 2013; Metzger 2017; Zhu et al. 2020), short gamma-ray bursts (e.g. Blinnikov et al. 1984; Goodman 1986; Paczynski 1986; Eichler et al. 1989; Gompertz, Levan & Tanvir 2020), radio emission (Nakar & Piran 2011; Piran, Nakar & Rosswog 2013; Hotokezaka & Piran 2015; Hotokezaka et al. 2016), and neutrinos (Deaton et al. 2013; Kyutoku et al. 2018). By having a plethora of possible observational signatures (see e.g. Metzger & Berger 2012; Pannarale & Ohme 2014; Bhattacharya, Kumar & Smoot 2019), BHNS mergers provide an interesting class of sources for multimessenger astronomy. On the other hand, despite the possibility of observing the NSs in BHNS as Galactic radio pulsars, no such systems are known at present, which may indicate the relative rarity of systems or selection effects that make their detection unlikely unless the NS was formed first and recycled by accretion from the black hole’s progenitor (Chattopadhyay et al. 2020). Meanwhile, some short gamma-ray bursts may have originated from BHNS mergers (e.g. Troja et al. 2008; Gompertz et al. 2020), but there are no consensus sources at present.

The main formation pathway leading to BHNS mergers is under debate, but the favoured scenario is that they form from two massive stars that are born in a binary and evolve in isolation, typically involving a common envelope (CE) episode that tightens the binary orbit (Smarr & Blandford 1976; Srinivasan 1989). This channel can explain the majority of current BHBH and NSNS mergers detected with GWs (e.g. Mapelli & Giacobbo 2018; Wysocki et al. 2018; Neijssel et al. 2019; Olejak et al. 2020; Santoliquido et al. 2020). A popular alternative formation pathway is through dynamical interactions in globular clusters (e.g. Portegies Zwart & McMillan 2000; Sigurdsson 2003; Downing et al. 2010; Clausen, Sigurdsson & Chernoff 2013; Clausen, Sigurdsson & Chernoff 2014; Rodriguez, Chatterjee & Rasio 2016; Kasen et al. 2017) or young stellar clusters (e.g. Ziosi et al. 2014; Mapelli 2016; Rastello et al. 2020; Santoliquido et al. 2020), but recent work suggests that the predicted BHNS merger rate from these channels might be low ($\lesssim 10 \text{ Gpc}^{-3} \text{ yr}^{-1}$) (Bae, Kim & Lee 2014; Ziosi et al. 2014; Mapelli 2016; Fragione, Pavlík & Banerjee 2018; Ye et al. 2019, 2020; Arca Sedda 2020; Fragione & Banerjee 2020; Hoang, Naoz & Kremer 2020; Samsing & Hotokezaka 2020; Banerjee 2021), although Arca Sedda (2021), Rastello et al. (2020), and Santoliquido et al. (2020) predict BHNS merger rates similar to the rates from isolated binary evolution for dynamical interactions in young stellar clusters.

Other formation channels include isolated (hierarchical) triple (or quadruple) evolution involving Kozai–Lidov oscillations (Silsbee & Tremaine 2017; Fragione & Loeb 2019a, b; Hamers & Thompson 2019; Stephan et al. 2019), isolated binary evolution where one star evolves chemically homogeneously through efficient rotational mixing (Mandel & de Mink 2016; Marchant et al. 2017), population III stars (Belczynski et al. 2017), and formation in (active) galactic nucleus discs (O’Leary, Kocsis & Loeb 2009; Fragione et al. 2019; McKernan, Ford & O’Shaughnessy 2020; Yang et al. 2020). More exotic channels have also been suggested such as formation from primordial black holes (Capela, Pshirkov & Tinyakov

2013; Pani & Loeb 2014) or mirror dark matter particles (Beradze, Gogberashvili & Sakharov 2020). Future GW observations will distinguish between formation channels (e.g. Mandel & O’Shaughnessy 2010; Stevenson, Berry & Mandel 2017b; Farr et al. 2017; Vitale et al. 2017; Zevin et al. 2020a). Here, we focus on the formation of BHNS mergers from the isolated binary evolution channel.

The formation of BHNS mergers through isolated binary evolution has been studied with population synthesis simulations for decades (e.g. Tutukov & Yungelson 1993b; Fryer, Woosley & Hartmann 1999; Voss & Tauris 2003; Dominik et al. 2015; Giacobbo & Mapelli 2018; Kruckow et al. 2018; Neijssel et al. 2019; Belczynski et al. 2020), but their predicted rates are still uncertain to several orders of magnitude (Abadie et al. 2010; Mandel & Broekgaarden 2021). This uncertainty has already been shown to come from two main factors. First, from uncertain physical processes in massive (binary)-star evolution such as the CE phase, mass transfer efficiency and supernovae (SNe) natal kicks (e.g. Kruckow et al. 2018; Bavera et al. 2021; Belczynski et al. 2021; Bouffanaïs et al. 2021). Secondly, from uncertainties in the star formation history and metallicity distribution of star-forming gas over cosmic time (e.g. Chruslinska & Nelemans 2019; Neijssel et al. 2019; Tang et al. 2020; Santoliquido et al. 2021), which we will refer to as the metallicity specific star formation rate density, the SFRD (Z_i, z), which is a function of birth (initial) metallicity Z_i and redshift z .

To make the most of future comparisons between observations and simulations of BHNS mergers, it is crucial to explore the uncertainties from both the assumptions for the massive (binary) evolution and SFRD(Z_i, z), in order to make predictions for the BHNS merger rate and characteristics. In turn, the population properties (e.g. the distributions of masses and mass ratios) can be used to make predictions for, e.g. the fraction of BHNS mergers with a possible electromagnetic counterpart. However, previous studies typically focus on exploring only one of the two uncertainties, making it challenging to understand how the massive (binary) evolution and SFRD(Z_i, z) combined impact the results. In addition, studies often focus on presenting results for BHBH or NSNS mergers as these double compact object (DCO) binaries have been observed longer and are more numerous and because BHNS mergers are typically a rare outcome in binary population synthesis models, making simulating a statistically significant population of BHNS systems computationally challenging (e.g. Barrett et al. 2017; Andrews, Zezas & Fragos 2018; Taylor & Gerosa 2018; Broekgaarden et al. 2019; Wong & Gerosa 2019).

In this paper, we therefore focus on making predictions for BHNS mergers and exploring the uncertainties from both varying assumptions for the massive (binary) evolution and SFRD(Z_i, z). We increase the efficiency of our simulations for BHNS mergers by a factor of ~ 100 compared with typical simulations that use sampling from the initial conditions, using the adaptive importance sampling algorithm STROOPWAFEL (Broekgaarden et al. 2019). By doing so, we can run simulations with high resolutions in metallicity (using 53 metallicity bins) and create catalogues with many BHNS sources.

We investigate a total of 420 models, which are combinations of 15 different binary population synthesis model settings and 28 SFRD(Z_i, z) prescriptions, to model these uncertainties. Using these explorations, we address the two main questions: (1) What are the expected properties of BHNS mergers? and (2) How do the uncertainties from both massive (binary) evolution and SFRD(Z_i, z) impact the predicted BHNS merger rates and properties?

The method is described in Section 2. We discuss the formation channels leading to BHNS mergers and their characteristics for both the intrinsic (merging at redshift zero) and GW detectable

population for our fiducial simulation assumptions in Section 3. We discuss how these predictions change for a set of 420 variations in both population synthesis model assumptions and SFRD(Z_i , z) assumptions in Section 4. We end with a discussion in Section 5 and present our conclusions in Section 6.

All data produced in this study are publicly available on Zenodo at <https://doi.org/10.5281/zenodo.4574727>. All code, scripts, and files to reproduce all figures and results in this paper are publicly available in the Github repository <https://github.com/FloorBroekgaarden/BlackHole-NeutronStar>. We present a comparison of our BHNS results to similar predictions for BHBH and NSNS mergers in an accompanying paper (Broekgaarden et al., in preparation).

2 METHOD

2.1 Population synthesis model setup

To evolve a population of binary systems, we use the rapid binary population synthesis code from the COMPAS¹ suite (Stevenson et al. 2017a; Barrett et al. 2018; Vigna-Gómez et al. 2018; Broekgaarden et al. 2019; Neijssel et al. 2019). The main methodology of the binary population synthesis code in COMPAS is built on algorithms developed by Whyte & Eggleton (1985), Dewey & Cordes (1987), and Lipunov & Postnov (1987), and later work by Tout et al. (1997). For single-star evolution (SSE), COMPAS uses the analytic fitting formulae by Hurley, Pols & Tout (2000) and Hurley, Tout & Pols (2002), which are based on SSE tables presented by Pols, Hurley & Tout (1998) and earlier work from Eggleton, Fitchett & Tout (1989) and Tout et al. (1996). The stellar evolution and binary interactions are incorporated through parametrized and approximate prescriptions of the physical processes. By doing so, COMPAS can typically compute an outcome of a binary system in under a second. COMPAS is described in the COMPAS method paper (Team COMPAS 2021, from hereon C21). We describe below the most relevant assumptions and the settings of our fiducial population synthesis model, which are also summarized in Table 1.

2.1.1 Initial distribution functions and sampling method

Each binary system in our simulation can be described at birth (on the zero-age main sequence, ZAMS) by its initial component masses, separation, eccentricity, and metallicity. During the simulation, random birth parameter values are drawn for each binary from distributions whose shape is based on observations that are described below. We assume that the initial parameter distributions are independent of each other. Although this might not be valid (Duchêne & Kraus 2013; Moe & Di Stefano 2017), this likely introduces only a small uncertainty (Abt, Gomez & Levy 1990; Klencki et al. 2018).

We assume that the mass of the initially most massive star in the binary system (the primary) $m_{1,i}$ follows a Kroupa (2001) initial mass function (IMF) with distribution function $p(m_{1,i}) \propto m_{1,i}^{-\alpha}$ with $\alpha = 2.3$, with masses $m_{1,i} \in [5, 150] M_{\odot}$, where the lower limit is chosen as stars below this mass typically do not form NSs and the $150 M_{\odot}$ is based on the typical maximum observed mass of stars. The mass of the secondary is chosen by drawing a mass ratio between the two stars $q_i \equiv m_{2,i}/m_{1,i}$, which is assumed to follow a flat distribution on $[0, 1]$ (cf. Tout 1991; Mazeh et al. 1992; Goldberg & Mazeh

1994; Kobulnicky & Fryer 2007; Sana et al. 2012; Kobulnicky et al. 2014). We set a minimum secondary mass of $m_{2,i} \geq 0.1 M_{\odot}$, the approximate minimal mass for a main-sequence star (Hayashi & Nakano 1963). The initial separation is assumed to follow a flat in the log distribution $p(a_i) \propto 1/a_i$, with $a_i \in [0.01, 1000]$ AU (Öpik 1924; Abt 1983; Duchêne & Kraus 2013), where the lower limit is chosen as stars closer than 0.01 AU typically touch on the ZAMS and the upper limit is chosen as we assume that wider binaries are single stars. We reject and resample binaries that are drawn with such small separations that there is mass transfer at birth, as we assume that those binaries merge as stars and are not included in the population of binaries. We assume that all binaries are circular at birth ($e_i = 0$) to reduce the dimensions of our parameter space; de Mink & Belczynski (2015) showed that this assumption is likely not critical for predictions of BHNS mergers. In addition, close binaries are expected to circularize by the time they have reached their first mass transfer episode (cf. Counselman 1973; Zahn 1977, 2008; Verbunt & Phinney 1995), although see e.g. Vigna-Gómez et al. (2020). Since this study focuses on post-mass transfer binaries, we expect that starting with circular orbits does not significantly influence our outcomes.

The birth metallicities of the stars are varied by using a grid of 53 different initial fractional metallicities Z_i in the range $[0.0001, 0.03]$, which matches the metallicity range of the stellar models by Pols et al. (1998). We define the fractional metallicity Z as the mass fraction of metals such that $X + Y + Z = 1$ with X and Y the mass fractions of hydrogen and helium, respectively. The Z_i grid points are roughly uniformly distributed in $\log(-Z_i)$ space.² For each grid point Z_i , we draw using Monte Carlo $\approx 10^6$ initial binaries using the adaptive importance sampling algorithm STROOPWAFEL (Broekgaarden et al. 2019). This algorithm improves our efficiency of sampling the rare astrophysical outcome of BHNS binaries (and NSNS and BHBH) in population synthesis simulations by a factor of about 100 with respect to traditional Monte Carlo sampling from the birth distributions within these initial ranges.

We assume all stars to initially be non-rotating (see e.g. de Mink et al. 2013 for more details).

2.1.2 Physical assumptions in the binary population synthesis model

We summarize our most important binary population synthesis model assumptions below and in Table 1. Our fiducial model has label A, and all 15 different binary population synthesis models studied in this paper are summarized in Table 2. More details about the modelling in COMPAS are given in C21.

For hydrogen-rich stars, we implement the mass loss rates for line-driven stellar winds from Vink et al. (2000, 2001) as implemented by Belczynski et al. (2010a, see their equations 6 and 7). This includes applying an additional wind mass loss of $f_{LBV} \cdot 10^{-4} M_{\odot} \text{ yr}^{-1}$ independent of metallicity to mimic the effect of luminous blue variable (LBV) winds for stars crossing the Humphreys & Davidson (1994) limit. We adopt the default $f_{LBV} = 1.5$ from Belczynski et al. (2010a). For hydrogen-poor stars (which can be observed as Wolf-Rayet stars, Crowther 2007), we use the stellar wind prescription from Belczynski et al. (2010b).

We distinguish in this paper between three different cases of mass transfer depending on the stellar phase of the donor star (based on Kippenhahn & Weigert 1967; Lauterborn 1970). Case A is when

¹Compact Object Mergers: Population Astrophysics and Statistics, <https://compas.science>

²See the scatter points in Fig. 5 for the exact grid of metallicities.

Table 1. Initial values and default settings of the population synthesis simulation with COMPAS for our fiducial model A. More details can be found in Section 2.1.2 and in the COMPAS method paper C21. Cyan star symbols in front of a row indicate prescriptions that we vary. These variations are listed in Table 2. A (overleaf) latex template for this table that is available for public use can be found at <https://github.com/FloorBroekgaarden/templateForTableBPSsettings>.

Description and name	Value/range	Note/setting
Initial conditions		
Initial mass $m_{1,i}$	[5, 150] M_{\odot}	Kroupa (2001) IMF $\propto m_{1,i}^{-\alpha}$ with $\alpha_{\text{IMF}} = 2.3$ for stars above $5 M_{\odot}$
Initial mass ratio $q_i = m_{2,i}/m_{1,i}$	[0, 1]	We assume a flat mass ratio distribution $p(q_i) \propto 1$ with $m_{2,i} \geq 0.1 M_{\odot}$
Initial separation a_i	[0.01, 1000] AU	Distributed flat-in-log $p(a_i) \propto 1/a_i$
Initial metallicity Z_i	[0.0001, 0.03]	Distributed using a uniform grid in log (Z_i) with 53 metallicities
Initial orbital eccentricity e_i	0	All binaries are assumed to be circular at birth
Fiducial parameter settings:		
Stellar winds for hydrogen-rich stars	Belczynski et al. (2010a)	Based on Vink, de Koter & Lamers (2000), and Vink, de Koter & Lamers (2001), including LBV wind mass loss with $f_{\text{LBV}} = 1.5$.
Stellar winds for hydrogen-poor helium stars	Belczynski et al. (2010b)	Based on Hamann & Koesterke (1998) and Vink & de Koter 2005.
Max transfer stability criteria	ζ -prescription	Based on Vigna-Gómez et al. (2018) and references therein
* Mass transfer accretion rate	Thermal time-scale	Limited by thermal time-scale for stars: Vigna-Gómez et al. (2018); Vinciguerra et al. (2020)
	Eddington-limited	Accretion rate is Eddington-limit for compact objects
Non-conservative mass loss	Isotropic re-emission	Mashevitch & Yungelson (1975); Bhattacharya & van den Heuvel (1991); Soberman, Phinney & van den Heuvel (1997)
		Tauris & van den Heuvel (2006)
* Case BB mass transfer stability	Always stable	Based on Tauris, Langer & Podsiadlowski (2015), Tauris et al. (2017), and Vigna-Gómez et al. (2018)
CE prescription	$\alpha - \lambda$	Based on Webbink (1984) and de Kool (1990)
* CE efficiency α -parameter	1.0	
CE λ -parameter	λ_{Nanjing}	Based on Xu & Li (2010a), Xu & Li (2010b), and Dominik et al. (2012)
* Hertzsprung gap (HG) donor in CE	Pessimistic	Defined in Dominik et al. (2012): HG donors do not survive a CE phase
SNe natal kick magnitude v_k	[0, ∞) km s^{-1}	Drawn from Maxwellian distribution with standard deviation $\sigma_{\text{rms}}^{\text{ID}}$
SNe natal kick polar angle θ_k	[0, π]	$p(\theta_k) = \sin(\theta_k)/2$
SNe natal kick azimuthal angle ϕ_k	[0, 2π]	Uniform $p(\phi) = 1/(2\pi)$
SNe mean anomaly of the orbit	[0, 2π]	Uniformly distributed
* Core-collapse SNe remnant mass prescription	Delayed	From (Fryer et al. 2012), which has no lower black hole (BH) mass gap
* USSN remnant mass prescription	Delayed	From (Fryer et al. 2012)
ECSN remnant mass prescription	$m_f = 1.26 M_{\odot}$	Based on equation (8) in Timmes, Woosley & Weaver (1996)
* Core-collapse SNe velocity dispersion $\sigma_{\text{rms}}^{\text{ID}}$	265 km s^{-1}	1D rms value based on Hobbs et al. (2005)
USSN and ECSN velocity dispersion $\sigma_{\text{rms}}^{\text{ID}}$	30 km s^{-1}	1D rms value based on, e.g. Pfahl, Rappaport & Podsiadlowski (2002) and Podsiadlowski et al. (2004)
* PISN/PPISN remnant mass prescription	Marchant et al. (2019)	As implemented in Stevenson et al. (2019)
* Maximum NS mass	max $m_{\text{NS}} = 2.5 M_{\odot}$	
Tides and rotation		We do not include prescriptions for tides and/or rotation
Simulation settings		
Total number of binaries sampled per metallicity	$\approx 10^6$	We simulate about a million binaries per Z_i grid point
Sampling method	STROOPWAFEL	Adaptive importance sampling from Broekgaarden et al. (2019).
Binary fraction	$f_{\text{bin}} = 1$	Corrected factor to be consistent with, e.g. Sana (2017)
Solar metallicity Z_{\odot}	$Z_{\odot} = 0.0142$	Based on Asplund et al. (2009)
Binary population synthesis code	COMPAS	Stevenson et al. (2017a), Barrett et al. (2018), Vigna-Gómez et al. (2018), and Neijssel et al. (2019) Broekgaarden et al. (2019).

Table 2. List of the 15 binary population synthesis models studied in this work. μ and ‘Label’ denote the alphabetical letter and abbreviated name used to label each model, ‘Changed physics’ and ‘Variation’ denote which category of physics and what we changed, respectively. The column #BHNS lists the total number of BHNS systems that merges in a Hubble time across the 53 metallicity bins comprising the given simulation. The fiducial model settings are summarized in Table 1.

μ	Label	Changed physics	Variation	#BHNS*
A	fiducial	–	–	1 525 553
B	$\beta = 0.25$	Mass transfer	Fixed mass transfer efficiency of $\beta = 0.25$	738 537
C	$\beta = 0.5$	Mass transfer	Fixed mass transfer efficiency of $\beta = 0.5$	148 043
D	$\beta = 0.75$	Mass transfer	Fixed mass transfer efficiency of $\beta = 0.75$	118 921
E	unstable case BB	Mass transfer	Case BB mass transfer is assumed to be always unstable	458 667
F	$\alpha = 0.5$	CE	CE efficiency parameter $\alpha = 0.5$	915 179
G	$\alpha = 2$	CE	CE efficiency parameter $\alpha = 2$	833 433
H	optimistic CE	CE	HG donor stars initiating a CE survive CE	1 535 042
I	rapid SN	SN	Fryer rapid SNe remnant mass prescription	2 766 298
J	max $m_{\text{NS}} = 2 M_{\odot}$	SN	Maximum NS mass is fixed to $2 M_{\odot}$	959 796
K	max $m_{\text{NS}} = 3 M_{\odot}$	SN	Maximum NS mass is fixed to $3 M_{\odot}$	1 990 330
L	no PISN	SN	We do not implement PISN and pulsational-PISN	1 524 497
M	$\sigma_{\text{cc}} = 100$	SN	$\sigma_{\text{rms}}^{\text{ID}} = 100 \text{ km s}^{-1}$ for core-collapse SNe	3 049 458
N	$\sigma_{\text{cc}} = 30$	SN	$\sigma_{\text{rms}}^{\text{ID}} = 30 \text{ km s}^{-1}$ for core-collapse SNe	4 198 238
O	$v_k, \text{BH} = 0$	SN	We assume BHs receive no natal kick	5 068 628

mass transfer is initiated from a main-sequence donor (during core hydrogen burning), case B for hydrogen-shell burning or core-helium burning donors, and case C for post-core helium burning donors. In addition, we use case BA, case BB, and case BC analogues for the A, B, and C mass transfer cases from a stripped or helium donor star (cf. De Greve & De Loore 1977; Delgado & Thomas 1981; Tutukov & Yungel’Son 1993a).

We use the ζ -prescription to determine the stability of mass transfer, which compares the radial response of the donor star with the response of the Roche lobe radius to mass transfer (Vigna-Gómez et al. 2018; Vinciguerra et al. 2020, C21 and references therein). The mass transfer efficiency describes the fraction of the mass lost by the donor that is accreted by the companion star, $\beta = \Delta M_{\text{acc}}/\Delta M_{\text{donor}}$, where ΔM_{donor} and ΔM_{acc} are the change in mass by the donor and accretor star over time, respectively. The time-scale and amount of donated mass are set by the stellar type of the donor star. We assume for our fiducial model that the maximum accretion rate for stars is $\Delta M_{\text{acc}}/dt = 10M_{\text{acc}}/\tau_{\text{KH}}$, similar to Hurley et al. (2002), with t the time, τ_{KH} the Kelvin–Helmholtz (thermal) time-scale of the star, and the factor of 10 is added to take into account the expansion of the accretor due to mass transfer (Paczyński & Sienkiewicz 1972; Hurley et al. 2002; Schneider et al. 2015; Kasen et al. 2017). For compact objects, we assume that the maximum mass accretion rate is Eddington-limited; this assumption likely does not impact our result (van Son et al. 2020). If more mass is transferred from the donor than can be accreted, we assume that this mass is lost from the vicinity of the accreting star through ‘isotropic re-emission’ (e.g. Masevitch & Yungelson 1975; Bhattacharya & van den Heuvel 1991; Soberman et al. 1997; Tauris & van den Heuvel 2006) and adopt the specific angular momentum accordingly (e.g. Belczynski et al. 2008). In models B, C, and D, we vary the maximum accretion rate of the accreting star by instead setting β to fixed values of $\beta = 0.25, 0.5,$ and $0.75,$ respectively.

We assume for our fiducial model that a mass transfer phase from a stripped post-helium-burning star (case BB) on to an NS or BH is always stable as suggested by Tauris et al. (2015, 2017). Vigna-Gómez et al. (2018) show that this assumption leads to a better match of population synthesis models to the observed population of Galactic NSNS binaries. We vary this in model E, where we assume case BB mass transfer to always be unstable (Table 2).

We follow the simplified α - λ prescription from Webbink (1984) and de Kool (1990) to parametrize the CE phase. We assume for the α parameter, which regulates the efficiency with which the envelope is ejected, the value $\alpha = 1$ in our fiducial model but vary this to $\alpha = 0.5$ and $\alpha = 2$ in models F and G, respectively (Table 2). A suitable value of α for these simulations is uncertain and challenging to infer from observations and simulations. There may well be no single value of α , which accurately describes the physics in the diverse CE phases experienced by our compact-object progenitors. Population synthesis predictions have suggested that the α value impacts the detectable GW merger rates (e.g. Dominik et al. 2012; Kruckow et al. 2016, 2018; Olejak, Belczynski & Ivanova 2021). For the λ parameter, we use the fitting formulas from Xu & Li (2010a) and Xu & Li (2010b), similar to the λ_{Nanjing} parameter in Dominik et al. (2012), which includes internal energy (λ_{b} as in Xu & Li 2010a, b) and the added models up to $100 M_{\odot}$ ZAMS masses. Similar to Dominik et al. (2012, see their section 2.3.2.), we extrapolate these models up to our maximum mass of $150 M_{\odot}$. In this method, the value of λ depends on the stellar evolutionary stages of the stars (see also Dewi & Tauris 2000; Tauris & Dewi 2001; Kruckow et al. 2016). For more details on the α and λ , see Ivanova et al. (2013) and references therein.

We do not allow hydrogen shell burning (typically Hertzsprung gap) donor stars that initiate a CE event to survive in our fiducial model. These donor stars are not expected to have developed a steep density gradient between core and envelope (Taam & Sandquist 2000; Ivanova & Taam 2004), making it challenging to successfully eject the envelope. Instead, it is thought that a merger takes place, and it has been shown for a few cases that such binaries are unlikely to form a DCO that can form a GW source (Pavlovskii & Ivanova 2015; Pavlovskii et al. 2017). This implementation follows the ‘pessimistic’ CE scenario (cf. Dominik et al. 2012). The ‘optimistic’ CE scenario, on the other hand, assumes that these systems can survive. Which of the scenarios more accurately represent observations is still under debate. Recently, Mapelli et al. (2017) showed that the pessimistic scenario slightly better matches the predicted BHBH rate. Vigna-Gómez et al. (2018) argued that there is no clear evidence to favour one of the scenarios over the other based on a study of Galactic NSNS binaries. We use the pessimistic model for our fiducial assumption, similar to recent population synthesis studies (e.g. Giacobbo & Mapelli 2018; Neijssel et al. 2019; Wiktorowicz et al. 2019), and use the optimistic assumption in model variation H (Table 2). We do allow main-sequence companion stars in a CE event to survive the CE. Lastly, we remove binaries where the secondary star fills its Roche lobe immediately after a CE event, as we treat those events as failed CE ejections. More details of the treatment of CE events in COMPAS are discussed in Vigna-Gómez et al. (2020) and C21.

We use the ‘delayed’ SNe remnant mass prescription (Fryer et al. 2012) to map the carbon–oxygen core masses of stars to compact object remnant masses during core-collapse SNe events.³ We deviate with this choice from most binary population synthesis codes that typically use instead the *rapid* SNe remnant mass prescription for their fiducial model (examples include Klennicki & Nelemans 2019; Breivik et al. 2020, but see e.g. also the discussion in Eldridge et al. 2020 on why this assumption may need to be revisited). We discuss in Section 5.1.1 why we prefer using the delayed remnant mass prescription. The main difference is that the delayed remnant mass prescription does not create, by construction, the remnant mass gap between NSs and BHs that might be apparent from X-ray binary observations (Bailyn et al. 1998; Özel et al. 2010; Farr et al. 2011). We explore changing our model to the rapid remnant mass prescription in model variation I (Table 2).

During the SNe event, a fraction of the ejected material, f_{fb} , is assumed to fall back on to the compact object. We use the prescription from equations (16) and (19) in Fryer et al. (2012) to determine this fraction and adjust the final remnant mass accordingly.

The maximum mass that an NS can have is uncertain and under debate. Observations from pulsars show that most NSs have masses around $\sim 1.3 M_{\odot}$ (e.g. Valentim, Rangel & Horvath 2011; Özel et al. 2012; Kiziltan et al. 2013; Linares 2020) and have found that the most massive NSs to date have masses of $\sim 2\text{--}2.2 M_{\odot}$ (Antoniadis et al. 2013; Cromartie et al. 2020; Farr & Chatziioannou 2020), although more massive NSs might have been observed (e.g. Freire et al. 2008; van Kerkwijk, Breton & Kulkarni 2011, but see the discussion in Özel & Freire 2016 on why these mass measurements

³Previous COMPAS studies included an extra mass gap in the NS mass distribution around $2.2 M_{\odot}$ (see e.g. the middle panel of fig. 7 in Vigna-Gómez et al. 2018 and bottom panels of fig. 7 in Broekgaarden et al. 2019) due to a difference in the assumed relationship between baryonic and gravitational masses for NS and BH remnants. In our corrected treatment, this quirk (see equations 12 and 13 in Fryer et al. 2012) leads to a single gap in the NS mass distribution around $1.7 M_{\odot}$ and a small gap between NS and BH gravitational masses even for the ‘delayed’ remnant mass prescription.

are more uncertain). From observational and theoretical (population) modelling, the possible maximum NS mass has been predicted to lie in the range of $2\text{--}3 M_{\odot}$ (e.g. Kalogera & Baym 1996; Fryer et al. 2015; Lawrence et al. 2015; Margalit & Metzger 2017; Alsing, Silva & Berti 2018; Abbott et al. 2020b, d; Sarin, Lasky & Ashton 2020). We decide to assume for our fiducial model that NSs can have a maximum mass of $2.5 M_{\odot}$. For models J and K, we change this to $2 M_{\odot}$ and $3 M_{\odot}$, respectively. We adopt the Fryer et al. (2012) remnant mass prescription accordingly.

We assume that stars with helium core masses in the range of $1.6\text{--}2.25 M_{\odot}$ (Hurley et al. 2002) lead to electron-capture SNe (ECSNe)⁴ (Miyaji et al. 1980; Nomoto 1984, 1987; Ivanova et al. 2008). If a star undergoes an ECSNe, we set its remnant mass to $1.26 M_{\odot}$, as an approximation to the solution of equation (8) in Timmes et al. (1996).

Case BB mass transfer from a companion star on to an NS or BH in short-period binaries leads to severe stripping (leaving behind an envelope with mass $\lesssim 0.1 M_{\odot}$) and we assume that the stripped star eventually undergoes an ultra-stripped SN (USSNe) as shown by Tauris et al. (2013, 2015), Suwa et al. (2015), Moriya et al. (2017), and Müller et al. (2018). This follows the prescription of the fiducial model of Vigna-Gómez et al. (2018), but we also assume that case BB mass transfer on to a BH leads to an ultra-stripped star and USSNe as suggested by Tauris et al. (2013, 2015), and in agreement with the implementation of USSNe in other binary population synthesis work (e.g. Kruckow et al. 2018; Vinciguerra et al. 2020). We calculate the remnant mass of an ultra-stripped SNe using the delayed Fryer et al. (2012) SNe prescription in our fiducial model.

Stars with helium cores in the range of about $45\text{--}150 M_{\odot}$ are thought to become unstable and undergo a pair-instability SN (PISN) or pulsational-PISN, leading to an absence of BHs with masses in this range as shown from theory (Fowler & Hoyle 1964; Barkat, Rakavy & Sack 1967; Woosley 2017; Farmer et al. 2019) and observations (Fishbach & Holz 2017; Talbot & Thrane 2018; Abbott et al. 2019; Roulet & Zaldarriaga 2019; Wysocki, Lange & O’Shaughnessy 2019; Galadage, Talbot & Thrane 2020). BH formation is expected again above a helium core mass of $\sim 150 M_{\odot}$ (Woosley, Heger & Weaver 2002; Woosley 2019; Woosley & Heger 2021). However, this assumption has recently been challenged by the second GW catalogue that contained BHBH merger detections with components with masses $\gtrsim 45 M_{\odot}$ (Abbott et al. 2021b), the most massive being GW190521 (Abbott et al. 2020c). The origin of these massive BHs is still unknown, and one of the current thoughts is that they formed from other channels than the isolated binary evolution channel such as via hierarchical mergers (e.g. Anagnostou, Trenti & Melatos 2020), stellar mergers (e.g. Spera et al. 2019; Di Carlo et al. 2020; Kremer et al. 2020), triples (e.g. Vigna-Gómez et al. 2021b) or in active galactic nucleus (AGN) discs (e.g. Secunda et al. 2020). See for a more detailed discussion, for example, Abbott et al. (2020f) and Kimball et al. (2021) and references therein. We follow the PISN and pulsational PISN prescription from Marchant et al. (2019) as implemented in Stevenson et al. (2019). The mass range of helium cores that undergo PISN is shown to be a robust prediction (Farmer et al. 2019; Renzo et al. 2020) and we do not expect our particular choice for PISN and pulsational PISN prescription to drastically influence our results other than somewhat the location of the gap (e.g. Spera & Mapelli 2017; Stevenson et al. 2019; Farmer et al. 2020; Costa et al. 2021; Woosley & Heger 2021). In model L, we

explore a simulation where we do not implement pulsational PISN and PISN.

NSs and BHs might receive SNe kicks at birth. For core-collapse SNe, we draw these natal kick magnitudes from a Maxwellian velocity distribution with a one-dimensional root-mean-square velocity dispersion of $\sigma_{\text{rms}}^{1D} = 265 \text{ km s}^{-1}$, based on observations of radio pulsar proper motions (Lyne & Lorimer 1994; Hobbs et al. 2005). In models M and N, we explore the variation of lower kicks by using $\sigma_{\text{rms}}^{1D} = 100 \text{ km s}^{-1}$ and $\sigma_{\text{rms}}^{1D} = 30 \text{ km s}^{-1}$, respectively. For USSNe and ECSNe, we use instead a one-dimensional root-mean-square velocity dispersion of $\sigma_{\text{rms}}^{1D} = 30 \text{ km s}^{-1}$ following Pfahl et al. (2002) and Podsiadlowski et al. (2004) as they are thought to have smaller kicks than standard iron core-collapse SNe (e.g. Suwa et al. 2015; Gessner & Janka 2018; Müller et al. 2018). This is in agreement with the subset of Galactic binary NS systems and pulsars observed with low velocities and small eccentricities (Briskin et al. 2002; Schwab, Podsiadlowski & Rappaport 2010; Beniamini & Piran 2016; Tauris et al. 2017; Verbunt & Cator 2017; Verbunt, Igoshev & Cator 2017; Igoshev 2020). Combined, the magnitude of SNe kicks will thus represent a broader, bimodal distribution as supported by Katz (1975), Arzoumanian, Chernoff & Cordes (2002), Verbunt et al. (2017), Kasen et al. (2017), and Igoshev (2020).

We reduce the natal kick using the fallback fraction by a factor $(1 - f_{\text{fb}})$. This typically reduces the natal kicks of BHs with masses above $11 M_{\odot}$ to zero for the delayed SNe prescription. This is in agreement with observations that show evidence that BHs might form with lower or no natal kicks, although this is still under debate (Brandt, Podsiadlowski & Sigurdsson 1995; Nelemans, Tauris & van den Heuvel 1999; Repetto, Davies & Sigurdsson 2012; Janka 2013; Repetto & Nelemans 2015; Mandel 2016). Model O explores a binary population synthesis variation where BHs receive no natal kick (Table 2).

All natal kicks are assumed to be isotropic in the frame of the collapsing star (e.g. Wongwathanarat, Janka & Müller 2013) and we sample the kick polar angles θ_{k} and kick azimuthal angles ϕ_{k} from a unit sphere. The mean anomaly of the orbit is randomly drawn from $[0, 2\pi]$.

The inspiral time-scale, t_{inspiral} , as a result from orbital energy lost in GWs is based on Peters (1964).

2.1.3 The formation, evolution, inspiral, and delay times

The time at which a DCO merges, t_{m} , is given by $t_{\text{m}} = t_{\text{form}} + t_{\text{evolve}} + t_{\text{inspiral}}$, shown in Fig. 1, with t_{form} the time at which the initial binary forms from a gas cloud and starts hydrogen burning since the beginning of star formation in the Universe, t_{evolve} the time it takes the binary from the onset of hydrogen burning at ZAMS to form a DCO (i.e. until the second SN), and t_{inspiral} the time it takes the DCO to coalesce from the moment of the second SNe. The formation and inspiral time together form the delay time $t_{\text{delay}} = t_{\text{evolve}} + t_{\text{inspiral}}$.

2.1.4 Initializing a population of BHNS mergers

For each binary population synthesis model, we evolve a population of about 10^6 binary systems per metallicity Z_i from birth until they form a DCO binary or otherwise merge or disrupt. From the population of DCO binaries, we select the BHNS systems. We also select only binaries that merge in a Hubble time (i.e. that have $t_{\text{delay}} \leq t_{\mathcal{H}}$, with $t_{\mathcal{H}} = \mathcal{H}_0^{-1} \approx 14 \text{ Gyr}$; cf. the WMAP9–cosmology, Hinshaw et al. 2013). We assume that BHNS systems with merger

⁴Lower core masses will lead to the formation of white dwarfs.

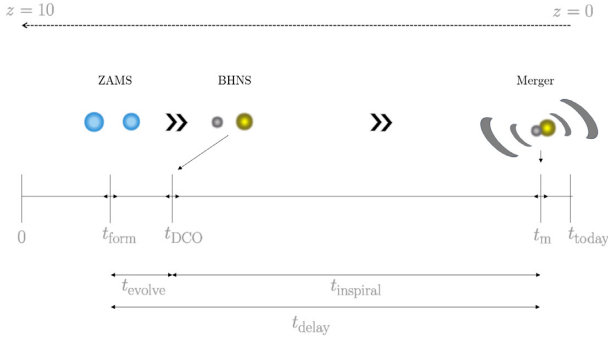


Figure 1. Schematic display of the different times in the formation and evolution of a binary system that impact the time t_m at which a BHNS system will merge in the Universe. The relevant time-scales are: the moment the binary is formed at ZAMS from a gas cloud, t_{form} , the moment of the DCO formation, t_{DCO} , the time at which the merger takes place, t_m , the time it takes the binary to evolve from ZAMS to the DCO system, $t_{\text{evolve}} = t_{\text{DCO}} - t_{\text{form}}$, the inspiral time, $t_{\text{inspiral}} = t_m - t_{\text{DCO}}$, and the time between binary formation at ZAMS and merger, $t_{\text{delay}} = t_m - t_{\text{form}}$. We assume in our models that star formation commenced at redshift $z = 10$.

times exceeding $t_{\mathcal{H}}$ will not be detectable by GW detectors (in the near future).

We use COMPAS to calculate and record properties such as the ages, masses, stellar radii, effective temperatures, velocities, eccentricities, and separations of the binary at important evolutionary stages of the binary such as mass transfer episodes and SNe. COMPAS also records t_{evolve} and t_{inspiral} for each BHNS system.

Throughout the rest of the paper, we will use the notation BHNS for binaries containing a BH and an NS. The notation BH–NS (NS–BH) will be used when we explicitly refer to a BHNS binary where the BH (NS) formed in the first SNe. The formation order is particularly important for spinning up the BH or NS and the formation of millisecond pulsars (discussed in Section 2.6).

2.2 Calculating the BHNS formation rate per unit star-forming mass

We model only a small fraction of the underlying stellar population by neglecting single stars, not simulating binaries with primary star masses below $5 M_{\odot}$, and not drawing binaries from their initial birth distributions. To calculate the BHNS formation rate, we therefore re-normalize our results to obtain a formation rate of BHNS mergers for a given metallicity Z_i per unit star-forming mass, i.e. $dN_{\text{form}}/dM_{\text{SFR}}$, and calculate the formation rate for BHNS mergers with a given delay time and final compact object masses, $m_{1,f}$ and $m_{2,f}$, in COMPAS with

$$\mathcal{R}_{\text{form}}(Z_i, t_{\text{delay}}, m_{1,f}, m_{2,f}) = \frac{d^4 N_{\text{form}}}{dM_{\text{SFR}} dt_{\text{delay}} dm_{1,f} dm_{2,f}}(Z_i, t_{\text{delay}}, m_{1,f}, m_{2,f}). \quad (1)$$

We calculate this re-normalized formation rate by incorporating the STROOPWAFEL weights and assuming a fixed binary fraction of $f_{\text{bin}} = 1$, which is consistent with the observed intrinsic binary fraction for O-stars of ~ 0.6 – 0.7 (Sana & Evans 2011; Sana et al. 2012; Dunstall et al. 2015; Almeida et al. 2017; Sana 2017), when extrapolating for the wider separation range used in this study compared with the observational surveys (cf. de Mink & Belczynski 2015). Changing f_{bin} to 0.7 did not substantially impact our results.

2.3 Calculating the cosmological BHNS merger rate

To make predictions for the GWs that can be detected with the LVK network today, it is important to consider BHNS that formed across a large range of metallicities and redshifts in our Universe. This is because BHNS systems form from their initial stars in several million years, but their inspiral times can span many Gyr (e.g. Tutukov & Yungelson 1994; Belczynski, Kalogera & Bulik 2002; Mennekens & Vanbeveren 2016). GWs can, therefore, originate from binaries with long inspiral times that were formed at high redshifts as well as binaries with shorter inspiral times formed at lower redshifts. This is especially the case for GW observations with the ground-based LVK network that has observation horizons beyond > 100 Mpc for DCO mergers (Abbott et al. 2018a). Moreover, the merger rate density of BHNS, and more generally DCOs, can be particularly sensitive to metallicity, which impacts mass loss through stellar winds, the stellar radii (and radial expansion), and thereby the outcome of the (binary) evolution (e.g. Maeder 1992; Eldridge & Stanway 2016; Klencki et al. 2018; Lamberts et al. 2018; Chruslinska, Nelemans & Belczynski 2019). As a result, DCO systems form sometimes much more efficiently at low metallicities ($Z_i \lesssim 0.1 Z_{\odot}$), which increases the importance of DCO formation at high redshifts, where low-metallicity stars are more abundantly formed, when considering the GWs that can be detected today. It is therefore important to take into account the SFRD at different metallicities over the history of our Universe when making predictions for GW observations (Chruslinska et al. 2019).

To calculate the BHNS merger rate density that can be detected with GWs today, we use the method from Neijssel et al. (2019); we first integrate the formation rate density from equation (1) over metallicity and use the relation $t_{\text{form}} = t_m - t_{\text{delay}}$ (Section 2.1.3) to obtain the merger rate for a binary with masses $m_{1,f}$, $m_{2,f}$ at any given merger time, t_m , using

$$\begin{aligned} \mathcal{R}_m(t_m, m_{1,f}, m_{2,f}) &= \frac{d^4 N_{\text{merger}}}{dt_s dV_c dm_{1,f} dm_{2,f}}(t_m, m_{1,f}, m_{2,f}) \\ &= \int dZ_i \int_0^{t_m} dt_{\text{delay}} \text{SFRD}(Z_i, t_{\text{form}} = t_m - t_{\text{delay}}) \times \\ &\quad \mathcal{R}_{\text{form}}(Z_i, t_{\text{delay}}, m_{1,f}, m_{2,f}), \end{aligned} \quad (2)$$

where t_s is the time in the source frame of the merger, V_c is the comoving volume, $\mathcal{R}_{\text{form}}$ is obtained using COMPAS (Section 2.2), and $\text{SFRD}(Z_i, t_{\text{form}}) = \text{SFRD}(Z_i, z(t_{\text{form}}))$. We obtain the $\text{SFRD}(Z_i, z)$ by multiplying an SFRD with a metallicity probability density function

$$\begin{aligned} \text{SFRD}(Z_i, z_{\text{form}}) &= \frac{d^3 M_{\text{SFR}}}{dt_s dV_c dZ_i}(z_{\text{form}}) \\ &= \underbrace{\frac{d^2 M_{\text{SFR}}}{dt_s dV_c}(z_{\text{form}})}_{\text{SFRD}} \times \underbrace{\frac{dP}{dZ_i}(z_{\text{form}})}_{\text{GSMF} + \text{MZR}}, \end{aligned} \quad (3)$$

where we wrote down the equations in z , and used the short-hand notation $z_{\text{form}} = z(t_{\text{form}})$. We use for the metallicity density function, dP/dZ_i , either a direct analytical formula (e.g. model $\mu = 000$) or, in most cases, a convolution between a galaxy mass function, the number density of galaxies per logarithmic mass bin (GSMF), and mass–metallicity relation (MZR). This is discussed in more detail below and schematically shown in Fig. 2. Throughout our analysis,

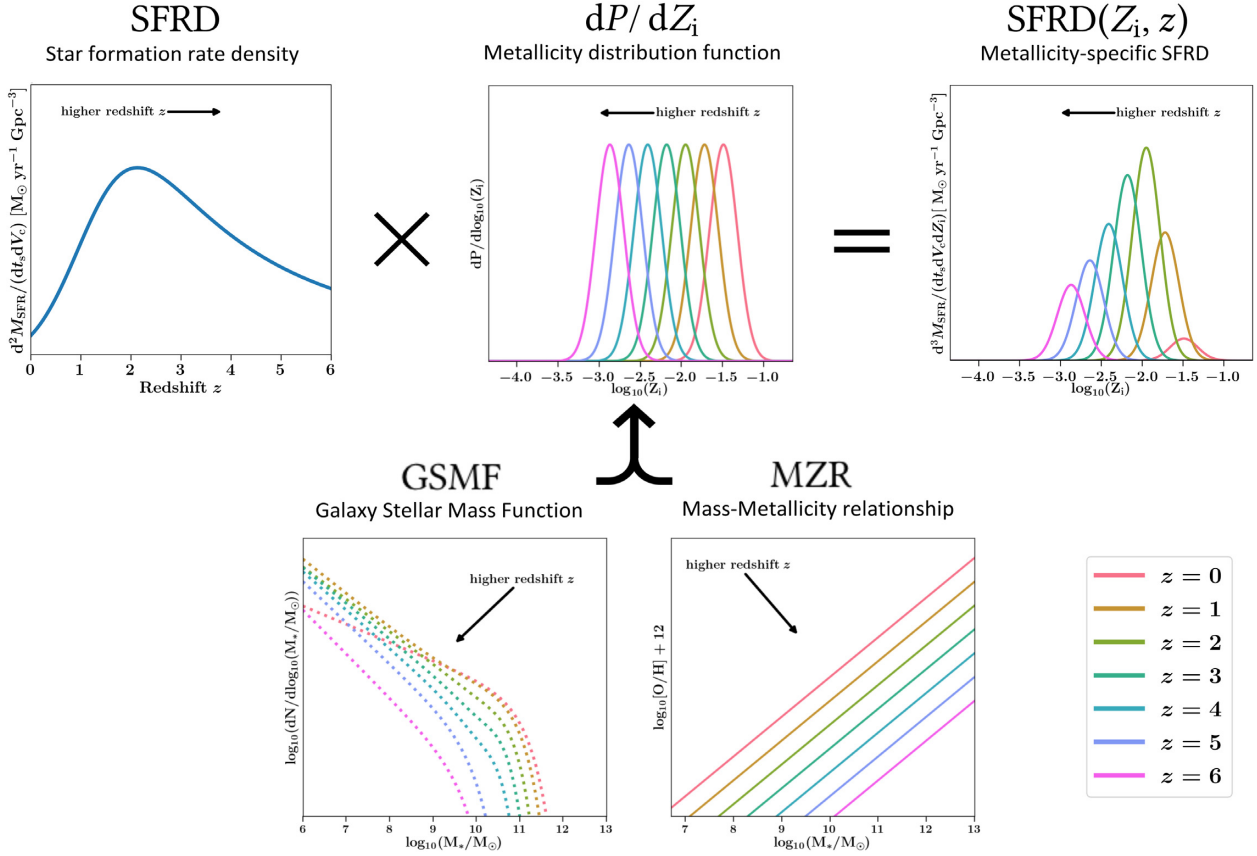


Figure 2. Schematic depiction of how our model for the metallicity specific star formation rate density, metallicity-specific star formation rate density (SFRD)(Z_i, z), is created from multiplying an SFRD with a metallicity probability distribution function, dP/dZ_i . The metallicity distribution function is constructed by convolving a galaxy stellar mass function with a mass–metallicity relationship. An exception is our fiducial SFRD(Z_i, z) model, which uses the ‘preferred’ phenomenological model from Neijssel et al. (2019) for the metallicity distribution function. The arrows in each sub-figure indicate in which direction the distribution moves as redshift increases.

we use the cosmology parameters from the WMAP9 study (Hinshaw et al. 2013).⁵

This merger rate density, \mathcal{R}_m , is then converted to a local detection rate by integrating over the co-moving volume and taking into account the probability, P_{det} , of detecting a GW source (Section 2.5) with

$$\begin{aligned} \mathcal{R}_{\text{det}}(t_{\text{det}}, m_{1,f}, m_{2,f}) &= \frac{d^3 N_{\text{det}}}{dt_{\text{det}} dm_{1,f} dm_{2,f}} \\ &= \int dV_c \frac{dt_s}{dt_{\text{det}}} \mathcal{R}_m(t_m, m_{1,f}, m_{2,f}) P_{\text{det}}(m_{1,f}, m_{2,f}, D_L(z)), \end{aligned} \quad (4)$$

where t_{det} is the time in the detector (i.e. the observer) frame and D_L is the luminosity distance. See Appendix A for more details about the conversion to t_{det} , z and D_L . In practice, we often marginalize in the remaining sections over the masses and redshifts (or equivalent, delay, or merger time) to obtain an overall rate in this equation as well as equation (1). We also calculate the detector rate for where t_{det} is the current age of our Universe.

In practice, the integral in equation (4) is estimated using a Riemann sum over redshift, metallicities, and delay time bins, given in equation (A1). This method is similar to previous work including Dominik et al. (2013, 2015), Belczynski et al. (2016b), Mandel &

de Mink (2016), Barrett et al. (2018), Eldridge, Stanway & Tang (2019), Baibhav et al. (2019), Bavera et al. (2020), and Chruslinska et al. (2019). Details of our method are given in Neijssel et al. (2019) and C21.

2.4 Metallicity-specific star formation rate density prescriptions

We explore the impact on the BHNS merger rate and population characteristics from a total of 28 different SFRD(Z_i, z) models. All our 28 SFRD(Z_i, z) models are constructed by combining analytical, simplified prescriptions for the SFRD and metallicity distribution function (equation 3). A schematic depiction is shown in Fig. 2. Although all models (drastically) simplify the complex behaviour of the SFRD(Z_i, z) as a function of redshift and time, many of the prescriptions explored in this work are widely used in population synthesis predictions for DCO mergers. Our aim in using these models is foremost to explore and study the impact of these uncertainties in current state-of-the-art population synthesis predictions for BHNS mergers. In Section 5.1.3, we discuss in more detail the main limitations and future prospects to this modelling.

Our fiducial SFRD(Z_i, z) model, xyz = 000 (Table 3), is the phenomenological model described in Neijssel et al. (2019) (referred to as the ‘preferred’ model). This model uses a phenomenological analytical model for the SFRD and the metallicity probability distribution function. The latter is directly constructed using a lognormal

⁵Obtained from the astropy cosmology module, which has $\Omega_m = 0.287$, $\Omega_\Lambda^0 = 0.713$ and assumes the flat Lambda–CDM model.

Table 3. List of the assumptions for the metallicity-specific star formation rate, SFRD(Z_i, z), models that we explore in this study. All SFRD(Z_i, z) models except our fiducial model are obtained by combining a star formation rate density (SFRD) with a galaxy stellar mass function (GSMF) and mass–metallicity relation (MZR). See Sections 2.3 and 2.4 for more details. The models are named in the convention xyz with $x, y, z \in [1, 2, 3]$ the index numbers for the models used for the SFRD, GSMF, and MZR, respectively. For example, the combination of using the Madau & Dickinson (2014) SFRD with the Panter et al. (2004) GSMF and Ma et al. (2016) MZR is labelled 113. The fiducial (phenomenological) model is not a specific combination but a parametrized model that is built to be flexible and is fitted to match the GW-detected BHBH rate and chirp mass distribution from the first two runs of LIGO and Virgo (Neijssel et al. 2019). The simulations using the phenomenological SFRD(Z_i, z) model have the label 000.

xyz index	SFRD (x)	GSMF (y)	MZR (z)
000 (fiducial)	Phenomenological model Neijssel et al. (2019)		
1	Madau & Dickinson (2014)	Panter, Heavens & Jimenez (2004)	Langer & Norman (2006)
2	Strolger et al. (2004)	Furlong et al. (2015) single Schechter	Langer & Norman (2006) + offset
3	Madau & Fragos (2017)	Furlong et al. (2015) double Schechter	Ma et al. (2016)

metallicity density distribution with a redshift-independent standard deviation $\sigma = 0.39$ and redshift-dependent mean $\mu(z)$, which follows the work of Langer & Norman (2006). The values of the free parameters in the phenomenological model are found by combining the SFRD(Z_i, z) prescription with a population synthesis outcome to find the best fit to the BHBH GW observations announced in the first two observing runs of LIGO and Virgo (Neijssel et al. 2019). This work is also done with COMPAS using stellar-evolution assumptions that are similar to the ones assumed in this study. We therefore expect the merger rates based on this SFRD(Z_i, z) choice and our fiducial simulations to be representative for the GW observations. The SFRD and the metallicity probability distribution function for this prescription are shown in Figs B1(a) and (b), respectively.

All our other 27 SFRD(Z_i, z) models, on the other hand, use one of the commonly used SFRDs in combination with a probability density function that is created by combining a GSMF with an MZR; these are described below.⁶ The main difference of these models compared to the preferred Neijssel et al. (2019) model is that the former does not assume that the metallicity probability distributions are symmetric in log-metallicity (while the preferred model from Neijssel et al. 2019 does), as can be seen in Fig. B1(b). Observational evidence suggests that this symmetric behaviour is likely not the case (e.g. Langer & Norman 2006; Chruslinska et al. 2019; Boco et al. 2021). Two combinations of the 27 SFRD(Z_i, z) models are shown in Fig. B1(b). By considering all possible combinations of the three SFRD, three GSMF, and three MZR prescriptions, we end up with a total of 27 SFRD(Z_i, z) models in addition to our fiducial SFRD(Z_i, z) model based on Neijssel et al. (2019), resulting in a total of 28 models.

2.4.1 Star formation rate density SFRD

The SFRDs prescriptions are shown in Fig. B1(a). Besides using the phenomenological SFRD from Neijssel et al. (2019) for model 000, we follow Neijssel et al. (2019) and vary between three typically used SFRD prescriptions described in Table 3. First, we use the SFRD from Madau & Dickinson (2014, equation 15), which has a slightly earlier peak compared to the other SFRDs used in this work. Population synthesis studies of DCO merger rates that use this SFRD prescription include Belczynski et al. (2016a), Chruslinska et al. (2018), Baibhav et al. (2019), and Eldridge et al. (2019). Secondly, we use the Strolger et al. (2004) prescription, which assumes a higher extinction correction, resulting in a higher SFRD, particularly

⁶During this convolution, we assume that the SFRD is spread equally among all galaxy stellar mass. Such that a galaxy with twice the amount of mass has twice the SFRD.

at higher redshifts. Population synthesis studies of DCO merger rates that use this SFRD prescription include the works by Dominik et al. (2013), Kowalska-Leszczynska et al. (2015), Belczynski et al. (2017), Cao, Lu & Zhao (2018), and Kruckow et al. (2018). Lastly, we also use the SFRD from Madau & Fragos (2017, equation 1), which is an updated version of Madau & Dickinson (2014) that uses the broken power-law IMF from Kroupa (2001) and better fits some of the observations between redshifts $4 \lesssim z \lesssim 10$. DCO merger rate studies that use this SFRD assumption include Belczynski et al. (2020), Drozda et al. (2020), Wong et al. (2021), and Zevin et al. (2020a).

2.4.2 Galaxy stellar mass function GSMF

Following Neijssel et al. (2019), we vary between three different prescriptions for the GSMF, which are shown in Fig. B1(c). Typically, the GSMF is described with a single or double Schechter (1976) function. First, we use a redshift-independent single Schechter GSMF model as given by Panter et al. (2004). This GSMF prescription is used to create a metallicity distribution function by Langer & Norman (2006), which is used by studies including Barrett et al. (2018) and Marchant et al. (2017). Secondly and thirdly, we use the redshift-dependent single and double Schechter functions based on results from Furlong et al. (2015), respectively. We use the fits by Neijssel et al. (2019) to the tabulated values from Furlong et al. (2015, table A1) that extrapolates to a full redshift range of $z \in [0, 6.5]$. See Neijssel et al. (2019) for more details.

2.4.3 Mass–metallicity relation MZR

We follow Neijssel et al. (2019) for exploring three different MZR prescriptions shown in Fig. B1(d). The metallicity in this figure is shown as the number density of oxygen over that of hydrogen, which is typically observed. The MZR describes the average relation between the typical metallicities found for star-forming galaxies at a given redshift. We use the solar values of $Z_\odot = 0.0142$ and $\log_{10}[\text{O}/\text{H}] + 12 = 8.69$ (Asplund et al. 2009) to convert to mass fraction metallicities. For our first two MZR prescriptions, we use the approximate MZR relation that Langer & Norman (2006) construct based on observations from Savaglio et al. (2005), which is given by $M_*/M_x = (Z_i/Z_\odot)^2$, with M_x as given by Langer & Norman (2006) and M_* the galaxy stellar mass. We assume the average metallicity scales with redshift as $\langle Z_i \rangle = Z_\odot 10^{-0.3z}$. Following Neijssel et al. (2019), we create a second prescription based on these two relations by adding an offset to better match the quadratic fit given in Savaglio et al. (2005). As third MZR model, we use the MZR relation given by Ma et al. (2016). See Neijssel et al. (2019) for more details. We

do not take into account the observed scatter around the MZR; see for more details (Chruslinska & Nelemans 2019).

2.5 Detection probability of a source

Whether a BHNS merger is detectable by a GW interferometer network depends on its distance, orientation, inclination, and source characteristics (such as component masses $m_{1,f}$, $m_{2,f}$). The detectability is described by a source signal-to-noise ratio (SNR). We follow the method from Barrett et al. (2018) to calculate the probability of detecting GW sources. We assume an SNR threshold of 8 for a single detector (Finn & Chernoff 1993) as a proxy for detectability by the network. The SNR of the BHNS mergers is calculated by computing the source waveforms using a combination of the LAL suite software packages IMRPHENOMPV2 (Hannam et al. 2014; Husa et al. 2016; Khan et al. 2016) and SEOBNRV3 (Pan et al. 2014; Babak, Taracchini & Buonanno 2017).⁷ We marginalize over the sky localization and source orientation of the binary using the antenna pattern function from Finn & Chernoff (1993). The detector sensitivity is assumed to be equal to advanced LIGO in its design configuration (LIGO Scientific Collaboration 2015; Abbott et al. 2016, 2018a), which is equal to that of a ground-based GW detector network composed of Advanced LIGO, Advanced Virgo, and KAGRA (LVK). We ignore the effect of the BH spin orientation and magnitude on the detectability of GWs, which is expected to possibly increase detection rates within a factor of 1.5 (Gerosa et al. 2018) as binaries with (high) aligned spins are predicted to have larger horizon distances (Campanelli, Lousto & Zlochower 2006; Scheel et al. 2015).

2.6 Tidally disrupted BHNS

Simulations show that during a BHNS merger, the NS is either tidally disrupted outside of the BH innermost stable circular orbit or instead plunges in, depending on the mass ratio, BH spin, and NS equation of state (Pannarale, Tonita & Rezzolla 2011; Foucart 2012; Foucart, Hinderer & Nissanke 2018). If the NS is disrupted, part of the disrupted material can form a disc and can eventually power electromagnetic counterparts such as short gamma-ray bursts and kilonovae (Bhattacharya et al. 2019; Barbieri et al. 2020; Zhu et al. 2020). We estimate the ejected mass during a BHNS merger using equation (4) from Foucart et al. (2018), who present a simple formula for the merger outcome, post-merger remnant mass, and ejecta mass based on numerical relativity simulations. We define a BHNS merger to ‘disrupt’ the NS if the calculated ejecta mass is non-zero. By doing so, we can calculate the fraction of BHNS mergers that disrupt the NS outside of the BH innermost-stable orbit, which are interesting candidates for observing an electromagnetic counterpart to their GW detection. Detecting BHNS mergers with electromagnetic counterparts is a golden grail in astronomy as it would confirm the origin of such transients and enables, e.g. measurements of the NS equation of state and BHNS system. There has been a big effort in finding such a counterpart, such as to the possible BHNS merger GW190814, but so far without a detection (e.g. Dobie et al. 2019; Gomez et al. 2019; Ackley et al. 2020).

As the NS equation of state is unknown, we explore two variations for the NS radius: we assume $R_{\text{NS}} = 11.5$ km or $R_{\text{NS}} = 13$ km consistent with the APR equation of state (Akmal, Pandharipande &

Ravenhall 1998), GW observations (Abbott et al. 2018b), and the NICER observations (e.g. Miller et al. 2019), respectively.

The spins of the BHs in BHNS mergers, χ_{BH} , are also unknown (e.g. Miller & Miller 2015). For the BH spin, we explore three models. First, we assume all black holes to have zero spin, $\chi_{\text{BH}} = 0$. Secondly, we assume all BHs to have half the maximum spin value, $\chi_{\text{BH}} = 0.5$, which explores a scenario where BHs in BHNS have more moderate spins. Lastly, we explore an ad hoc but physically motivated spin model where we assign spins based on the study by Qin et al. (2018). Here, it is assumed that all first formed BHs in BHNS binaries have zero spin as a consequence of efficient angular momentum transport (Fragos & McClintock 2015; Qin et al. 2018; Fuller & Ma 2019; Belczynski et al. 2020). The helium star progenitors of BHs that form second in the binary, however, can spin-up through tidal interactions if they are in a close orbit with their companion, leading to BHs with significant spins (cf. van den Heuvel & Yoon 2007; Kushnir et al. 2016; Qin et al. 2018; Bavera et al. 2020; Mandel & Fragos 2020). For these NS–BH binaries, we use an approximate prescription to determine the BH spin:

$$\chi_{\text{BH}} = \begin{cases} 0 & \text{for } \log_{10}(P) > 0.3 \\ 1 & \text{for } \log_{10}(P) < -0.3 \\ -5/3 \log_{10}(P) + 0.5 & \text{for } -0.3 < \log_{10}(P) < 0.3, \end{cases} \quad (5)$$

where P is the orbital period of the binary in days right before the second SNe. We follow with this the prescription in Chattopadhyay et al. (2021), who create this ad hoc fit from the top middle panel of fig. 6 in Qin et al. (2018), which is based on a simulation for solar metallicity. Although in reality the spin distribution is more complicated and metallicity dependent, we use this single prescription for simplification. We expect that this does not impact drastically our results as the variation over metallicity is minor compared to the overall behaviour of most BHs having zero spin and only close NS–BH binaries having high spins. Moreover, we show in Section 4.1.5 that the amount of systems with ejecta is in this prescription dominated by the number of NS–BH binaries, and as this fraction is low, this prescription is most similar to the assumption where all χ_{BH} are zero.

We assume the BH spin to be aligned with the orbit and not vary from the moment the BHNS has formed. For each spin model, we vary the two NS radii assumptions, resulting in six different combinations of BH spin and NS radius. See Zappa et al. (2019) and Zhu et al. (2020) for a further discussion on the effect of different equations of state and BH spins on BHNS ejecta.

2.7 Statistical sampling uncertainty

Each of our simulations yields a finite number of BHNS mergers, as quoted in the last column of Table 2, which results in a statistical sampling uncertainty. We calculated this uncertainty on the BHNS formation rate (equation 1) using equation (15) from Broekgaarden et al. (2019) and found that this statistical uncertainty is at most 0.06 per cent, less than a tenth of a per cent. This is negligible compared to the systematic uncertainties from our assumptions in modelling of the massive binary evolution and the SFRD(Z_i , z).⁸ We therefore decide to not quote these statistical sampling uncertainties throughout the remaining of the paper and instead focus on the uncertainty from stellar evolution and SFRD(Z_i , z) variations. An

⁸And from our usage of a fixed, finite grid of birth metallicity points Z_i and redshift grid points for the cosmic integration, instead of (more) continuous distributions.

⁷See also LIGO Scientific Collaboration (2018).

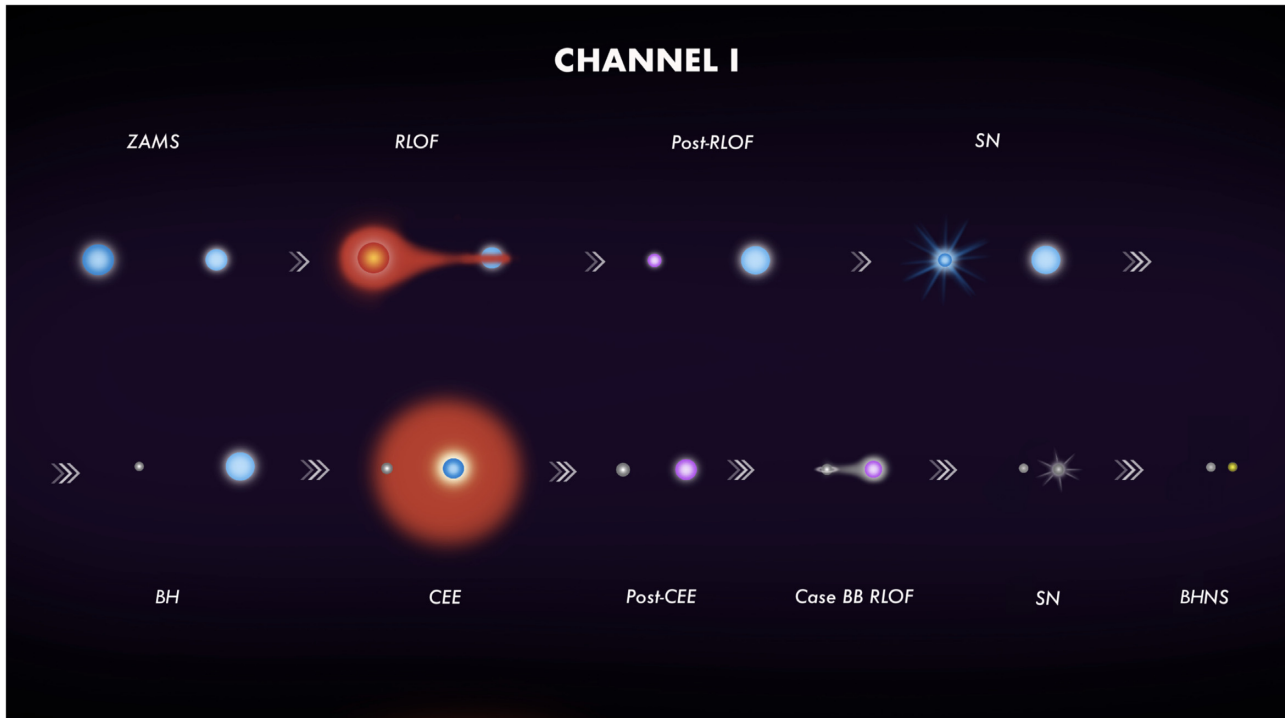


Figure 3. Schematic depiction of the classic formation channel as described in Section 3.1.1. The acronyms stand for: zero-age main sequence (ZAMS), Roche lobe overflow (RLOF), supernova (SN), black hole (BH), common-envelope episode (CEE), and black hole–neutron star (BHNS). The figure is based on fig. 1 from Vigna-Gómez et al. (2020) by T. Rebagliato, which is publicly available at <https://zenodo.org/record/3634498#.XnS9ZC2ZNQI>. Adjustments to the original image were made by S. Vinciguerra.

interested reader can find more details on the statistical uncertainties in the related script in <https://github.com/FloorBroekgaarden/BlackHole-NeutronStar> and in Broekgaarden et al. (2019) and references therein.

3 FIDUCIAL MODEL

In this section and in Figs 3–8, we describe the results of our population synthesis simulation for model A000, which uses both our fiducial assumptions for the massive (binary) star model (described in Section 2.1 and listed in Table 1) and our fiducial assumptions for the cosmic star formation history model (described in Section 2.4 and listed in Table 3). We focus on this model to provide insight to a typical output of a COMPAS simulation. This model choice is similar to earlier work done with COMPAS and has been chosen as it, for example, matches the population of galactic NSNS systems (Vigna-Gómez et al. 2018; Chattopadhyay et al. 2020) and the rate and chirp mass distributions of the GW sources in the first two observing runs of LIGO and Virgo (Neijssel et al. 2019). In Section 4, we describe the results for all 420 model variations.

3.1 Formation channels

We identify four main groups of formation channels described below. The percentages, quoted after each section header, indicate the fraction that each channel contributes to the total number of detected BHNS mergers. This takes into account the SFRD(Z_i, z) weighting using our fiducial model ($xyz = 000$) and the detection probability of a GW network equivalent to LVK at design sensitivity. These percentages are calculated using equation (4), while marginalizing over the BHNS masses. The percentage that each formation channel

contributes to the detectable merger rate is impacted by variations in the population synthesis and SFRD(Z_i, z) models. We present results for our 420 models in Section 4.1.3.

3.1.1 (I) Classic channel 86 per cent

We find, in agreement with, e.g. Neijssel et al. (2019) for BHBH mergers, that the majority of the binaries form a BHNS through the ‘classic’ formation channel where the binary experiences both a stable mass transfer and an unstable (CE) mass transfer phase. This classic channel is discussed in, e.g. Bhattacharya & van den Heuvel (1991); van den Heuvel & De Loore (1973); Tauris & van den Heuvel (2006); and Belczynski et al. (2008), see also Mandel & Farmer 2018 and references therein. We schematically depict this formation channel in Fig. 3 and describe it below in more detail for binaries that form a BHNS merger.

The binaries in the classic channel are born with a wide range of initial separations of about 0.3–20 AU as shown in Fig. 4. The initially more massive star (the primary) eventually expands and fills its Roche lobe initiating a stable mass transfer phase (Roche lobe overflow, RLOF) on to the initially less massive star (the secondary). This happens in this channel when the primary is either a Hertzsprung gap star or a core helium burning star (both case B mass transfer), where core helium burning donor stars are in initially wider binaries compared to Hertzsprung gap donor stars. In our fiducial model, the companion typically accretes a large fraction of the mass that is lost from the primary star donor. Mass transfer typically ends in our simulations when the donor has lost all of its hydrogen envelope. The result for case A or B mass transfer is typically a stripped envelope star that is burning helium, which may be observed as a Wolf–Rayet star (e.g. Crowther 2007; Götzberg et al. 2018).

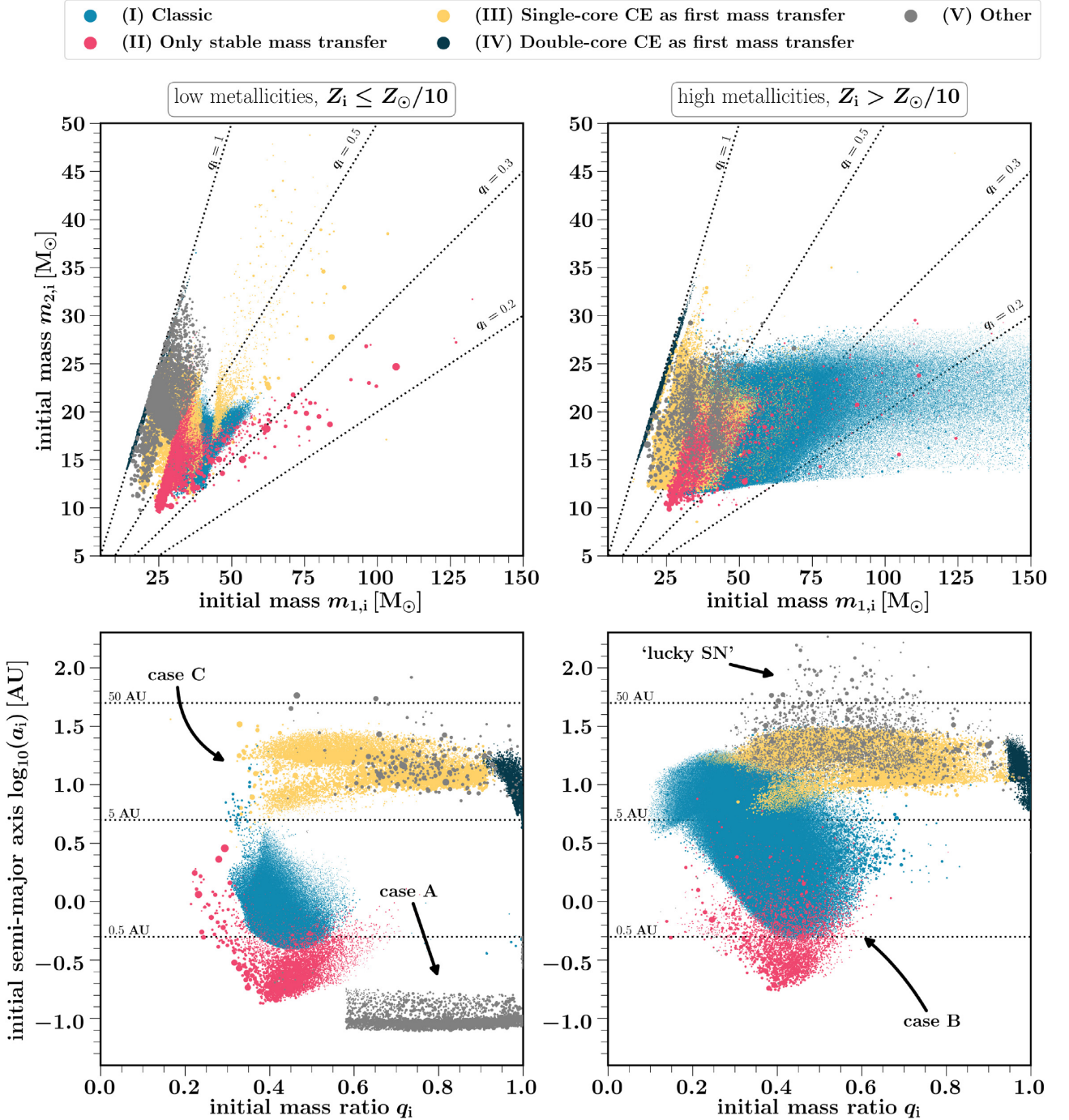


Figure 4. Initial parameters of binaries forming BHNS systems that merge in $t_{\mathcal{H}}$ for our fiducial model A000 (Section 2) for ‘lower’ metallicities $Z_i \leq Z_{\odot}/10$ (left-hand panels) and ‘higher’ metallicities $Z_i > Z_{\odot}/10$ (right-hand panels), where $Z_{\odot} = 0.0142$. Colours represent different formation channels, described in Section 3.1. Each point represents one simulated binary system that leads to a BHNS merger. The areas of the points represent the statistical weight w_i (i.e. probability of occurrence) of that binary in our simulation. Dotted lines indicate some values of the parameters to guide the reader. We define the initial mass ratio $q_i = m_{2,i}/m_{1,i}$. Arrows indicate regions where the first mass transfer is case A, B, or C, as well as ‘lucky SNe’ systems that do not experience mass transfer before the first SNe. Figures and videos showing how these distributions change over our model variations are available at <https://github.com/FloorBroekgaarden/BlackHole-NeutronStar>.

Eventually, the stripped primary star ends its life in a core-collapse (SNe) and the first compact object, a BH or an NS, is formed. The binary needs to stay bound during the SNe to eventually form a BHNS. Typically, more than 80 per cent of the binaries disrupt during the first SNe (e.g. Renzo et al. 2019), where disruption depends on the magnitude and orientation of the SNe kick, the separation of the

binary, and the amount of ejected mass (e.g. Flannery & van den Heuvel 1975; Tauris & Takens 1998).

The secondary star later evolves off the main sequence and expands to fill its Roche lobe. This is the start of a reverse mass transfer phase from the secondary on to the compact object. However, for this reverse mass transfer phase, the extreme mass ratio contributes to

the mass transfer being dynamically unstable and the start of CE evolution (e.g. Soberman et al. 1997; Ge et al. 2010, 2015; Vigna-Gómez et al. 2018). During the CE event, the separation of the binary decreases as orbital angular momentum and energy are transferred to the CE. If the CE is ejected successfully, the result is a close binary system consisting of a BH or an NS and a massive helium star; an example of a possible observed system in this phase is Cyg X-3 (Belczynski et al. 2013; Zdziarski, Mikolajewska & Belczynski 2013). Otherwise, the system results in a merger of the star with the compact object, which can possibly form a Thorne–Żytkow object (Thorne & Żytkow 1977) or lead to peculiar SNe (e.g. Chevalier 2012; Pejcha, Metzger & Tomida 2016; Schröder et al. 2020).

In a subset of the binaries, there is a stable case BB mass transfer phase after the CE from the helium star on to the primary compact object (cf. Dewi & Pols 2003). This typically occurs when the secondary is a relatively low-mass helium star as they expand to larger radii compared to more massive helium stars in the single-star prescriptions of Hurley et al. (2000) implemented in COMPAS (cf. Dewi & Pols 2003). However, Laplace et al. (2020) point out that these prescriptions might underestimate the expansion of helium stars, especially at metallicities $Z_i \approx 0.001$. BHNS systems undergoing case BB mass transfer typically have the shortest semimajor axis in Fig. 6.

The helium star eventually forms an NS or a BH in the second SNe. If the binary remains bound, a BHNS binary is formed with masses as in Fig. 6 that gradually decays in separation due to the emission of GWs. If the separation is small enough (typically $\lesssim 10 R_\odot$, see Fig. 6), the BHNS will merge within $t_{\mathcal{H}}$.

3.1.2 (II) Only stable mass transfer channel 4 per cent

In about 4 per cent of all detectable mergers, the binary forms similar to the classic channel (I) but does not experience an unstable mass transfer phase leading to a CE. This channel thus has only stable mass transfer phases (cf. van den Heuvel, Portegies Zwart & de Mink 2017; Neijssel et al. 2019, see also, e.g. Pavlovskii et al. 2017). To form BHNS systems with semimajor axis $\lesssim 10 R_\odot$ that can merge in $t_{\mathcal{H}}$, these binaries typically experience a second stable mass transfer phase from the secondary star on to the compact object after the first SNe that decreases the separation of the binary. This formation channel typically leads to BHNS mergers with final mass ratios $q_f \equiv m_{\text{BH}}/m_{\text{NS}} \approx 3$

3.1.3 (III) Single-core CE as first mass transfer channel 4 per cent

In the window of initial separations between $\sim 5\text{--}40$ AU as shown in Fig. 4, the first mass transfer phase leads to an unstable single-core CE event, with only the donor star having a clear core-envelope structure and the secondary star still being a main-sequence star. This is in agreement with other studies on mass transfer stability (see e.g. figs 19 and 20 in Schneider et al. 2015). The donor star that initialized the CE is typically a core helium burning star or a star on the giant branch. If the CE is successfully ejected, this leads to a tight binary star system. The primary star will eventually form a BH in an SNe. Eventually, the secondary star also evolves off the main sequence, leading to either a stable mass transfer phase or a second unstable CE event. The latter occurs for the widest binaries in Fig. 4. The secondary eventually forms an NS. In this formation channel, the BH always forms first in our simulations. This formation channel typically leads to BHNS mergers with final BHNS mass ratios $q_f \approx 3$ as shown in Figs 6 and 8.

3.1.4 (IV) Double-core CE as first mass transfer channel < 1 per cent

In this channel, the primary star fills its Roche lobe when both stars are on the giant branch and both stars have a core-envelope structure. The mass transfer is unstable, leading to a double-core CE. Both stars need to evolve on a similar time-scale and, therefore, have similar initial masses (i.e. $0.9 \lesssim q_i \lesssim 1$) as can be seen in the bottom panel of Fig. 4. Further evolution of the binary proceeds similar to channel III, except that in most cases there is never a case BB mass transfer phase. A BHNS system can be formed if the stars have carbon-oxygen core masses close to the boundary between NS and BH formation in our remnant mass prescription. This is visible in Fig. 6 where it can be seen that the BHNS in this channel have BH and NS masses that are very equal compared to the other formation channels. This formation channel typically also leads to BHNS mergers with the smallest final mass ratios $q_f \approx 1.5$ as shown in Figs 6 and 8. These low BHNS masses cause GW detectors to be less sensitive to finding binaries from this channel. This results in < 1 per cent of the detections being predicted from this channel, which is different from the expected contribution of this channel to, e.g. binary NS mergers (Vigna-Gómez et al. 2018). This channel is similar to the one described by Brown (1995), Bethe & Brown (1998), and later on by, e.g. Dewi, Podsiadlowski & Sena (2006), Justham, Podsiadlowski & Han (2011), and Vigna-Gómez et al. (2018).

3.1.5 (V) Other channel 6 per cent

We classify all other BHNS under the ‘other’ channel. The majority of contributions comes from two formation pathways. First, a large fraction of the other channel consists of binaries born with low metallicities and initial separations between about 0.01 and 0.20 AU (grey scatter points in bottom right of the bottom left-hand panel of Fig. 6). These binaries undergo mass transfer when the donor star is a main-sequence star (case A), which typically results in the secondary star accreting a large amount of mass from the primary. A lot of binaries from this formation pathway form the NS first. Secondly, most of the remaining binaries in the ‘other’ channel form by having a ‘lucky SNe natal kick’. The first event in this pathway is the primary star undergoing an SNe, and in a tiny fraction of those binaries the natal kick has the right magnitude and direction so that the binary stays bound.

3.2 Initial properties leading to BHNS mergers

The locations in the initial parameter space of the binaries (e.g. initial masses, initial mass ratio, and initial semimajor axis) leading to the formation of a BHNS system that merges in $t_{\mathcal{H}}$ are shown in Fig. 4 for metallicities $Z_i \leq Z_\odot/10$ and $Z_i > Z_\odot/10$, which represent, respectively, lower and more solar-like metallicity environments. We assume in our simulations $Z_\odot = 0.0142$ (Asplund et al. 2009). We chose the boundary $Z_i = Z_\odot/10$ somewhat arbitrarily as it is about half way in our Z_i grid (Fig. 5).

3.2.1 Initial masses

As can be seen in the top panels of Fig. 4, the majority of BHNS mergers at low Z_i originate from binaries with masses $10 \lesssim m_{1,i}/M_\odot \lesssim 60$ and $10 \lesssim m_{2,i}/M_\odot \lesssim 30$, while at higher metallicities this shifts to $10 \lesssim m_{1,i}/M_\odot \lesssim 150$ and $10 \lesssim m_{2,i}/M_\odot \lesssim 30$, respectively. A difference between the two panels is that, at higher metallicities, there are BHNS systems formed from binaries with initial mass ratios

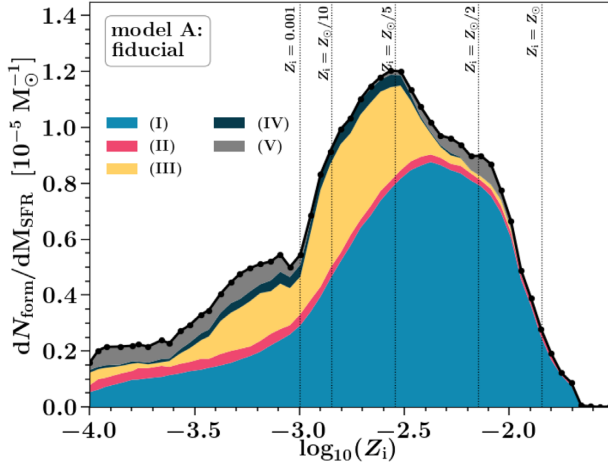


Figure 5. Number of BHNS mergers with $t_{\text{delay}} \leq t_{\mathcal{H}}$ that form per unit star-forming mass (M_{SFR}) as a function of initial metallicity Z_i for our fiducial model. This rate is obtained from equation (1) by marginalizing over t_{delay} , $m_{1,f}$, and $m_{2,f}$. The colours represent the contribution from each formation channel colour coded as in Fig. 4 and described in Section 3.1. The main formation channels are the (I) ‘classic’ channel (blue) and the (III) ‘single-core CE as first mass transfer channel’ (yellow). The 53 black scatter points denote the simulated Z_i grid points. Dotted lines indicate some Z_i values to guide the reader.

$\lesssim 0.3$, whereas these mostly lack at lower metallicities, as can also be seen in the lower panels of Fig. 4. This is because higher metallicities correspond to stronger line-driven stellar winds, leading to more mass loss, which equalizes the more extreme mass ratio before the onset of mass transfer, making the mass transfer more stable and the system more likely to survive to form a GW progenitor (cf. Belczynski et al. 2010b; Giacobbo & Mapelli 2018; Neijssel et al. 2019). At lower metallicities, there is fewer mass loss and so the mass ratio stays more extreme at the moment of mass transfer, making it often unstable and the stars merge. Moreover, on average, the total initial mass of binaries is higher at higher metallicities, as at those metallicities stellar winds strip more mass from the system compared to lower metallicities (Belczynski et al. 2010b). This stripping leads to lower mass carbon–oxygen cores compared to those of stars born with the same masses at lower metallicities. So, where at higher metallicities BHNS form, the same systems may form BHBH binaries at lower metallicities in our simulations.

3.2.2 Initial semimajor axis and mass ratio

The initial semimajor axis of the binaries forming BHNS mergers in Fig. 4 spans the range of about $0.1 \lesssim a_i \lesssim 50$ AU with higher metallicities favouring slightly larger a_i . The latter seems counterintuitive since stellar winds typically widen the binary but come from subtle and indirect effects of the wind loss being stronger at higher metallicities. As discussed above, the binaries at higher metallicities originate from initially more massive primary stars in the range of 25–150 M_{\odot} . The radii of these stars typically expand more during the Hertzsprung-gap phase in the stellar evolution tracks implemented in COMPAS (Hurley et al. 2000). Since this expansion, in combination with the initial separation, determines when mass transfer happens, the binary needs to have a much larger a_i at higher metallicities to form through the same channel as a binary at lower metallicities. In addition, the secondary star is typically more massive at the onset of a

CE for higher metallicity binaries, causing the binary to shrink more compared to lower metallicity binaries (cf. Neijssel et al. 2019).

3.3 Yield of BHNS mergers as a function of birth metallicity

Fig. 5 shows the contribution of the five formation channels to the yield of BHNS mergers as a function of metallicity. The yield of BHNS mergers peaks around metallicities $Z_i \approx Z_{\odot}/5$ ($Z_i \approx 0.003$) and is lowest around $Z_i \gtrsim Z_{\odot}$ in broad agreement with, e.g. Giacobbo & Mapelli (2018); Mapelli et al. (2019); and Neijssel et al. (2019), but there are some variations between these models in single stellar evolution, winds, mass transfer, and supernova prescriptions. The classic formation channel (channel I) dominates the yield. At metallicities $\log(Z_i) \lesssim Z_{\odot}/2$, the other formation channels also contribute, particularly, the single-core CE channel. For $Z_i > Z_{\odot}/2$ almost all BHNS mergers form through just two formation channels: the classic channel and a fraction forms through the only stable mass transfer channel. This is in agreement with Kruckow et al. (2018, see their table C1) and is a result from a combination of the metallicity-dependent effects described in the paragraphs above.

That the BHNS yield peaks around $Z_i \approx 0.003$ is due to line-driven stellar winds scaling positively with metallicity in our simulations (Section 2.1). First, at higher metallicities, higher wind-loss rates strip more mass from the star leading to lower compact object masses in our SSE and SNe remnant prescription. Lower mass BHs receive larger natal kicks and have less mass fallback (leading to larger Blaauw kicks) and smaller total system masses making them more likely to disrupt during the SNe. Secondly, at higher metallicities, binaries typically have wider separations after the second SN and therefore longer t_{inspiral} that may exceed $t_{\mathcal{H}}$. This is both because stellar winds widen the binary and because they result in stars with less massive envelopes, which reduces the amount of orbital hardening in mass transfer events (i.e. CE and stable Roche lobe overflow). At metallicities $Z_i \lesssim 0.001$, on the other hand, the formation rate of BHNS mergers is suppressed as the reduced stellar winds lead to massive enough carbon–oxygen cores that many systems instead form a BHBH merger. A second effect comes from that although overall the radius expansion of stars increases with increasing metallicity, particularly between $-3 \lesssim \log(Z_i) \lesssim -2$ the radius extension of Hertzsprung-gap stars decreases for primary star masses that lie in the range to form BHNS mergers. This decrease in radial extension decreases the number of systems that merge as stars during mass transfer (cf. Giacobbo & Mapelli 2018), which increases the rate of BHNS formation.

3.4 Final properties of BHNS mergers

The final characteristics of the BHNS systems at t_{DCO} (after the formation of the second compact object) are shown in Fig. 6. In addition, Fig. 7 shows the predicted distributions functions of the BHNS merger yield for five different simulated metallicities Z_i for typical BHNS characteristic at t_{DCO} . These characteristics are the BH mass m_{BH} , the NS mass m_{NS} , mass ratio $q_f = m_{\text{BH}}/m_{\text{NS}}$, eccentricity e_f , total mass $m_{\text{tot}} = m_{\text{BH}} + m_{\text{NS}}$, and chirp mass \mathcal{M}_c , which is a binary characteristic that is well measured by ground-based GW observatories and is given by

$$\mathcal{M}_c = \frac{(m_{\text{BH}}m_{\text{NS}})^{3/5}}{(m_{\text{BH}} + m_{\text{NS}})^{1/5}}, \quad (6)$$

the inspiral time t_{inspiral} and the semimajor axis, a_f , at t_{DCO} .

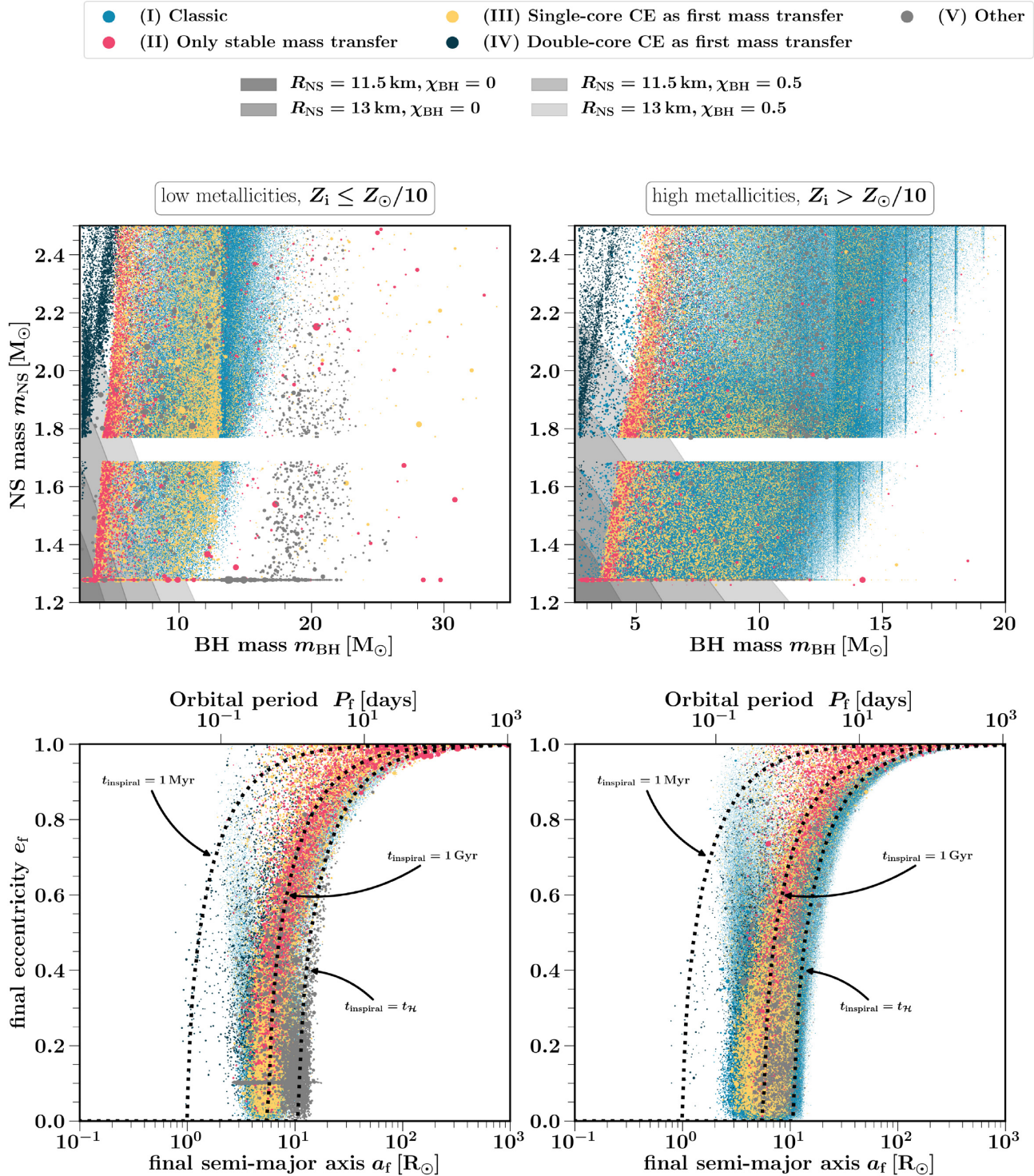


Figure 6. Same as Fig. 5 for the BHNS properties at DCO formation, t_{DCO} , for our Fiducial model A000. The grey areas in the top panels denote the DCOs that have final masses such that the NS is tidally disrupted outside the BH innermost stable circular orbit based on Foucart et al. (2018) when assuming an NS radius $R_{\text{NS}} \in \{11.5 \text{ km}, 13 \text{ km}\}$ and BH spins $\chi_{\text{BH}} \in \{0, 0.5\}$ for all BHs. Vertical lines, visible in the top right-hand panel, are artificially caused by our model that maps for a specific Z_i a small range of stars with different initial masses to the exact same BH mass as described in Section 3.4.1. The dotted black lines in the bottom panels show lines of constant $t_{\text{inspiral}} \in \{1 \text{ Myr}, 1 \text{ Gyr}, t_{\mathcal{H}}\}$. For the orbital period on the second x-axis and the lines of constant inspiral time, we assumed a fixed $m_{\text{BH}} = 10 M_{\odot}$ and $m_{\text{NS}} = 1.4 M_{\odot}$. Figures and videos showing how these distributions change over our model variations are available at <https://github.com/FloorBroekgaarden/BlackHole-NeutronStar>.

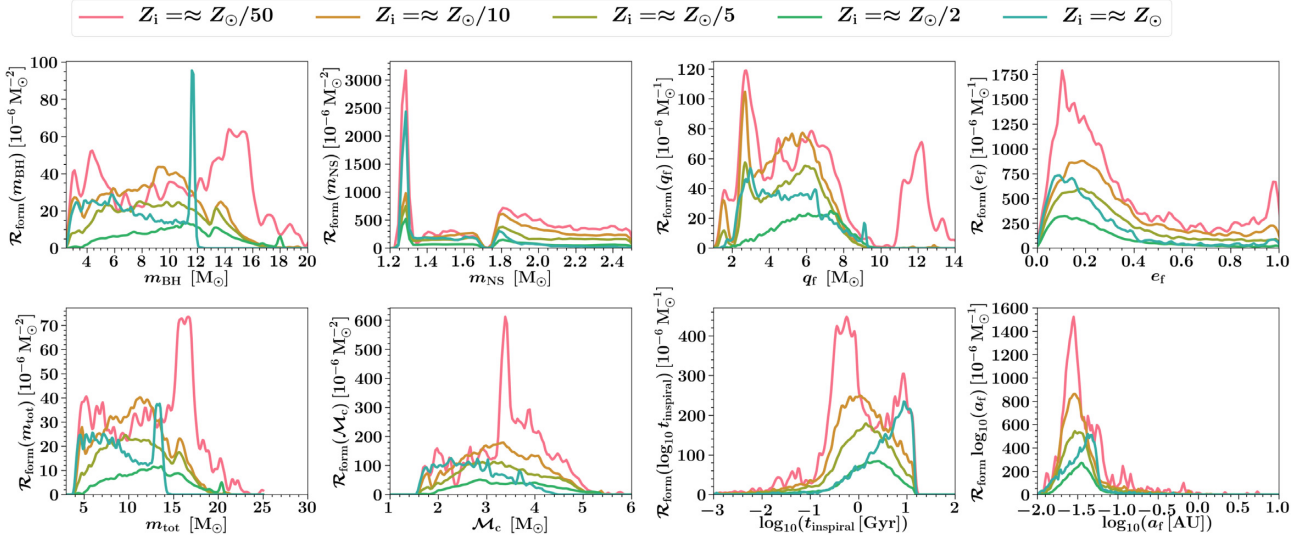


Figure 7. Distributions of the characteristics of BHNS systems that merge in $t_{\mathcal{H}}$ at t_{DCO} for five different metallicities Z_i . The yield is calculated using equation (1) and plotted using a weighted kernel density estimator with a dimensionless kernel bandwidth of 0.04; see the publicly available code for more details. We use the short-hand notation $\mathcal{R}_{\text{form}}(x) \equiv dN/(dM_{\text{SFR}}dx)$ for variable x . The variables are described in Section 3.4. We warn the reader that interpreting the distributions of t_{inspiral} and a_f can be misleading as they are shown in log to best demonstrate the characteristics over the wide parameter range. Plots showing more intuitive (not log) distributions of t_{inspiral} and a_f are given in <https://github.com/FloorBroekgaarden/BlackHole-NeutronStar>.

3.4.1 BH and NS remnant masses

The top panels in Fig. 6 show that the simulated BHNS mergers have NSs with masses in the range $1.25 \lesssim m_{\text{NS}}/M_{\odot} \leq 2.5$ (where the maximum NS mass is set to $2.5M_{\odot}$ in our fiducial model). The discontinuity in the NS remnant mass around $1.7M_{\odot}$ in Figs 6 and 7 results from the discontinuity in the proto-compact object mass equation at carbon–oxygen cores of $3.5M_{\odot}$ in the delayed SNe remnant mass prescription (equation 18 in Fryer et al. 2012). The overdensity of remnant masses around $1.3M_{\odot}$ comes from two effects. First, the ECSNe prescription maps stars with different masses to an NS mass of $1.26M_{\odot}$, as described in Section 2.1 and Vigna-Gómez et al. (2018). Secondly, all NS progenitors with carbon–oxygen core masses below $2.5M_{\odot}$ are in the delayed Fryer et al. 2012 remnant mass prescription mapped to NSs with fixed masses $\approx 1.28M_{\odot}$.⁹

The majority of BHs in the BHNS binaries have masses in the range $2.5 \leq m_{\text{BH}}/M_{\odot} \lesssim 20$, but this can extend to $m_{\text{BH}} \approx 30M_{\odot}$ for very low values of Z_i , as shown in the top left-hand panel of Fig. 6. We find that BHNS binaries with $m_{\text{BH}} \gtrsim 20M_{\odot}$ are rare, in agreement with, e.g. Rastello et al. (2020). At lower metallicities, BHNS mergers are formed with more massive BHs compared to higher metallicities, as can be seen in the distributions of m_{BH} , q_f , m_{tot} , and \mathcal{M}_c in Fig. 7 that are more extended to higher masses for lower metallicities. This is because stars at lower metallicities lose less mass during their lives through line-driven stellar winds leading to larger remnant masses. The delayed SNe remnant mass prescription does not lead to a BH mass gap between 2.5 and $5M_{\odot}$ and we therefore find BHs with masses close to the maximum NS mass of $2.5M_{\odot}$, as can be seen in Figs 6 and 7. The overdensity in m_{BH} in straight vertical lines, particularly visible in the right top panel of Fig. 6, is due to our prescription of LBV wind mass loss that maps a broad range of initial ZAMS masses to the same carbon–

oxygen core masses and hence the same BH remnant masses (see for a discussion appendix B of Neijssel et al. 2019). This results for some of our Z_i in peaks in the BH mass distribution around the highest BH mass for that metallicity as can be seen in the top right-hand panel of Fig. 6 and the top left-hand panel of Fig. 7.

A subset of the BHNS mergers in our fiducial simulation have final masses such that the NS is disrupted outside of the BH innermost stable circular orbit during the merger. This is shown in Fig. 6 with the shaded areas for four different models for the NS radii and BH spins. Typically, only the BHNS with low-mass BHs and NS result in a tidal disruption of the NS. The fraction of BHNS mergers that disrupt the NS outside of the BH innermost stable orbit is strongly dependent on the assumed BH spin and NSs radii, with higher spins and larger NS radii leading to more tidally disrupted NSs. We discuss this in more detail in Section 3.5.7.

3.4.2 Eccentricity and semimajor axis at t_{DCO}

Fig. 6 shows the semimajor axis and eccentricity for the BHNS mergers in our Fiducial model A000. BHNS binaries that merge in $t_{\mathcal{H}}$ typically have merger times in the range $1 \text{ Myr} \leq t_{\text{inspiral}} \leq t_{\mathcal{H}}$ at the moment of the BHNS formation, corresponding to a semimajor axis between $1 \lesssim a_f/R_{\odot} \lesssim 100$, as can be seen in the bottom panels of Fig. 6. Systems with larger semimajor axis still merge in $t_{\mathcal{H}}$ if the binary is more eccentric as this decreases t_{inspiral} . A subset of the binaries from the classic formation channel have the shortest semimajor axis at t_{DCO} , which is because these systems undergo a case BB mass transfer phase tightening the binary further after the CE phase.

Fig. 6 shows that the BHNS eccentricities densely populate the full range of 0–1, although smaller eccentricities are slightly favoured as can be seen in Fig. 7. We do not find clear subpopulations of BHNS systems with distinguishable eccentricity as discussed for NSNS systems by Andrews & Mandel (2019).

⁹For the rapid Fryer et al. (2012) remnant mass prescription, this maps to an NS mass of $\approx 1.1M_{\odot}$.

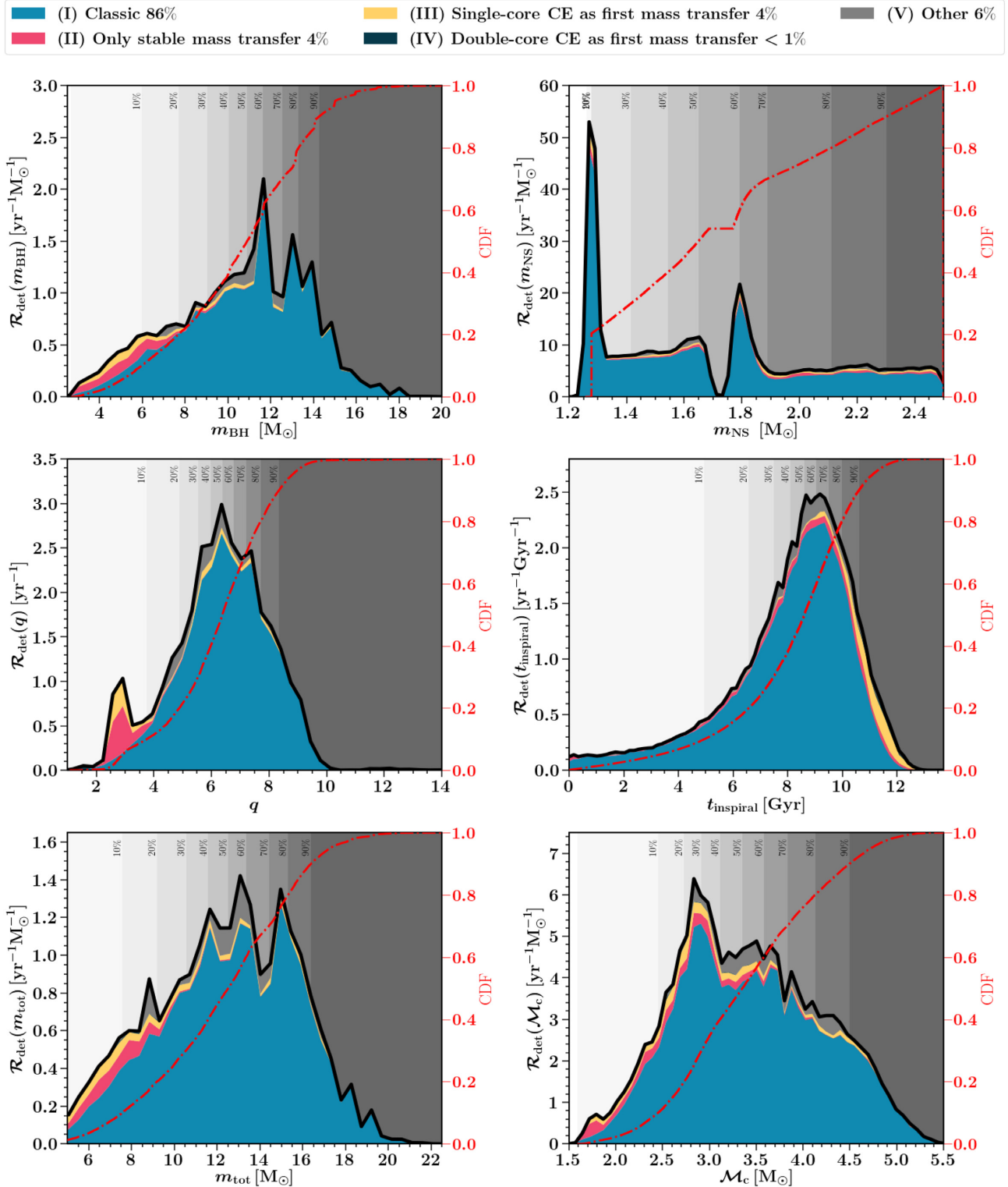


Figure 8. Predicted distributions of the detectable BHNS merger characteristics for our fiducial binary population synthesis and SFRD(Z_i, z) model A000 for a ground-based LVK detector network at design sensitivity. The detection rate is calculated using equation (4). The colours in each graph, and the numbers quoted in the legend, represent the percentage that each formation channel (presented in Section 3.1) contributes to the total GW-detected yield. The gap in the NS remnant mass distribution is caused by a discontinuity in the remnant mass prescription as discussed in Section 2.1. The red dashed–dotted lines show the cumulative distribution function (CDF). Grey areas indicate values for the CDF. The distributions are produced using a kernel density estimator with a bandwidth factor of 0.04; see our publicly available code for more details.

3.5 Predicted GW detectable BHNS distributions

The predicted GW detectable BHNS distributions for an LVK network at design sensitivity are shown in Fig. 8. We show the distribution for the BH mass, NS mass, mass ratio, inspiral times, total mass, and chirp mass (equation 6). Except for the inspiral times, t_{inspiral} , all other BHNS parameters are typically obtained from GW observations (e.g. Abbott et al. 2017). The distributions and yields are determined using equation (4), taking into account the SFRD(Z_i , z) and detector probability (P_{det}) weighting. In this section, we show the predicted distributions for our fiducial population synthesis and SFRD(Z_i , z) model, given by A000. In Section 4, we present the predicted BHNS distributions for all our 420 model variations. The predicted distributions and characteristics for NSNS and BHBH mergers are given in a companion paper.

Our fiducial model A000 presents an intrinsic BHNS merger rate at redshift zero of $\mathcal{R}_m^0 \approx 43 \text{ Gpc}^{-3} \text{ yr}^{-1}$ consistent with the inferred local BHNS merger rate density from Abbott et al. (2021d) of $\mathcal{R}_m^0 = 45_{-33}^{+75} \text{ Gpc}^{-3} \text{ yr}^{-1}$ when assuming that GW200105 and GW200115 are representative of the entire BHNS population, while slightly below the inferred $\mathcal{R}_m^0 = 130_{-69}^{+112} \text{ Gpc}^{-3} \text{ yr}^{-1}$ when Abbott et al. (2021d) assume a broader (and likely optimistic) distribution of component masses. When weighting for the sensitivity of a ground-based GW network, we find a detection rate of $\mathcal{R}_{\text{det}} \approx 11 \text{ yr}^{-1}$.

3.5.1 Formation channels

Our fiducial model predicts that about 86 per cent of the BHNS mergers detected by an LVK network at design sensitivity form through the classic formation channel (I, Section 3.1.1 and Fig. 3). This percentage is higher compared to the average percentage that the classic channel contributes for each Z_i in our simulation [without the SFRD(Z_i , z) and GW observation weighting]. This results from two main effects. First, our fiducial SFRD(Z_i , z) model convolved with the typical short delay times (Fig. 7) for BHNS systems biases the detectable BHNS systems to originate from binary systems with initial metallicities $Z_i \gtrsim Z_\odot/2$. At these metallicities, the contribution from other channels is relatively low (Fig. 5). Secondly, the classic formation channel produces overall more massive BHNS systems compared to the other channels as shown in Fig. 6, which are observed to larger distances with GW detectors. This further increases the contribution of the classic formation channel to eventually form the 86 per cent.

The dominant channel for BHBH and NSNS observations is different compared to our findings for BHNS mergers. For BHBH mergers, the majority of GW-detected mergers are predicted to form through the only stable mass transfer channel (II, e.g. Neijssel et al. 2019). For NSNS mergers, about 60–70 per cent of the detected systems are predicted to form through the double-core CE channel (IV, cf. Vigna-Gómez et al. 2018). BHNS mergers might thus provide a good probe to study the formation of GW sources that form through the classic formation channel compared to BHBH and NSNS mergers as there is less contamination from other channels. However, the contribution of each channel can drastically change as we vary population synthesis models, particularly for changes in the CE parameter and mass transfer efficiency, which we discuss in Section 4.1.3.

3.5.2 BH mass

The fiducial model predicts that the BHNS mergers will typically have $2.5 \lesssim m_{\text{BH}}/M_\odot \lesssim 16$, with less than 5 per cent of GW-detected

BHNS mergers having $m_{\text{BH}} \gtrsim 15 M_\odot$ (cf. Rastello et al. 2020), as can be seen in Fig. 8. This is different for BHBH mergers where the majority of predicted BHs is typically predicted to exceed $15 M_\odot$ (e.g. Neijssel et al. 2019). Some of the sharp peaks in the BH mass, such as the pile up around $m_{\text{BH}} \approx 12 M_\odot$, are caused by our grid of metallicity sampling in combination with our LBV wind prescription (see also Fig. 7 and Section 3.4.1).

3.5.3 NS mass

Fig. 8 shows that our fiducial model predicts a somewhat flat distribution in NS mass with two peaks around $1.3 M_\odot$ and $1.8 M_\odot$ caused by our choice of SNe remnant mass prescription. A large fraction of NSs in BHNS mergers are massive: almost 60 per cent of the BHNS observations are predicted to have $m_{\text{NS}} \gtrsim 1.5 M_\odot$ (cf. Giacobbo, Mapelli & Spera 2018). This is a much larger fraction compared to the typical fraction of NSNS mergers with an $m_{\text{NS}} \gtrsim 1.5 M_\odot$ (e.g. Vigna-Gómez et al. 2018). This mainly results from the NSs in BHNS systems originating from more massive stars compared to NSs in NSNS mergers. These more massive stars result in more equal mass ratio stellar binaries (since the binary also contains the BH progenitor), which is typically more likely to avoid a stellar merger and disruption during the SNe in the binary evolution. This favours more massive NSs in BHNS mergers. Massive BHs in BHNS mergers typically have more massive NS as can be seen in Fig. 6, in agreement with, e.g. Kruckow et al. (2018, fig. 7). All in all, BHNS mergers can be important for the study of massive NSs.

3.5.4 Mass ratio

Fig. 8 shows that the predicted BHNS merger mass ratio is typically in the range $2 \lesssim q_f \lesssim 10$, where we now define $q_f = m_{\text{BH}}/m_{\text{NS}}$ and peaks around $q_f \approx 5$ –8 (cf. Giacobbo et al. 2018) due to many BHs with $m_{\text{BH}} \approx 10$ – $12 M_\odot$ and the NS mass peaks around $1.3 M_\odot$ and $1.8 M_\odot$. There is also a small second peak around $q_f \approx 3$ from contributions from channels II and IV (Section 3.1) that produce BHNS mergers with low BH masses resulting in small q_f .

3.5.5 Inspirational time

The BHNS inspiral times typically span $t_{\text{inspiral}} \approx 2$ – 12 Gyr. Although most BHNS that merge in $t_{\mathcal{H}}$ are formed with $t_{\text{inspiral}} \lesssim 6$ Gyr (Fig. 7), selection effects favour the detection of systems that merge in the local Universe and so have longer delay times in order to match the higher rate of star formation and increased yields at higher redshifts. The t_{inspiral} distribution is sensitive to the assumed SFRD(Z_i , z) model. The delay time distribution of these mergers could be constrained in the future from observations (e.g. Fishbach, Holz & Farr 2018; Safarzadeh et al. 2019; Fishbach & Kalogera 2021) and might, therefore, help distinguishing binary population synthesis and SFRD(Z_i , z) models.

3.5.6 Total mass and chirp mass

The left bottom panel of Fig. 8 shows that the BHNS total masses are predicted to lie in the range $5 \lesssim m_{\text{tot}}/M_\odot \lesssim 20$. The shape of the total mass distribution follows as the BH mass dominates the total mass for BHNS mergers. The right bottom panel of Fig. 8 shows that the predicted chirp masses of the BHNS mergers lie in the range $1.5 \lesssim \mathcal{M}_c/M_\odot \lesssim 5.5$ with the majority of systems having chirp masses between about 2 and $5 M_\odot$.

Table 4. Fraction, f_{EM} , of the detectable BHNS mergers that are predicted to disrupt the NS outside of the BH innermost stable orbit. The different columns correspond to the different spin models assuming: (i) all BH spins are zero, (ii) an ad hoc, but physically motivated, model based on Qin et al. (2018) where the BH can have a moderate spin if it is formed second, and (iii) all BH spins are half the maximum spin. The rows correspond to assuming a 11.5-km and 13-km NS radius, respectively. The fractions are calculated using Foucart et al. (2018) and equation (4), taking into account the SFRD(Z_i, z) weighting from our fiducial model and detector sensitivity for a ground-based LVK detector network at design sensitivity.

f_{EM}	$\chi_{\text{BH}} = 0$	$\chi_{\text{BH}} \sim \text{Qin18}$	$\chi_{\text{BH}} = 0.5$
$R_{\text{NS}} = 11.5 \text{ km}$	0.013	0.015	0.13
$R_{\text{NS}} = 13 \text{ km}$	0.043	0.045	0.28

3.5.7 NS disruption

We predict that a fraction between ≈ 1 per cent and 28 per cent of the GW-detectable BHNS mergers will disrupt the NS outside of the BH innermost stable orbit as shown in Table 4 for our fiducial model A000. These systems are predicted to have non-zero ejecta mass and can potentially have an electromagnetic counterpart such as a short gamma-ray burst or kilonova. A subset of these systems could potentially be observed as electromagnetic counterpart. The highest fractions of BHNS mergers with non-zero ejecta masses is when assuming that systems have large NS radii and large BH spins, where especially the spins of the BH are dominant. Our models, except those assuming $\chi_{\text{BH}} = 0.5$, result in percentages on the order of 1 per cent consistent with, e.g. Drozda et al. (2020).

4 VARYING MODEL ASSUMPTIONS

The predicted rates and characteristics of BHNS mergers, presented in Section 3 for our fiducial model A000, are sensitive to uncertainties in binary population synthesis and SFRD(Z_i, z) model assumptions. We compare in this section the predicted BHNS merger rates and characteristics for our total of 420 combinations of the 15 binary

population synthesis and 28 SFRD(Z_i, z) models. These model variations are summarized in Tables 2 and 3. In most figures throughout this section, we highlight three of our SFRD(Z_i, z) models: the preferred phenomenological model from Neijssel et al. (2019), $xyz = 000$, and the SFRD(Z_i, z) prescriptions $xyz = 312$ and $xyz = 231$, which we show correspond to the lowest and highest BHNS merger rates, respectively.

4.1 Predicted BHNS merger rate for varying model assumptions

4.1.1 Intrinsic BHNS merger rates

The predicted intrinsic (at redshift $z = 0$) rates for BHNS mergers are shown for our 420 models in Fig. 9. These rates are calculated using equation (2) and do not yet take into account the GW-detector selection effects. We find that the intrinsic BHNS merger rates are predicted to lie in the range $\mathcal{R}_m^0 \approx 4\text{--}830 \text{ Gpc}^{-3} \text{ yr}^{-1}$. Our fiducial model A000 predicts $\mathcal{R}_m^0 \approx 43 \text{ Gpc}^{-3} \text{ yr}^{-1}$. We discuss in more detail the variations in rates over the models in Section 4.1.6. Almost all 420 models predict intrinsic BHNS merger rates that are consistent with one of the GW-inferred 90 per cent confidence interval for the BHNS merger rates from Abbott et al. (2021d).

4.1.2 GW-detectable BHNS merger rates

The predicted GW-detectable rates for BHNS mergers are shown in Fig. 10. These rates are calculated using equation (4) for a ground-based GW detector equivalent to the LVK network at design sensitivity for a full year observing run. Our fiducial model predicts a BHNS merger rate of $\mathcal{R}_{\text{det}} \approx 11 \text{ yr}^{-1}$. Considering the 420 model variations, we find predicted rates in the range $\mathcal{R}_{\text{det}} \approx 1\text{--}180 \text{ yr}^{-1}$. The GW-detectable rates in Fig. 10 behave similar under our 420 model variations as the intrinsic rates presented in Fig. 9. This is because the impact of the redshift evolution of the BHNS merger properties in our simulations is minor compared to changes over our model variations, within the GW horizon distance of BHNS mergers.

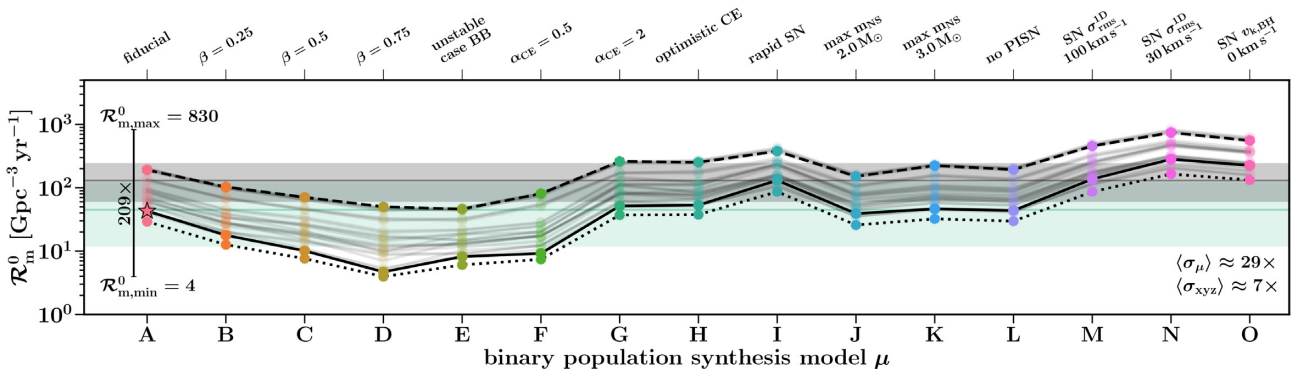


Figure 9. Predicted intrinsic BHNS merger rates for our 420 model variations. The rates are for mergers at $z = 0$ without applying GW selection effects. We show for each of the 15 binary population synthesis model variations (given in Table 2) the BHNS merger rates for the 28 variations in SFRD(Z_i, z) (given in Table 3). We connect predictions that use the same SFRD(Z_i, z) model with a line for visualization reasons only (it is not an interpolation between models). Three SFRD(Z_i, z) variations, $xyz = 000$ (solid), $xyz = 231$ (dashed), and $xyz = 312$ (dotted) are highlighted, corresponding to our fiducial SFRD(Z_i, z) model and the models resulting in one of the highest and lowest rate predictions. The shaded horizontal bars mark the corresponding GW-inferred 90 per cent credible intervals for the merger rate densities from Abbott et al. (2021d): $\mathcal{R}_m^0 = 45^{+75}_{-33} \text{ Gpc}^{-3} \text{ yr}^{-1}$ when assuming that GW200105 and GW200115 are representative of the entire BHNS population (teal) and $\mathcal{R}_m^0 = 130^{+112}_{-69} \text{ Gpc}^{-3} \text{ yr}^{-1}$ when assuming a broader distribution of component masses (grey). Our fiducial model (A000) estimate is shown with a star symbol. On the right of the panel, $\langle \sigma_\mu \rangle$ and $\langle \sigma_{xyz} \rangle$ represent the mean scatter in rates due to varying our assumptions in binary population synthesis and SFRD(Z_i, z) prescriptions, respectively. These are calculated using equations (7) and (8). The minimum and maximum rates and the ratio between those are quoted with an error bar on the left. We use the short-hand notation $\mathcal{R}_m^0 \equiv (dN_{\text{det}}^2 / dV_c dt_s) (t_m(z = 0))$.

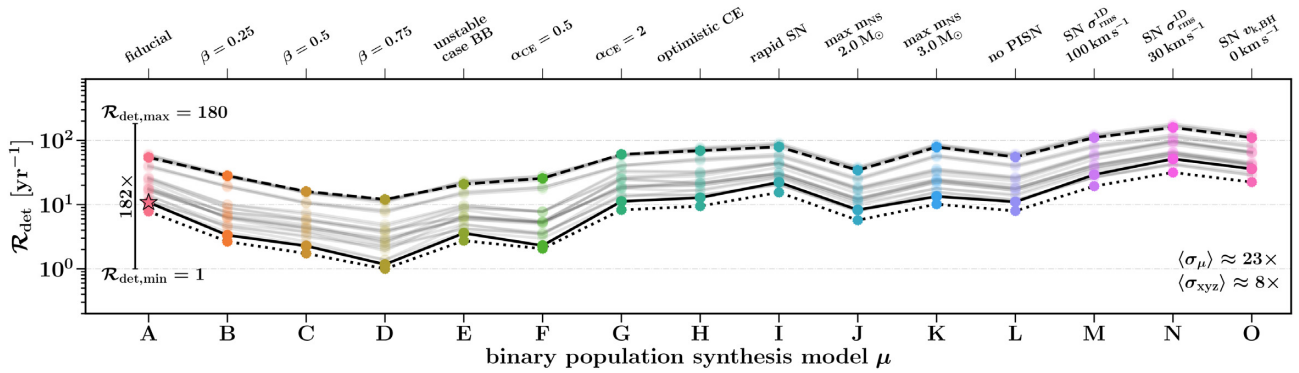


Figure 10. Same as Fig. 9 but for the predicted detectable BHNS rates for a GW network at design sensitivity. We use the short-hand notation $\mathcal{R}_{\text{det}} \equiv dN_{\text{det}}/dt_{\text{det}}$.

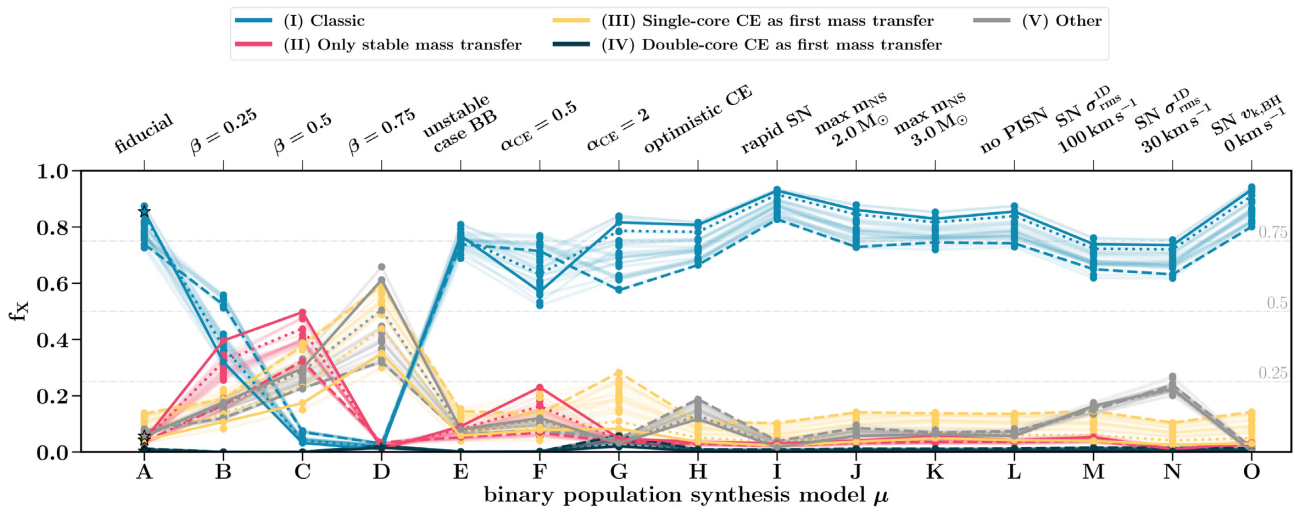


Figure 11. Fraction, f_X , that each formation channel contributes to the total predicted GW-detected BHNS merger rate \mathcal{R}_{det} for our 420 model variations (where the subscript X is a place holder for the formation channel label). Labels and lines are as in Fig. 10 but are coloured based on the five formation channels we classify as described in Section 3.1.

Table 5. Range of the minimum and maximum predicted percentage that each BHNS formation channel contributes when considering all 420 model variations studied in this work. From left to right the columns represent the formation channels labelled: (I) classic, (II) only stable mass transfer, (III) single-core CE as first mass transfer, (IV) double-core CE as first mass transfer, and (V) other. The formation channels are described in Section 3.1.

f_I	f_{II}	f_{III}	f_{IV}	f_V
0.01–0.94	0.008–0.50	0.021–0.60	0–0.59	<0.1–0.66

4.1.3 Formation channel rates

The predicted percentages that each formation channel contributes to the predicted total GW-detected BHNS merger rate are affected by variations in $\text{SFRD}(Z_i, z)$ and binary population synthesis models and shown in Fig. 11 and Table 5 for our five formation channels as described in Section 3.1. The minimum and maximum predicted percentages that each formation channel from Fig. 11 can contribute to the GW-detected BHNS rate are quoted in Table 5. We find that the fraction each formation channel contributes is dominated by variations in the binary population synthesis model over variations in $\text{SFRD}(Z_i, z)$. All models, except those involving binary population synthesis models B, C, and D, predict the classic formation channel (I) dominates the BHNS rate, with a percentage $f_I > 50$ per cent

of the GW-detectable BHNS coming from this channel. Particularly in models B, C, and D that assume a fixed mass transfer efficiency of $\beta = 0.25$, $\beta = 0.5$, and $\beta = 0.75$ for non-compact objects, respectively, this percentage drastically decreases, as in those models binaries going through the classic channel merge before they form a BHNS system. This is particularly visible in the variations for Figs 4–6 for models B and C, which are given in our online supplementary material. All in all, we find that the formation channel contributions for BHNS mergers are particularly sensitive to mass transfer, and so we expect that also varying binary population synthesis prescriptions for the stability criteria, the angular momentum loss and the CE prescription might further impact our results, as also suggested by, e.g. Klencki et al. (2020, see section 4.3).

4.1.4 GW-detectable NS–BH merger rates

NS–BH systems where the NS forms first are interesting astrophysical sources. First, because the first formed NS may spin-up during mass transfer episodes and eventually form a millisecond-pulsar BH binary that might be observable with radio telescopes (e.g. Pfahl, Podsiadlowski & Rappaport 2005; Chattopadhyay et al. 2021). Detecting such a system would provide a unique laboratory to test general relativity and alternative theories of gravity (Wex &

Kopeikin 1999; Kramer et al. 2004; Wex 2014) and will enable high precision measurements of the properties of BHs (Blandford & Teukolsky 1975; Brumberg et al. 1975). However, to date, no pulsar–BH system has been observed through radio observations. This might not be entirely surprising as several studies estimate that the fraction of pulsar–BH over NSNS binaries in our Milky Way is small (Pfahl et al. 2005; Chattopadhyay et al. 2021). Currently, there are about 20 NSNS known (e.g. Tauris et al. 2017; Farrow, Zhu & Thrane 2019). Secondly, in NS–BH systems the second formed BH may obtain a high BH spin if its progenitor helium star spun up due to tidal interactions with the NS companion, whereas a first formed BH in BHNS mergers may always have negligible spin (Qin et al. 2018). NS–BH mergers might, therefore, be distinguishable in GW observations by measuring a high χ_{eff} from the high NS or BH spins compared to BH–NS mergers that will always have low χ_{eff} (e.g. Chattopadhyay et al. 2021).

Fig. 12 shows the predicted fraction of detectable BHNS mergers where the NS formed first (NS–BH systems). We predict fractions of NS–BH mergers in the range $f_{\text{NS–BH}} \approx 0.00038\text{--}0.2$ for a GW network equivalent to LVK at design sensitivity. The highest fraction of NS–BH mergers is in the optimistic-CE model (H). This is because most NS–BH systems form from binaries where the first mass transfer occurs relatively early on (case A or early case B mass transfer). In our model, this phase of mass transfer is typically highly conservative and the stars can therefore exchange a large fraction of mass and reverse in masses, making the initial primary star the least massive star in the system and eventually form the NS first. Such systems also typically undergo a CE phase initiated by a donor star on the Hertzsprung gap, which are assumed to lead to a stellar merger in the pessimistic CE models. From Fig. 12, it can be seen that the fraction of GW-detectable NS–BH mergers is particularly sensitive to assumptions in the mass transfer and CE prescriptions, varied in binary population synthesis models B, C, D, E, F, G, and H. GW observations of χ_{eff} of BHNS mergers could therefore be particularly insightful to constraining the mass transfer and CE prescriptions, given that the spin properties of NS–BH are distinct from those of BH–NS mergers.

4.1.5 GW-detectable merger rates of BHNS systems that disrupt the NS outside of the BH innermost-stable orbit

Fig. 13 shows the predictions for the fraction of GW-detectable BHNS mergers for which the NS is disrupted outside the BH innermost stable circular orbit for six combinations of assumed NS radii and BH spins (described in Section 2.6). Our 420 model variations predict fractions in the range $f_{\text{EM}} \approx 0\text{--}0.70$. The predictions that assume the highest BH spin values predict the highest fraction of BHNS mergers that disrupt the NS outside of the BH innermost stable orbit. Larger NS radii assumptions also lead to higher fractions as this makes it easier to disrupt the NS. The unstable case BB model (E) and rapid SNe remnant mass prescription model (I) give the lowest fractions, where for the 11.5 km NS radius and zero or Qin et al. (2018) BH spin assumptions, none of the BHNS systems disrupt the NS outside of the BH. This is because only BHNS mergers with small NS and BH masses¹⁰ disrupt the NS outside of the BH innermost stable circular orbit for these most pessimistic assumptions for the NS radii and BH spins (see dark grey shaded area in top panels of Fig. 6). These low-mass remnants form from relatively low-mass helium stars that in model E undergo unstable case BB mass transfer and merge before

¹⁰Typically, $m_{\text{BH}} \lesssim 6 M_{\odot}$ and $m_{\text{NS}} \lesssim 1.7 M_{\odot}$; see Fig. 6.

forming a BHNS system. Model I does not produce, by construction, any BHs with $m_{\text{BH}} \lesssim 6 M_{\odot}$, which are the BH masses that can disrupt the NS outside of the BH for the most pessimistic NS radius and BH spin assumption. At the same time, model I also predicts the highest fraction of NS disruptions outside the BH innermost-stable orbit, as high as $f_{\text{EM}} \approx 0.70$ for the most optimistic assumptions of 13-km NS radii and BH spins of $\chi_{\text{BH}} = 0.5$. This is because the rapid SNe remnant prescription produces a peak of BHs with masses around $\sim 8 M_{\odot}$ that disrupt their NS under these assumptions.

Fig. 13 shows that the predicted rates of BHNS mergers that disrupt the NS outside of the BH innermost-stable orbit that assume our Qin et al. (2018) spin model (black and grey lines) are closest to our models that assume that all BHs have zero spins (yellow and orange lines). This is because in most BHNS mergers the BHs forms first, resulting in zero BH spins in our Qin et al. (2018) spin model. The only binary population synthesis model where the Qin et al. (2018) spin assumption predicted rates drastically deviate from the zero BH spin predicted rates is in the optimistic-CE model (H). This is because in this model the fraction of NS–BH mergers, where the NS formed first, can be as high as $f_{\text{NS–BH}} \approx 20$ per cent as shown in Fig. 12. As a result, a significant fraction of these NS–BH can achieve high spins in our Qin et al. (2018) model and disrupt the NS outside of the BH innermost-stable orbit.

The disruption of the NS outside of the BH innermost stable circular orbit can result in the production of electromagnetic transients such as short gamma-ray bursts, neutrinos, and kilonovae (e.g. Bhattacharya et al. 2019; Barbieri et al. 2020; Darbha et al. 2021). In a (small) fraction of such events, the electromagnetic counterpart might be detectable, allowing a multimessenger observation (e.g. a fraction of 0.1–0.5 for kilonovae cf. Bhattacharya et al. 2019; Zhu et al. 2020). This depends among other things on the distance to the BHNS merger, the luminosity of the electromagnetic transient, its orientation, and sky location.

4.1.6 Effect of varying binary population synthesis and SFRD(Z_i, z) assumptions on the predicted BHNS rates

To quantify the scatter in the predicted rates, i.e. the impact from varying our model assumptions, we calculate the mean of the ratios between the maximum and minimum predicted rates given by

$$\langle \sigma_{\mu} \rangle = \frac{1}{15} \sum_{\mu=A}^{\mu=O} \frac{\max(\mathcal{R}_{m,\mu000}^0, \dots, \mathcal{R}_{m,\mu333}^0)}{\min(\mathcal{R}_{m,\mu000}^0, \dots, \mathcal{R}_{m,\mu333}^0)}, \quad (7)$$

and

$$\langle \sigma_{xyz} \rangle = \frac{1}{28} \sum_{xyz=000}^{xyz=333} \frac{\max(\mathcal{R}_{m,Axyz}^0, \dots, \mathcal{R}_{m,Oxyz}^0)}{\min(\mathcal{R}_{m,Axyz}^0, \dots, \mathcal{R}_{m,Oxyz}^0)}. \quad (8)$$

The values for the scatter caused by our binary population synthesis and SFRD(Z_i, z) assumptions are quoted for our BHNS mergers in Figs 9 and 10. We find that for both the predicted intrinsic and detected BHNS merger rates $\langle \sigma_{\mu} \rangle \approx 20\text{--}30$ and $\langle \sigma_{xyz} \rangle \approx 8$. Overall, we thus find that variations from binary population synthesis and SFRD(Z_i, z) assumptions affect the rates of order $\sim \mathcal{O}(10)$. In the models that we varied, we find that the binary population synthesis variations impact the rate with a factor of 2–4 more compared to the variations in SFRD(Z_i, z). Figs 9 and 10 also show that the uncertainties are somewhat independent of each other: our SFRD(Z_i, z) assumptions introduce uncertainties of $\mathcal{O}(10)$ for all our binary population synthesis models and vice versa: varying our binary population synthesis model assumptions introduces uncertainties of

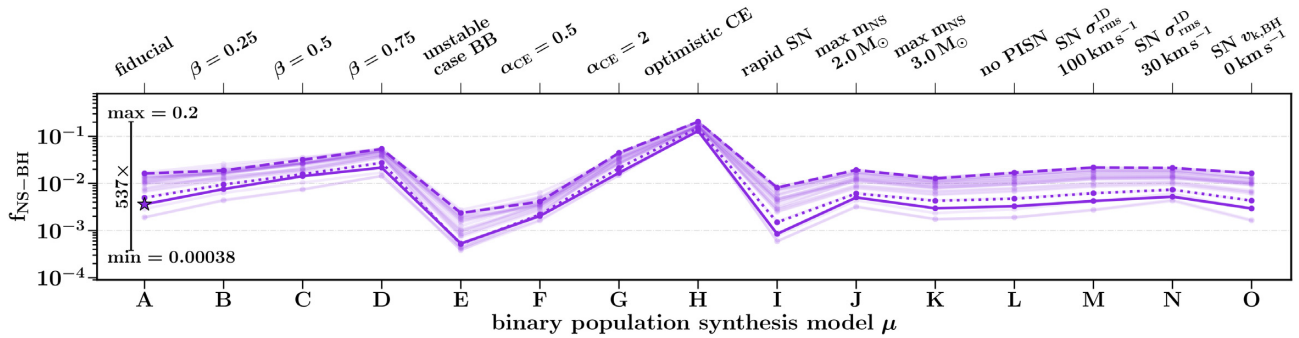


Figure 12. The predicted fractions of detectable BHNS systems where the NS forms first (NS–BH systems), $f_{\text{NS–BH}}$, for a GW network at design sensitivity. The labels and lines are as in Fig. 9.

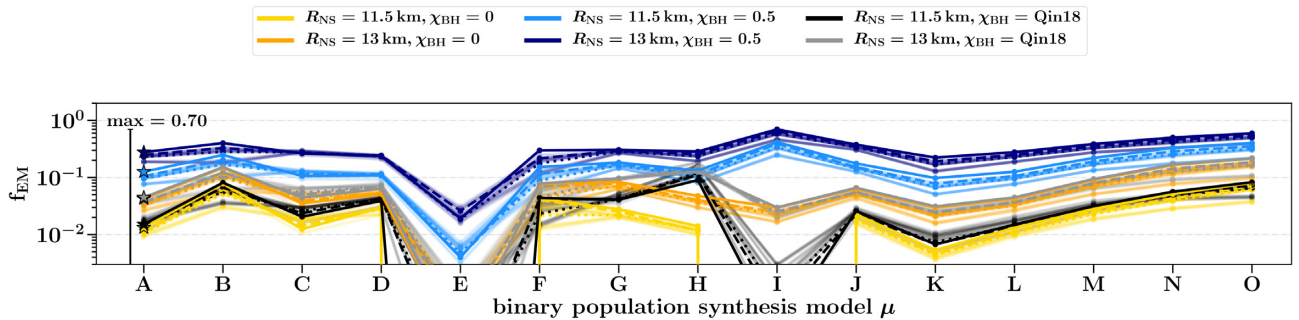


Figure 13. The fraction of GW-detected BHNS mergers in which the NS is disrupted outside of the BH innermost stable circular orbit (instead of plunging into the BH), f_{EM} . Different colours correspond to different assumptions for the NS radii and BH spins. The labels and lines are as in Fig. 9.

order $\mathcal{O}(10)$ for all our SFRD(Z_i, z) models. This is because in all our population synthesis models, the BHNS rate behaves overall similarly as a function of metallicity: the rate is suppressed both at extremely low and high metallicities for all our binary population synthesis variations. This is shown for our fiducial model in Fig. 5.

4.1.7 Effect from binary population synthesis variations

The highest predicted BHNS rates in Figs 9 and 10 are found in the binary population synthesis models G, H, I, K, M, N, and O, which have $\gtrsim 50$ per cent of the SFRD(Z_i, z) variations, typically predict BHNS merger rates $\mathcal{R}^0 \gtrsim 100 \text{ Gpc}^{-3} \text{ yr}^{-1}$, and predict for most SFRD(Z_i, z) models $\mathcal{R}_{\text{det}} \gtrsim 10 \text{ yr}^{-1}$.

In model G, the CE efficiency parameter is increased to $\alpha = 2$ compared to $\alpha = 1$ for our fiducial model. This means that we assume that more binary orbital energy is converted into unbinding the CE during the unstable mass transfer phase. This leads to more binaries surviving the CE phase as systems that do not successfully eject the envelope are assumed to merge as stars. The result is that the rate of BHNS mergers forming from formation channels involving a CE increases in our simulations for model G, as also visible for model G in Fig. 11.

The optimistic CE model (H) is the variation on our fiducial model where we allow Hertzsprung gap donors that engage in a CE event to survive. In this model, the BHNS merger rate is, therefore, enhanced compared to the fiducial model as a significant number of BHNS systems forms through a CE with a Hertzsprung gap donor. Fig. 12 shows that model H is especially important for forming a large fraction of NS–BH systems.

In the rapid SNe model (I), the rate of BHNS merger formation is also enhanced compared to our fiducial model that assumes

the delayed SNe remnant mass prescription. This is because most BHNS mergers form from binaries with secondary stars that have $10 \lesssim m_{2,i}/M_{\odot} \lesssim 30$ (Section 3.2 and top panels Fig. 4). The rapid SNe remnant mass function typically allows a larger fraction of secondary masses in this range to form an NS whereas in the delayed prescription these form a BH instead. This is visible in the bottom panel in fig. 12 of Fryer et al. (2012). This effect causes the BHNS rate to increase in our model I simulation.

In model K, which assumes a maximum NS mass of $3 M_{\odot}$, the BHNS merger rate is also enhanced as a fraction of the systems that in our fiducial model form BHBH mergers with one BH $\lesssim 3 M_{\odot}$ in this model forming a BHNS merger instead. Models M, N, and O all have lower BH and/or NS natal kicks compared to our fiducial model, which increases the fraction of systems that remain bound during the SNe and therefore increases the BHNS merger rate compared to our fiducial model.

Figs 9 and 10 show that when the mass transfer efficiency is changed to $\beta = 0.25, 0.5$, and 0.75 , respectively (models B, C, and D), this leads to a decreasing BHNS rate. This seems counterintuitive since higher values for β correspond to more mass accretion by a star during mass transfer, which intuitively leads to the formation of more BHs and higher BHNS merger rates. However, there is another effect: the detectable systems are highly biased towards tight binaries that merge within a Hubble time. As almost all our BHNS mergers in our fiducial model go through the classic formation channel (I) (Fig. 11), which involves a CE phase, a more massive companion leads to a more massive shared envelope that needs to be successfully ejected to avoid a stellar merger from the CE event. This leads to fewer BHNS systems as in agreement with findings by, e.g. Kruckow et al. (2018). Fig. 12 shows that the fraction of NS–BH mergers, on the other hand, increases for increasing β . This is because in this case

the contribution of systems that merge as a result from a failed CE ejection is relatively low as these binaries typically form from initially lower mass stars and will typically have a lower mass envelope in the CE compared to BH–NS binaries.

4.1.8 Effect from SFRD(Z_i, z) variations

For a given binary population synthesis model, the highest predicted BHNS rates are from the SFRD(Z_i, z) models with the Langer & Norman (2006) MZR (the models xy1). For a fixed galaxy mass, this MZR relation results in lower average birth metallicities compared to the other MZR variations as can be seen in Fig. B1(d) (see appendix B, and appendix A of Neijssel et al. 2019 for more details). This leads to a higher fraction of stars that form BHs and therefore to a higher yield of BHNS mergers. The other two MZRs, Langer & Norman (2006) + offset and Ma et al. (2016), corresponding to xy2 and xy3, respectively, lead to lower BHNS yields. We find that the MZR dominates the uncertainty in the predicted rates for our model variations, consistent with findings by, e.g. Artale et al. (2019) and Chruslinska & Nelemans (2019).

For the SFRD, we find that the Strolger et al. (2004) SFRD (2yz) typically has the highest yields, followed by the Madau & Dickinson (2014) (1yz) and Madau & Fragos (2017) (3yz) SFRD assumptions. This corresponds to each SFRD(Z_i, z) prescription having a different total star-forming yield, as can be seen in Fig. B1(a).

For the GSMFs, we find that the highest yield is given by the Furlong et al. (2015) functions, either single or double Schechter, which both give almost identical yields. On the other hand, the Panter et al. (2004) GSMF (x1z) leads to relatively lower BHNS merger yields. This is because the Furlong et al. (2015) GSMF prescriptions have relatively more low-mass galaxies compared to the Panter et al. (2004) GSMF as can be seen in Fig. B1(c), which map to lower Z_i and typically to higher BHNS yields.

In total, this leads to the SFRD(Z_i, z) models xyz = 231 and xyz = 312 having (one of) the highest and lowest BHNS merger yields for each binary population synthesis model, as can be seen in Figs 9 and 10. Our fiducial SFRD(Z_i, z) model (000) also produces one of the lowest yields. These three SFRD(Z_i, z) models are highlighted in Figs 9–13.

4.2 Predicted BHNS distribution functions for varying model assumptions

Besides the predicted rates (discussed in Section 4.1), the shapes of the predicted BHNS distributions are also sensitive to the binary population synthesis and SFRD(Z_i, z) assumptions. To summarize and compare these effects, we discuss in this section the shape of the BHNS merger distributions for our 420 model variations. We show the BH and NS masses (m_{BH} and m_{NS}), mass ratio ($q_{\text{r}} = m_{\text{BH}}/m_{\text{NS}}$), total mass ($m_{\text{tot}} = m_{\text{BH}} + m_{\text{NS}}$), and chirp mass (\mathcal{M}_{c}) distributions as these are properties of the BHNS mergers that are generally inferred from GW observations. In addition, we show the delay times, t_{delay} , and birth metallicity, Z_i , of the detected mergers. The birth metallicity is highly correlated with the inspiral times, shown in previous sections, as BHNS mergers with longer inspiral times typically formed from stars with lower Z_i . Throughout this section, we show normalized probability distribution functions of these BHNS characteristics to compare their shapes (the rates are given in Fig. 9 and 10). The distributions are weighted for the detection probability obtained from equation (4) for a GW detector equivalent to the LVK network at design sensitivity.

To summarize and compare the shape of the BHNS merger characteristics for 420 model variations, we focus on two figures. First, Fig. 14 shows the predicted BHNS probability distribution functions for all 420 model variations. This figure visualizes the overall shape of the distributions. Secondly, Fig. 15 shows the median and the 50 per cent, 90 per cent, and 99 per cent distribution quantiles for all 420 model variations.

4.2.1 BH mass

The top panel in Fig. 15 shows that for all our 420 model variations 90 per cent of the predicted observable BHNS mergers have m_{BH} in the range of 2.5–18 M_{\odot} . We find that in all model combinations less than 5 per cent of the BHNS mergers are predicted to have m_{BH} exceeding 18 M_{\odot} . Moreover, most of the 420 model variations predict that < 1 per cent of GW-detectable BHNS mergers have $m_{\text{BH}} \gtrsim 20 M_{\odot}$, and only in models B, C, D, and H this fraction is slightly above 1 per cent for some of the SFRD(Z_i, z) models. This is especially clear in the probability distribution functions (PDFs) for the BH mass shown in Fig. 14, where the region above $m_{\text{BH}} \gtrsim 20 M_{\odot}$ is visibly suppressed for all models. Even the models that do not assume (pulsational)–PISN (all models with $\mu = \text{L}$), or that have SFRD(Z_i, z) models that prefer low Z_i , lack a population of BHNS mergers with $m_{\text{BH}} \gtrsim 20 M_{\odot}$. All in all, we conclude that such massive BHs are extremely rare in BHNS mergers in all our 420 model variations. Detecting more than 1 per cent of BHNS mergers with $m_{\text{BH}} \gtrsim 20 M_{\odot}$ would therefore suggest that a large fraction of the BHNS systems form through a different formation channel than the isolated binary evolution channel, such as in AGN discs or through dynamical formation, which predict a significant fraction of BHNS mergers with BHs exceeding 20 M_{\odot} (e.g. Rastello et al. 2020). Alternatively, it could constrain binary population synthesis and SFRD(Z_i, z) models as basically all our models would be excluded as they do not support such observations. In Broekgaarden et al. (in preparation), we show that this is very different compared to our results for BHBH mergers, where typically our models predict that $\gtrsim 50$ per cent of GW detectable BHBH mergers contain two BHs that both have masses m_{BH} exceeding 18 M_{\odot} .

The m_{BH} distributions for models with the rapid SNe remnant mass model (I) sharply peak around $m_{\text{BH}} \approx 8 M_{\odot}$ in Fig. 14. This is because the rapid prescription maps a large range of ZAMS masses to this BH mass range (see fig. 12 of Fryer et al. 2012).

The top panel in Figs 14 and 15 also shows that BHNS mergers with $m_{\text{BH}} \lesssim 5 M_{\odot}$ are rare in most of our 420 models. In all models, except most of the SFRD(Z_i, z) models in combination with E (unstable case BB mass transfer) and all models with I (rapid SN remnant mass model) about 5 per cent of BHNS are expected to have BH masses below 5 M_{\odot} . The sharp boundary in the minimum BH mass for model I is caused by the rapid SNe remnant mass prescription, which assumes that no BHs form with $m_{\text{BH}} \leq 6 M_{\odot}$. Figs 14 and 15 show that models including B, C, G, H, N, and O have the largest fraction of BHNS mergers with $m_{\text{BH}} \lesssim 5 M_{\odot}$.

4.2.2 NS mass

The 90 per cent confidence intervals of the BHNS NS masses in the second row of Fig. 15 typically span the range $m_{\text{NS}} \approx 1.25$ –2.5 M_{\odot} . The exceptions of models where the 90 per cent quantiles shift significantly are model E (assuming unstable case BB) where the range is $m_{\text{NS}} \approx 1.8$ –2.5 M_{\odot} , model I (the rapid SN remnant mass model) where it shifts to $m_{\text{NS}} \sim 1.1$ –1.9, model J (assuming max $m_{\text{NS}} = 2 M_{\odot}$) where it shifts to 1.25–2 M_{\odot} , and model K (assuming

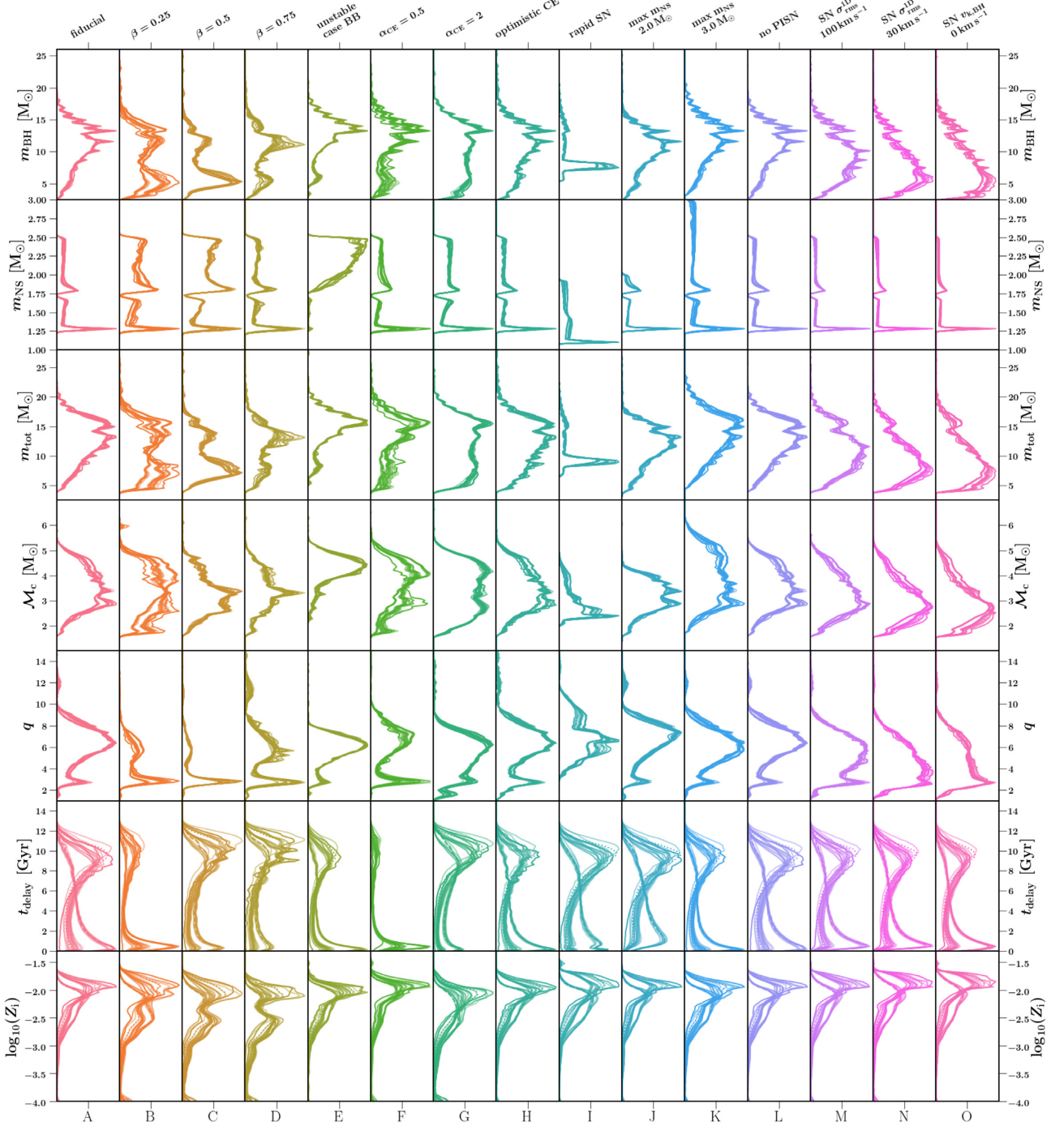


Figure 14. Predicted normalized probability distribution functions (PDFs) for BHNS merger characteristics for our 420 model variations of binary population synthesis and SFRD(Z_i, z) assumptions (Tables 2 and 3). Each row shows, for the 15 binary population synthesis variations (denoted with letters A, B,..., O, and different colours), the PDFs for the 28 SFRD(Z_i, z) models in a subfigure using a kernel density estimator. The PDF axis is plotted in linear scale. All distributions are weighted by the detection probability for an observatory equivalent to the LVK network at design sensitivity. For the kernel density functions, we use the dimensionless bandwidth. More details are given in <https://github.com/FloorBroekgaarden/BlackHole-NeutronStar>.

max $m_{\text{NS}} = 3 M_{\odot}$) where it shifts to $1.25\text{--}3 M_{\odot}$. Especially in Fig. 14, it can be seen that the unstable case BB model highly favours NSs with $m_{\text{NS}} \gtrsim 2 M_{\odot}$, which is a result from that the low-mass NSs are suppressed as their low-mass progenitor helium stars typically undergo a case BB mass transfer phase and merge before forming a BHNS system in this model. In addition, it can be seen that for the rapid SNe remnant mass model (I), the most

probable NS mass in BHNS mergers is predicted to be $\lesssim 1.25 M_{\odot}$. In most model variations, we find that the median NS mass is $\gtrsim 1.8 M_{\odot}$ and that except for models I and J, in all other models typically $\gtrsim 25$ per cent of GW-detectable BHNS mergers have NS with $m_{\text{NS}} \gtrsim 2 M_{\odot}$. Such massive NSs are thus predicted to be common in BHNS mergers as can also be seen in the Figs 14 and 15.

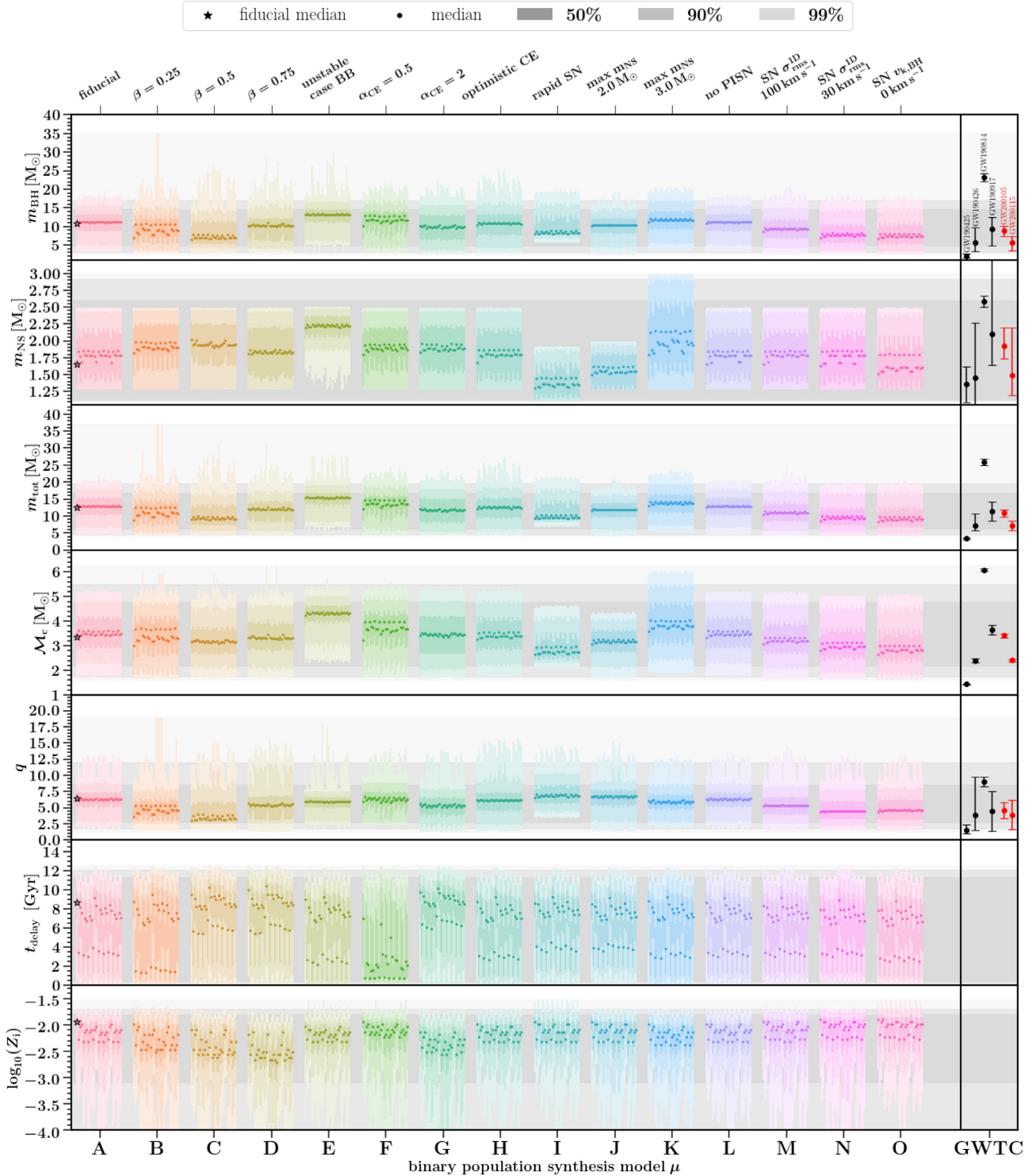


Figure 15. Distribution quantiles for the predicted BHNS distributions for our 420 model variations of binary population synthesis and SFRD(Z_i, z) assumptions (Tables 2 and 3). Panels, colours, and labels are as in Fig. 14. Each coloured block, which corresponds to one sub-figure in Fig. 14, shows 28 bars, indicating the 28 SFRD(Z_i, z) model variations. The SFRD(Z_i, z) labels of these bars are shown in Fig. C1 in appendix C. Each individual vertical bar representing one SFRD(Z_i, z) model shows the median (scatter points), 50 per cent, 90 per cent, and 99 per cent (see three shades) quantiles for the normalized probability distribution functions. The fiducial model (A000) median values are shown with star symbols. The grey areas in the background show the minimum and maximum values for the 50 per cent, 90 per cent, and 99 per cent distribution quantiles for all 420 models in each panel. All distributions are weighted by the detection probability for an observatory equivalent to the LVK network at design sensitivity. The rightmost columns show the median and 90 per cent credible intervals for the component masses, total mass, chirp mass, and mass ratio of the confident BHNS detections GW200105 and GW200115 in red (Abbott et al. 2021d) and the possible detected GW sources GW190425, GW190426, GW190814, and GW190917 in black (where a BHNS origin has not been ruled out yet; Abbott et al. 2021b, a).

4.2.3 Total mass and chirp mass

The BHNS total mass distributions follow the shape of the BH mass distributions as the BH typically dominates the mass of the BHNS. Fig. 15 shows that in all 420 model variations 90 per cent of the predicted GW-detectable BHNS mergers will have m_{tot} in the range of $\sim 5\text{--}20 M_{\odot}$ and hence that less than 5 per cent of BHNS mergers are predicted to have $m_{\text{tot}} \gtrsim 20 M_{\odot}$. The total mass peaks around $m_{\text{tot}} \approx 15 M_{\odot}$ for models including our fiducial model (A) and has the highest average in the unstable case BB model (E), as shown in Fig. 14, as in this model many of the binaries with low BH mass progenitors merge during unstable case BB mass transfer. The total mass peaks as low as $m_{\text{tot}} \approx 7 M_{\odot}$ for models including model C ($\beta = 0.5$) and models N and O with low SNe natal kicks. The latter is because low-mass BHs can get moderate kicks in our delayed remnant mass prescription, disrupting the binary, whereas in models N and O such low-mass BHs are given low or zero natal kicks.

Fig. 15 shows that 90 per cent of the predicted GW-detectable BHNS mergers will have $\mathcal{M}_c \approx 1.7\text{--}5.5 M_{\odot}$ and hence that less than 5 per cent of BHNS mergers are predicted to have $\mathcal{M}_c \gtrsim 5.5 M_{\odot}$. The most probable chirp masses, as shown in Fig. 14, are typically in the range $\mathcal{M}_c \approx 2\text{--}5 M_{\odot}$.

4.2.4 Mass ratio distribution

The 90 per cent quantiles for the BHNS mass ratio distributions lie for all models in $q_f \approx 2\text{--}12$ as shown in Fig. 15. The median and most probable BHNS q_f for our fiducial model (A), and most models, is $q_f \approx 6$ as shown in Fig. 14. For models B, C, and D ($\beta = 0.25, 0.5, 0.75$), however, this changes to a sharper peak around $q_f \approx 3$, as in these models low-mass BHs are more common. Fig. 15 also shows that in none of the models more than 5 per cent of the BHNS mergers are predicted to have $q_f \gtrsim 12$. In addition, Figs 14 and 15 show that BHNS mergers with $q_f \lesssim 2$ are predicted to be rare in all our 420 model variations (less than 5 per cent of all BHNS mergers).

4.2.5 Delay times

Figs 14 and 15 show that the predicted delay time distributions have a wide spread of t_{delay} , which typically peaks around 9 Gyr or 1 Gyr, where the peak depends mostly on the SFRD(Z_i, z) model that is used. Fig. 15 shows that SFRD(Z_i, z) models with relatively shorter median delay times (e.g. models with xy1) correspond to SFRD(Z_i, z) models with low median metallicities. This is because the delay time of the detected BHNS mergers is a convolution between the intrinsic delay time distribution and the SFRD(Z_i, z). Intrinsically, most BHNS mergers have short delay times $\lesssim 1$ Gyr (e.g. Fig. 7), and so the majority of BHNS systems has already merged before redshift $z = 0$. In addition, the yield of BHNS mergers is higher at lower metallicities (i.e. around $\log_{10}(Z_i) \approx -2.5$), as shown in Fig. 5. As a result, SFRD(Z_i, z) models with high median metallicities only form stars with low Z_i early in the Universe. Because of the high BHNS formation yield, these low metallicities dominate the rate, leading to the detected population having longer delay times (since the BHNS with short delay times from low metallicities will already have merged at high redshifts). On the other hand, SFRD(Z_i, z) models with low median metallicities still form low Z_i binaries at lower redshifts. All in all, this results in SFRD(Z_i, z) models with low median metallicities corresponding to shorter t_{delay} values.

4.2.6 Birth metallicities

Figs 14 and 15 show that the predicted range and shape of the birth metallicity distribution of the detected BHNS mergers are strongly impacted by the SFRD(Z_i, z) prescriptions. The scatter is mostly dominated by the MZR prescriptions in combination with the inspiral time distributions from the BHNS mergers. Models with relatively higher metallicities originate from SFRD(Z_i, z) prescriptions that have the Langer & Norman (2006) + offset or Ma et al. (2016) MZR relation that, for a given galaxy mass, maps to higher average initial metallicities. Fig. 14 shows that typically the metallicities have values in the range $Z_i \approx 0.001\text{--}0.03$. The highest values for the median of Z_i in Fig. 15 are $Z_i \sim 0.016$, whereas the lowest median values are $Z_i \sim 0.0018$.

4.2.7 Effect from variations in the binary population synthesis and SFRD(Z_i, z) model assumptions on the shape of the BHNS distribution functions

We find that the variation in the predicted BHNS distribution functions is typically dominated by the binary population synthesis model assumptions when comparing with the effect from variations in our SFRD(Z_i, z) models. This can be seen in Figs 14 and 15 that show that typically variations between models that use the same binary population synthesis model but different SFRD(Z_i, z) are smaller compared to variations in the predicted BHNS merger distributions between different binary population synthesis models. The main exceptions are the Z_i distributions, which are mostly impacted by variations in SFRD(Z_i, z). Models where some of the probability density function values change with factors 2 or more over variations of SFRD(Z_i, z) within the same binary population synthesis model include $\mu = \text{B}$ ($\beta = 0.25$), $\mu = \text{F}$ ($\alpha_{\text{CE}} = 0.5$), $\mu = \text{N}$ (reduced SN natal kicks of $\sigma_{\text{rms}}^{\text{ID}} = 30 \text{ km s}^{-1}$), and $\mu = \text{O}$ (zero BH natal kicks). This is particularly also visible in Fig. 15, where for those binary population synthesis models the median changes the most over SFRD(Z_i, z) variations. In all the figures, the largest impact by SFRD(Z_i, z) models comes from the MZR assumption, which seems to be an outlier in our SFRD(Z_i, z) models.

4.2.8 Comparison with GW observations

The right-most panels of Fig. 15 show the median and 90 per cent credible intervals for the component masses, total mass, chirp mass, and mass ratio of the two confident and four possible BHNS mergers from the third LIGO–Virgo–KAGRA observing run (Abbott et al. 2021a, b, d).

GW200105 and GW200115 are the first two confident BHNS mergers recently detected by LIGO–Virgo (Abbott et al. 2021d). The 90 per cent credible intervals of the properties of GW200105 are inferred to be $\mathcal{M}_c = 3.41_{-0.07}^{+0.08} M_{\odot}$, $m_{\text{tot}} = 10.9_{-1.2}^{+1.1} M_{\odot}$, $m_{\text{BH}} = 8.9_{-1.5}^{+1.2} M_{\odot}$, $m_{\text{NS}} = 1.9_{-0.2}^{+0.3} M_{\odot}$, and $q_f = 0.22_{-0.04}^{+0.08}$. For GW200115, the properties are $\mathcal{M}_c = 2.42_{-0.07}^{+0.05} M_{\odot}$, $m_{\text{tot}} = 7.1_{-1.4}^{+1.5} M_{\odot}$, $m_{\text{BH}} = 5.7_{-2.1}^{+1.8} M_{\odot}$, $m_{\text{NS}} = 1.5_{-0.3}^{+0.7} M_{\odot}$, and $q_f \equiv (m_{\text{NS}}/m_{\text{BH}}) = 0.26_{-0.10}^{+0.35}$. Both GW200105 and GW200115 are consistent with the predicted distributions from our population synthesis models as shown in Fig. 15. However, BHNS mergers with lower black hole masses, such as in GW200115, are more common in a subset of our models such as the simulations with $\beta = 0.25$ or $\beta = 0.5$ (models B and C) and/or low SNe natal kicks (models N and O). In Broekgaarden & Berger (2021), we discuss the formation of GW200105 and GW200115 from isolated binary evolution in more detail and show that our models with low SNe kick can potentially explain their formation as well as

simultaneously match the inferred BHNS, BHBH, and NSNS merger rate densities.

GW190425 is the system of the possible BHNS detections with the lowest total mass and is most likely an NSNS merger. However, a BHNS has not been ruled out. If it is a BHNS system, the component masses are $m_{\text{BH}} = 2.0_{-0.3}^{+0.6}$ and $m_{\text{NS}} = 1.4_{-0.3}^{+0.3}$, and \mathcal{M}_c , m_{tot} , and q_f are as shown with error bars in Fig. 15. The inferred credible intervals of GW190425, particularly those for the m_{BH} , m_{tot} and \mathcal{M}_c , fall outside of the typical parameter values predicted by our models, which might indicate that this is likely not a (typical) BHNS system.

GW190426 (short for GW190426.152155) is a candidate event with a relatively high FAR of 1.4 yr^{-1} (Abbott et al. 2021b), making it a less significant detection compared to the two events mentioned above. If this event is real, we find that its inferred parameter credible intervals match well with the predicted BHNS distributions for all shown parameters in Fig. 15.

GW190814 has been interpreted as a likely BHBH merger since its lower component mass is $2.59_{-0.009}^{+0.008} M_{\odot}$. However, a BHNS interpretation cannot be ruled out (Abbott et al. 2020e). We find that although our model K (max $m_{\text{NS}} = 3.0 M_{\odot}$) can produce such a massive NS, the other inferred credible intervals for GW190814, such as m_{tot} , \mathcal{M}_c , and m_{BH} , do not match well with typical BHNS distributions predicted by any of our models. These findings conform Zevin et al. (2020b), who also discuss the challenges in forming this system through isolated binary evolution.

GW190917 is a marginal BHNS event from the GWTC-2.1 catalogue (Abbott et al. 2021a). If real, this BHNS merger has inferred source parameters of $\mathcal{M}_c = 3.7_{-0.2}^{+0.2} M_{\odot}$, $m_{\text{BH}} = 9.3_{-4.4}^{+3.4} M_{\odot}$, $m_{\text{NS}} = 2.1_{-0.5}^{+1.5} M_{\odot}$, and $q_f = 0.23_{-0.09}^{+0.52}$, very similar to GW200105, that are consistent with our predicted populations.

5 DISCUSSION

5.1 Uncertainties beyond our models

We have modelled the rate and properties of BHNS mergers and demonstrated that uncertainties from both the massive (binary) star evolution and SFRD(Z_i, z) significantly impact the predicted results. However, even with our large set of 420 model variations, there are still additional uncertainties in the modelling that should be added and further explored in future work. We discuss the most important ones below.

5.1.1 SN remnant mass functions

Fig. 14 showed that model I, which uses the *rapid* SN remnant mass prescription from Fryer et al. (2012), is the model variation that resulted in one of the most drastic changes in the predicted BHNS distributions. This makes the remnant mass prescription one of the key assumptions in modelling BHNS merger properties. Many binary population synthesis studies use the *rapid* SN prescription instead of our default delayed SN remnant prescription (e.g. Klencki & Nelemans 2019; Belczynski et al. 2020). The rapid prescription assumes that SNe explosions occur within 250 ms (compared to longer time-scales assumed for the delayed prescription) and reproduces, by construction, the lower remnant mass gap between NSs and BHs that has been inferred from X-ray binary observations (Bailyn et al. 1998; Özel et al. 2010; Farr et al. 2011) by a lack of BHs in the mass range between about the heaviest NSs $\sim 3 M_{\odot}$ (Özel & Freire 2016; Kasen et al. 2017; Margalit & Metzger 2017; Abbott et al. 2020b; Sarin et al. 2020) and BHs of $\sim 6 M_{\odot}$.

It is still under debate whether this lower BH mass gap exists. Models of SNe predict a gap (Kochanek 2014; Pejcha & Thompson 2015) and no gap (e.g. Woosley & Weaver 1995; Fryer & Kalogera 2001; Chan, Müller & Heger 2020; Ertl et al. 2020); see also Burrows et al. (2020), who point out that it is challenging to model remnant masses, and that the compactness measure that is often used in these SNe remnant mass studies is not a good metric for SNe explodability. Moreover, Kreidberg et al. (2012) argue that the apparent mass gap in X-ray binaries could be caused by systematic offsets in the BH mass measurements. More recently, Thompson et al. (2019) found evidence for a $3.3_{-0.7}^{+2.8} M_{\odot}$ mass BH observed in a non-interacting binary with a red giant, adding to earlier speculation of an $\sim 2.44 \pm 0.27 M_{\odot}$ BH (Clark et al. 2002; Rude et al. 2010; Dolan 2011). In addition, Wyrzykowski et al. (2016) and Wyrzykowski & Mandel (2020) studied microlensing events of BHs based on observations from OGLE-III and *Gaia* data release 2. They found evidence for a continuous distribution of stellar remnant masses and disfavoured a mass gap between NSs and BHs (unless BHs receive natal kicks above $20\text{--}80 \text{ km s}^{-1}$). In addition, the LIGO–Virgo Collaboration reported in the second GW catalogue three GW events, GW190425, GW190814, and GW190426, with at least one component possibly in the lower mass gap (Abbott et al. 2021b). Zevin et al. (2020b) showed that particularly the formation of GW190814 might require the absence of the lower mass gap between NSs and BHs. Moreover, Vigna-Gómez et al. (2018) showed that the delayed prescription better matches the observed distribution of masses of Galactic double NS systems.

In practice, both the delayed and rapid SNe models might not represent the SNe remnant mass distribution and future work should, therefore, explore other alternatives (cf. Mandel et al. 2021; Román-Garza et al. 2021; Vigna-Gómez et al. 2021a). Examples include the Müller et al. (2016) prescription used in Vigna-Gómez et al. (2018), the remnant mass function studied in Román-Garza et al. (2021), and the probabilistic remnant mass function from Mandel & Müller (2020).

5.1.2 Other binary population synthesis variations

Besides the remnant mass prescription, there are many additional uncertainties from binary population synthesis prescriptions that should be explored in future work. Examples that we think could significantly impact the rate and characteristics of BHNS mergers include the wind prescription, exploring different models and assumptions for ECSNe and USSNe, exploring alternative models for the SNe natal kick magnitude, and using different prescriptions for the CE evolution (e.g. Klencki et al. 2020; Vigna-Gómez et al. 2020; Olejak et al. 2021). Beyond this, we also note that instead of varying one population parameter at a time, future work should do a more robust exploration of the full parameter space that includes changing parameters simultaneously (e.g. Barrett et al. 2018). In addition, future studies should incorporate more detailed stellar evolution tracks such as discussed in, e.g. Agrawal et al. (2020), Kruckow et al. (2018), and Bavera et al. (2021).

5.1.3 Metallicity-specific star formation rate density

As discussed in Section 2.4, in this work we used analytical prescriptions, commonly applied in binary population synthesis studies, to construct 28 SFRD(Z_i, z) models. This allows us to discuss the variation in the modelled properties of BHNS population caused by the different literature SFRD(Z_i, z) assumptions. We note that

to properly evaluate the uncertainty of the modelled properties of the BHNS population, one should cover the full range of SFRD(Z_i, z) assumptions allowed by observations. Establishing this range presents a challenge in itself (Chruslinska & Nelemans 2019) and is beyond the scope of this study. Furthermore, prescriptions introduced in Section 2.4 rely on important simplifications and do not reproduce all characteristics of the SFRD(Z_i, z) expected from observations (see e.g. discussion in Chruslinska & Nelemans 2019). For instance, our fiducial SFRD(Z_i, z) (following the phenomenological model from Neijssel et al. 2019) by construction produces a lognormal metallicity distribution, which is not supported by observations (e.g. Chruslinska & Nelemans 2019; Boco et al. 2021) and does not reproduce the extended low-metallicity tail of the distribution. Those issues could be circumvented with more detailed approaches, for instance, employing cosmological simulations to construct an SFRD(Z_i, z) (e.g. O’Shaughnessy, Kalogera & Belczynski 2010; Mapelli et al. 2017; Lamberts et al. 2018; Mapelli & Giacobbo 2018; Artale et al. 2019) or combining a wide range of recent observational results describing the properties of star-forming galaxies at different redshifts (Chruslinska & Nelemans 2019; Boco et al. 2019, 2021).

5.1.4 Initial conditions

We assumed fixed initial distributions for e.g. the initial masses and separations. In practice, these distributions are uncertain (e.g. Schneider et al. 2018) and may be metallicity or redshift-dependent (e.g. Gennaro et al. 2018), which is not taken into account here. Varying the uncertain initial conditions can impact the results for the predicted rates and shapes of BHNS merger distributions. Future work should explore this impact similar to studies such as de Mink & Belczynski (2015) and use correlated initial distribution function as described in work including de Mink & Belczynski (2015), Moe & Di Stefano (2017), and Klencki et al. (2018).

6 CONCLUSIONS

In this study, we made predictions for the intrinsic and GW-detectable rate and characteristics of BHNS mergers for ground-based GW detectors equivalent to the LVK network at design sensitivity. We accomplish this by simulating populations of binaries over a grid of 53 metallicities and convolving this with an SFRD(Z_i, z) and detection probability. We explore uncertainties arising from both assumptions in massive binary star evolution and the SFRD(Z_i, z) and present the BHNS rates and characteristics for a total of 420 variations (15 binary population synthesis and 28 SFRD(Z_i, z) variations). Our main findings are summarized below.

6.1 Predictions for BHNS mergers from our fiducial model

(i) Our fiducial model A000 predicts an intrinsic BHNS merger rate at redshift zero of $\mathcal{R}_m^0 \approx 43 \text{ Gpc}^{-3} \text{ yr}^{-1}$, consistent with the inferred merger rate from the first two BHNS observations by the LIGO/Virgo network (Abbott et al. 2021d). We find a GW detection rate of $\mathcal{R}_{\text{det}} \approx 11 \text{ yr}^{-1}$ for an LVK network at design sensitivity.

(ii) In Section 3.5.1, we show that our fiducial model predicts that 86 per cent of the GW-detectable BHNS mergers formed through the *classic* formation channel within isolated binary evolution (shown in Fig. 3). This channel involves first a dynamically stable mass transfer episode and eventually a reverse dynamically unstable (common-envelope) mass transfer phase. GW observations of BHNS mergers will therefore provide a clean probe of the classic formation channel

(whereas BHBH and NSNS detections might be dominated by different formation channels within isolated binary evolution).

(iii) In Fig. 8, we present the characteristic distributions for detectable BHNS mergers for our fiducial model A000. This model predicts that BHNS mergers observable with the LVK network at design sensitivity typically have BH masses of $2.5 \lesssim m_{\text{BH}}/M_\odot \lesssim 16$, with fewer than 5 per cent of BHNS mergers having $m_{\text{BH}} \gtrsim 15 M_\odot$. We also find that ≈ 60 per cent of the NS masses are $m_{\text{NS}} \gtrsim 1.5 M_\odot$. In addition, we find for A000 that the mass ratio is typically in the range $2 \lesssim q_f \lesssim 10$ ($q_f \gtrsim 2$ for $\gtrsim 98$ per cent of detectable BHNS mergers). The BHNS merger total mass and chirp mass for our fiducial model are predicted to lie in the ranges $5 \lesssim m_{\text{tot}}/M_\odot \lesssim 20$ and $1.5 \lesssim \mathcal{M}_c/M_\odot \lesssim 5.5$. The inspiral times for the majority of detected BHNS mergers are predicted to fall in the range $2 \lesssim t_{\text{inspiral}}/\text{Gyr} \lesssim 12$ in model A000.

(iv) Our fiducial model predicts that $f_{\text{EM}} \approx 1$ –28 per cent of the GW-detected BHNS mergers will have a disruption of the NS outside of the BH’s innermost stable circular orbit (Table 4). Such systems are expected to produce electromagnetic counterparts.

6.2 Varying binary population synthesis and metallicity-specific star formation rate models

In Section 4, we investigate how the predictions for the BHNS characteristics change over our 420 model variations in binary population synthesis and SFRD(Z_i, z) prescriptions (summarized in Tables 2 and 3).

6.2.1 Predicted rates

(i) The predicted merger rate is uncertain, spanning two orders of magnitude across our range of assumptions, where both binary evolution model assumptions and SFRD(Z_i, z) variations impact the predicted merger rates at the order-of-magnitude level. We show our predicted intrinsic BHNS merger rates in Fig. 9; these 420 rates span the range $\mathcal{R}_m^0 \approx 4$ –830 $\text{Gpc}^{-3} \text{ yr}^{-1}$. In Fig. 10, we show the rates of detectable events, which are in the range $\mathcal{R}_{\text{det}} \approx 1$ –180 yr^{-1} for an LVK network.

(ii) In Fig. 11, we show that in the majority of our models $\gtrsim 50$ per cent of the GW-detectable BHNS mergers form through the classic formation channel. However, we also show that, particularly when changing the mass transfer efficiency in models B, C, and D, the contribution of the classic channel is reduced to a few per cent and that other channels dominate the formation of BHNS mergers, including the only stable mass transfer channel (II) and single-CE as first mass transfer channel (III). We find that the double-core CE channel, which has been found to be important for the formation of NSNS mergers, does not significantly contribute to the formation of BHNS mergers in any of our 420 models.

(iii) We present in Fig. 12 the predicted fraction of GW-detectable BHNS mergers where the NS forms first. We find that this fraction lies in the range $f_{\text{NS-BH}} \approx 0$ –20 per cent, and that the fraction is mostly impacted by our mass transfer and CE assumptions. This fraction could be possibly inferred from the spin distribution of GW detections and the rate of occurrence of pulsar–BH systems.

(iv) We present for our 420 model variations the predicted fraction of GW observable BHNS mergers, where the NS is disrupted outside of the BH innermost-stable orbit in Fig. 13, and find that this fraction lies in the range $f_{\text{EM}} \approx 0$ –70 per cent. The lowest fractions are from models assuming small NS radii and low BH spins and from models assuming unstable case BB mass transfer or using the

rapid SNe remnant mass prescription. We find that in most of our 420 models, the fraction lies above 1 per cent even for our most pessimistic assumptions for the NS radii and BH spins.

6.2.2 Predicted shapes of the BHNS property distributions

In Figs 14 and 15, we present the predicted shapes of the probability distribution functions for the population of BHNS mergers that will be detected with design-sensitivity advanced GW instruments. We present results for BHNS merger characteristics including the BH and NS masses (m_{BH} , m_{NS}), the total mass (m_{tot}), the chirp mass (\mathcal{M}_c), the mass ratio ($q_f = m_{\text{BH}}/m_{\text{NS}}$), delay time (t_{delay}), and the initial metallicity (Z_i). We find that, except for the delay time and initial metallicity distributions, the shapes are predominantly impacted by the binary evolution variations and that the impact from variations in SFRD(Z_i, z) is typically minor.

(i) In all our 420 models, fewer than 5 per cent of the BHs in BHNS mergers are predicted to have $m_{\text{BH}} \gtrsim 18 M_{\odot}$, and typically $\lesssim 1$ per cent of the BHNS merges are predicted to have $m_{\text{BH}} \gtrsim 20 M_{\odot}$ (Section 4.2.1). Thus, our model variations do not commonly form GW events similar to GW190814, which is inferred to have $m_{\text{BH}} \gtrsim 20 M_{\odot}$.

(ii) In Section 4.2.2, we show that all models except I and J (which assume the ‘rapid’ SNe remnant mass function and a maximum NS mass of $m_{\text{NS}} = 2 M_{\odot}$, respectively) predict median NS masses of $\gtrsim 1.8 M_{\odot}$, with $\gtrsim 25$ per cent of the detectable BHNS mergers having $m_{\text{NS}} > 2 M_{\odot}$, making such massive NSs common in observations of BHNS mergers.

(iii) We find in Section 4.2.3 that in all 420 models, $\gtrsim 90$ per cent of the detectable BHNS mergers are predicted to have total masses in the range $m_{\text{tot}} \approx 5 - 20 M_{\odot}$ and chirp masses in the range $\mathcal{M}_c \approx 1.7 - 5.5 M_{\odot}$. Less than 5 per cent of BHNS mergers are predicted to have $m_{\text{tot}} \gtrsim 20 M_{\odot}$ or $\mathcal{M}_c \gtrsim 5.5 M_{\odot}$ in any of our models.

(iv) In Section 4.2.4, we show that in all 420 models, $\gtrsim 90$ per cent of the detectable BHNS mergers are predicted to have mass ratios in the range $q_f \approx 2 - 12$ and that less than 5 per cent of GW-detected BHNS mergers are predicted to have $q_f \gtrsim 12$. We also find that BHNS mergers with $q_f \lesssim 2$ are predicted to be rare (less than 5 per cent of all BHNS mergers) in all our simulations.

To summarize, we find that the rate and the shape of the distributions of GW-detectable BHNS mergers are significantly impacted by variations in binary evolution and SFRD(Z_i, z). Future BHNS observations can, therefore, help to constrain our models. On the other hand, several predictions above are robust among our 420 variations. If future GW observations of BHNS mergers support distributions that violate these predictions, it will mean that either all our 420 models miss some of the underlying physics necessary to correctly model BHNS mergers (as discussed in Section 5) or that BHNS mergers predominantly form through a different formation channel than the isolated binary evolution studied in this paper. Future GW observations and modelling, particularly simultaneously with constraints from NSNS and BHBH observations and electromagnetic observations, will aid in exploring massive binary star evolution and the metallicity-specific star formation history over cosmic time.

SOFTWARE

Simulations in this paper made use of the COMPAS rapid binary population synthesis code, which is freely available at <http://github.com/TeamCOMPAS/COMPAS> (Stevenson et al. 2017a; Barrett

et al. 2018; Vigna-Gómez et al. 2018; Broekgaarden et al. 2019). The simulations performed in this work were simulated with a COMPAS version that predates the publicly available code. Our version of the code is most similar to version 02.13.01 of the publicly available COMPAS code. Requests for the original code can be made to the lead author. The authors used STROOPWAFEL from Broekgaarden et al. (2019), publicly available at <https://github.com/FloorBroekgaarden/STROOPWAFEL>.¹¹ The authors also made use of python from the PYTHON Software Foundation. Python Language Reference, version 3.6 available at <http://www.python.org> (van Rossum 1995). In addition, the following PYTHON packages were used: MATPLOTLIB (Hunter 2007), NUMPY (Harris et al. 2020), SCIPY (Virtanen et al. 2020), IPYTHON/jupyter (Perez & Granger 2007; Kluyver et al. 2016), pandas (Wes McKinney 2010), and seaborn (Waskom & the seaborn development team 2020) (Astropy Collaboration 2018). This paper also made use of the hdf5 library for PYTHON, available at <https://docs.h5py.org/en/stable/> (Collette 2013; Kasen et al. 2017). This research has made use of NASA’s Astrophysics Data System Bibliographic Services. We also made use of the computational facilities from the FAS Research Computing and Birmingham computer cluster. This research has made use of data, software, and/or web tools obtained from the GW Open Science Center (<https://www.gw-openscience.org>), a service of LIGO Laboratory, the LIGO Scientific Collaboration, and the Virgo Collaboration. LIGO is funded by the U.S. National Science Foundation. Virgo is funded by the French Centre National de Recherche Scientifique (CNRS), the Italian Istituto Nazionale della Fisica Nucleare (INFN), and the Dutch Nikhef, with contributions by Polish and Hungarian institutes.

ACKNOWLEDGEMENTS

The authors thank Gus Beane, Christopher Berry, Charlie Conroy, Rosanne Di Stefano, Douglas Finkbeiner, Chris Fryer, Sebastian Gomez, Griffin Hosseinzadeh, Lokesh Khandawal, Floris Kummer, Joel Leja, Mathieu Renzo, Carl Rodriguez, Lieke van Son, Mario Spera, Ashley Villar, Serena Vinciguerra, Thomas Wagg, and Reinhold Willcox for helpful discussions and input on this manuscript. FSB thanks Munazza Alam, Marisa Borreggine, Victoria diTomasso, Miranda Eiben, Claire Lamman, Locke Patton, and Christina Richey for crucial input during this project. The authors also thank everyone in the COMPAS collaboration and Berger Time-Domain Group for help. In addition, the authors thank David Stops and the Harvard FAS research computing group for technical support on the simulations and high-performance computing part of the research. Lastly, FSB wants to acknowledge the amount of serendipity and privilege that was involved to end up pursuing this astronomy research. The Berger Time-Domain Group is supported in part by the National Science Foundation (NSF) grant AST-1714498 and NASA grant NNX15AE50G. Some of the authors are supported by the Australian Research Council Centre of Excellence for Gravitational Wave Discovery (OzGrav) through project number CE170100004. FSB is supported in part by the Prins Bernard Cultuurfonds studiebeurs 2020. IM is a recipient of the Australian Research Council Future Fellowship FT190100574. A.V-G. acknowledges funding support by the Danish National Research Foundation (DNRF132). SJ and SdM acknowledge funding from the Netherlands Organisation for

¹¹For the latest pip installable version of STROOPWAFEL, please contact Floor Broekgaarden.

Scientific Research (NWO), as part of the Vidi research program BinWaves (project number 639.042.728).

DATA AVAILABILITY

All data produced in this study are publicly available on Zenodo under the DOI [10.5281/zenodo.4574727](https://doi.org/10.5281/zenodo.4574727) through the link <https://doi.org/10.5281/zenodo.4574727>. All code, scripts, and files to reproduce all the figures, results, and supplementary material from the paper are publicly available through the main author’s Github repository <https://github.com/FloorBroekgaarden/BlackHole-NeutronStar> at doi:10.5281/zenodo.5555970.

REFERENCES

- Abadie J. et al., 2010, *Class. Quantum Gravity*, 27, 173001
- Abbott B. P. et al., 2016, *Living Rev. Relativ.*, 19, 1
- Abbott B. P. et al., 2017, *Annalen der Physik*, 529, 1600209
- Abbott B. P. et al., 2018a, *Living Rev. Relativ.*, 21, 3
- Abbott B. P. et al., 2018b, *Phys. Rev. Lett.*, 121, 161101
- Abbott B. P. et al., 2019, *Phys. Rev. X*, 9, 031040
- Abbott R. et al., 2020a, preprint (arXiv:2004.08342)
- Abbott B. P. et al., 2020b, *Class. Quantum Gravity*, 37, 045006
- Abbott R. et al., 2020c, *Phys. Rev. Lett.*, 125, 101102
- Abbott B. P. et al., 2020d, *ApJ*, 892, L3
- Abbott R. et al., 2020e, *ApJ*, 896, L44
- Abbott R. et al., 2020f, *ApJ*, 900, L13
- Abbott R. et al., 2021a, preprint (arXiv:2108.01045)
- Abbott R. et al., 2021b, *Phys. Rev. X*, 11, 021053
- Abbott R. et al., 2021c, *ApJ*, 913, L7
- Abbott R. et al., 2021d, *ApJ*, 915, L5
- Abt H. A., 1983, *ARA&A*, 21, 343
- Abt H. A., Gomez A. E., Levy S. G., 1990, *ApJS*, 74, 551
- Acernese F. et al., 2015, *Class. Quantum Gravity*, 32, 024001
- Ackley K. et al., 2020, *A&A*, 643, A113
- Agrawal P., Hurley J., Stevenson S., Szécsi D., Flynn C., 2020, *MNRAS*, 497, 4549
- Akmal A., Pandharipande V. R., Ravenhall D. G., 1998, *Phys. Rev. C*, 58, 1804
- Almeida L. A. et al., 2017, *A&A*, 598, A84
- Alsing J., Silva H. O., Berti E., 2018, *MNRAS*, 478, 1377
- Anagnostou O., Trenti M., Melatos A., 2020, preprint (arXiv:2010.06161)
- Andrews J. J., Mandel I., 2019, *ApJ*, 880, L8
- Andrews J. J., Zezas A., Fragos T., 2018, *ApJS*, 237, 1
- Antoniadis J. et al., 2013, *Science*, 340, 448
- Arca Sedda M., 2020, *Commun. Phys.*, 3, 43
- Arca Sedda M., 2021, *ApJ*, 908, L38
- Artale M. C., Mapelli M., Giacobbo N., Sabha N. B., Spera M., Santoliquido F., Bressan A., 2019, *MNRAS*, 487, 1675
- Arzoumanian Z., Chernoff D. F., Cordes J. M., 2002, *ApJ*, 568, 289
- Aso Y., Michimura Y., Somiya K., Ando M., Miyakawa O., Sekiguchi T., Tatsumi D., Yamamoto H., 2013, *Phys. Rev. D*, 88, 043007
- Asplund M., Grevesse N., Sauval A. J., Scott P., 2009, *ARA&A*, 47, 481
- Astropy Collaboration, 2018, *AJ*, 156, 123
- Babak S., Taracchini A., Buonanno A., 2017, *Phys. Rev. D*, 95, 024010
- Bae Y.-B., Kim C., Lee H. M., 2014, *MNRAS*, 440, 2714
- Baibhav V., Berti E., Gerosa D., Mapelli M., Giacobbo N., Bouffanais Y., Di Carlo U. N., 2019, *Phys. Rev. D*, 100, 064060
- Bailyn C. D., Jain R. K., Coppi P., Orosz J. A., 1998, *ApJ*, 499, 367
- Banerjee S., 2021, *MNRAS*, 500, 3002
- Barbieri C., Salafia O. S., Perego A., Colpi M., Ghirlanda G., 2020, *Eur. Phys. J. A*, 56, 8
- Barkat Z., Rakavy G., Sack N., 1967, *Phys. Rev. Lett.*, 18, 379
- Barnes J., Kasen D., 2013, *ApJ*, 775, 18
- Barrett J. W., Mandel I., Neijssel C. J., Stevenson S., Vigna-Gómez A., 2017, in Brescia M., Djorgovski S. G., Feigelson E. D., Longo G., Cavuoti S., eds, Proc. IAU Symp. 325, *Astroinformatics*. Cambridge Univ. Press, Cambridge, p. 46
- Barrett J. W., Gabel S. M., Neijssel C. J., Vigna-Gómez A., Stevenson S., Berry C. P. L., Farr W. M., Mandel I., 2018, *MNRAS*, 477, 4685
- Bavera S. S. et al., 2020, *A&A*, 635, A97
- Bavera S. S. et al., 2021, *A&A*, 647, A153
- Belczynski K., Kalogera V., Bulik T., 2002, *ApJ*, 572, 407
- Belczynski K., Kalogera V., Rasio F. A., Taam R. E., Zezas A., Bulik T., Maccarone T. J., Ivanova N., 2008, *ApJS*, 174, 223
- Belczynski K., Bulik T., Fryer C. L., Ruiters A., Valsecchi F., Vink J. S., Hurley J. R., 2010a, *ApJ*, 714, 1217
- Belczynski K., Dominik M., Bulik T., O’Shaughnessy R., Fryer C., Holz D. E., 2010b, *ApJ*, 715, L138
- Belczynski K., Bulik T., Mandel I., Sathyaprakash B. S., Zdziarski A. A., Mikołajewska J., 2013, *ApJ*, 764, 96
- Belczynski K., Holz D. E., Bulik T., O’Shaughnessy R., 2016a, *Nature*, 534, 512
- Belczynski K., Repetto S., Holz D. E., O’Shaughnessy R., Bulik T., Berti E., Fryer C., Dominik M., 2016b, *ApJ*, 819, 108
- Belczynski K., Ryu T., Perna R., Berti E., Tanaka T. L., Bulik T., 2017, *MNRAS*, 471, 4702
- Belczynski K. et al., 2020, *A&A*, 636, A104
- Belczynski K. et al., 2021, preprint (arXiv:2108.10885)
- Beniamini P., Piran T., 2016, *MNRAS*, 456, 4089
- Beradze R., Gogberashvili M., Sakharov A. S., 2020, *Phys. Lett. B*, 804, 135402
- Bethe H. A., Brown G. E., 1998, *ApJ*, 506, 780
- Bhattacharya D., van den Heuvel E. P. J., 1991, *Phys. Rep.*, 203, 1
- Bhattacharya M., Kumar P., Smoot G., 2019, *MNRAS*, 486, 5289
- Blandford R., Teukolsky S. A., 1975, *ApJ*, 198, L27
- Blinnikov S. I., Novikov I. D., Perevodchikova T. V., Polnarev A. G., 1984, *SvA Lett.*, 10, 177
- Boco L., Lapi A., Goswami S., Perrotta F., Baccigalupi C., Danese L., 2019, *ApJ*, 881, 157
- Boco L., Lapi A., Chruslinska M., Donevski D., Sicilia A., Danese L., 2021, *ApJ*, 907, 110
- Bouffanais Y., Mapelli M., Santoliquido F., Giacobbo N., Iorio G., Costa G., 2021, *MNRAS*, 505, 3873
- Brandt W. N., Podsiadlowski P., Sigurdsson S., 1995, *MNRAS*, 277, L35
- Breivik K. et al., 2020, *ApJ*, 898, 71
- Briskin W. F., Benson J. M., Goss W. M., Thorsett S. E., 2002, *ApJ*, 571, 906
- Broekgaarden F. S., Berger E., 2021, *ApJ*, 920, L13
- Broekgaarden F. S. et al., 2019, *MNRAS*, 490, 5228
- Brown G. E., 1995, *ApJ*, 440, 270
- Brumberg V. A., Zeldovich I. B., Novikov I. D., Shakura N. I., 1975, *SvA Lett.*, 1, 2
- Burrows A., Radice D., Vartanyan D., Nagakura H., Skinner M. A., Dolence J. C., 2020, *MNRAS*, 491, 2715
- Cai R.-G., Yang T., 2017, *Phys. Rev. D*, 95, 044024
- Campanelli M., Lousto C. O., Zlochower Y., 2006, *Phys. Rev. D*, 74, 041501
- Cao L., Lu Y., Zhao Y., 2018, *MNRAS*, 474, 4997
- Capela F., Pshirkov M., Tinyakov P., 2013, *Phys. Rev. D*, 87, 123524
- Chan C., Müller B., Heger A., 2020, *MNRAS*, 495, 3751
- Chattopadhyay D., Stevenson S., Hurley J. R., Rossi L. J., Flynn C., 2020, *MNRAS*, 494, 1587
- Chattopadhyay D., Stevenson S., Hurley J. R., Bailes M., Broekgaarden F., 2021, *MNRAS*, 504, 3682
- Chevalier R. A., 2012, *ApJ*, 752, L2
- Chruslinska M., Nelemans G., 2019, *MNRAS*, 488, 5300
- Chruslinska M., Belczynski K., Klencek J., Benacquista M., 2018, *MNRAS*, 474, 2937
- Chruslinska M., Nelemans G., Belczynski K., 2019, *MNRAS*, 482, 5012
- Clark J. S., Goodwin S. P., Crowther P. A., Kaper L., Fairbairn M., Langer N., Brocksopp C., 2002, *A&A*, 392, 909
- Clausen D., Sigurdsson S., Chernoff D. F., 2013, *MNRAS*, 428, 3618
- Clausen D., Sigurdsson S., Chernoff D. F., 2014, *MNRAS*, 442, 207
- Collette A., 2013, *Python and HDF5*. O’Reilly

- Costa G., Bressan A., Mapelli M., Marigo P., Iorio G., Spera M., 2021, *MNRAS*, 501, 4514
- Counselman Charles C. I., 1973, *ApJ*, 180, 307
- Cromartie H. T. et al., 2020, *Nature Astron.*, 4, 72
- Crowther P. A., 2007, *ARA&A*, 45, 177
- Darbha S., Kasen D., Foucart F., Price D. J., 2021, *ApJ*, 915, 69
- De Greve J. P., De Loore C., 1977, *Ap&SS*, 50, 75
- de Kool M., 1990, *ApJ*, 358, 189
- de Mink S. E., Belczynski K., 2015, *ApJ*, 814, 58
- de Mink S. E., Langer N., Izzard R. G., Sana H., de Koter A., 2013, *ApJ*, 764, 166
- Deaton M. B. et al., 2013, *ApJ*, 776, 47
- Delgado A. J., Thomas H. C., 1981, *A&A*, 96, 142
- Dewey R. J., Cordes J. M., 1987, *ApJ*, 321, 780
- Dewi J. D. M., Pols O. R., 2003, *MNRAS*, 344, 629
- Dewi J. D. M., Tauris T. M., 2000, *A&A*, 360, 1043
- Dewi J. D. M., Podsiadlowski P., Sena A., 2006, *MNRAS*, 368, 1742
- Di Carlo U. N., Mapelli M., Bouffanais Y., Giacobbo N., Santoliquido F., Bressan A., Spera M., Haardt F., 2020, *MNRAS*, 497, 1043
- Dobie D. et al., 2019, *ApJ*, 887, L13
- Dolan J. F., 2011, preprint ([arXiv:1107.1537](https://arxiv.org/abs/1107.1537))
- Dominik M., Belczynski K., Fryer C., Holz D. E., Berti E., Bulik T., Mandel I., O'Shaughnessy R., 2012, *ApJ*, 759, 52
- Dominik M., Belczynski K., Fryer C., Holz D. E., Berti E., Bulik T., Mandel I., O'Shaughnessy R., 2013, *ApJ*, 779, 72
- Dominik M. et al., 2015, *ApJ*, 806, 263
- Dooley K. L. et al., 2016, *Class. Quantum Gravity*, 33, 075009
- Downing J. M. B., Benacquista M. J., Giersz M., Spurzem R., 2010, *MNRAS*, 407, 1946
- Drozda P., Belczynski K., O'Shaughnessy R., Bulik T., Fryer C. L., 2020, preprint ([arXiv:2009.06655](https://arxiv.org/abs/2009.06655))
- Duchêne G., Kraus A., 2013, *ARA&A*, 51, 269
- Duez M. D., Foucart F., Kidder L. E., Ott C. D., Teukolsky S. A., 2010, *Class. Quantum Gravity*, 27, 114106
- Dunstall P. R. et al., 2015, *A&A*, 580, A93
- Eggleton P. P., Fitchett M. J., Tout C. A., 1989, *ApJ*, 347, 998
- Eichler D., Livio M., Piran T., Schramm D. N., 1989, *Nature*, 340, 126
- Eldridge J. J., Stanway E. R., 2016, *MNRAS*, 462, 3302
- Eldridge J. J., Stanway E. R., Tang P. N., 2019, *MNRAS*, 482, 870
- Eldridge J. J., Stanway E. R., Breivik K., Casey A. R., Steeghs D. T. H., Stence H. F., 2020, *MNRAS*, 495, 2786
- Ertl T., Woosley S. E., Sukhbold T., Janka H. T., 2020, *ApJ*, 890, 51
- Farmer R., Renzo M., de Mink S. E., Marchant P., Justham S., 2019, *ApJ*, 887, 53
- Farmer R., Renzo M., de Mink S. E., Fishbach M., Justham S., 2020, *ApJ*, 902, L36
- Farr W. M., Chatziioannou K., 2020, *Res. Notes Am. Astron. Soc.*, 4, 65
- Farr W., Sravan N., Cantrell A., Kreidberg L., Bailyn C., Mandel I., Kalogera V., 2011, in *APS April Meeting Abstracts*. p. H11.002
- Farr W. M., Stevenson S., Miller M. C., Mandel I., Farr B., Vecchio A., 2017, *Nature*, 548, 426
- Farrow N., Zhu X.-J., Thrane E., 2019, *ApJ*, 876, 18
- Feeney S. M., Peiris H. V., Nissanke S. M., Mortlock D. J., 2021, *Phys. Rev. Lett.*, 126, 171102
- Finn L. S., Chernoff D. F., 1993, *Phys. Rev. D*, 47, 2198
- Fishbach M., Holz D. E., 2017, *ApJ*, 851, L25
- Fishbach M., Kalogera V., 2021, *ApJ*, 914, L30
- Fishbach M., Holz D. E., Farr W. M., 2018, *ApJ*, 863, L41
- Flannery B. P., van den Heuvel E. P. J., 1975, *A&A*, 39, 61
- Foucart F., 2012, *Phys. Rev. D*, 86, 124007
- Foucart F., Hinderer T., Nissanke S., 2018, *Phys. Rev. D*, 98, 081501
- Fowler W. A., Hoyle F., 1964, *ApJS*, 9, 201
- Fragione G., Banerjee S., 2020, *ApJ*, 901, L16
- Fragione G., Loeb A., 2019a, *MNRAS*, 486, 4443
- Fragione G., Loeb A., 2019b, *MNRAS*, 490, 4991
- Fragione G., Pavlík V., Banerjee S., 2018, *MNRAS*, 480, 4955
- Fragione G., Grishin E., Leigh N. W. C., Perets H. B., Perna R., 2019, *MNRAS*, 488, 47
- Fragos T., McClintock J. E., 2015, *ApJ*, 800, 17
- Freiburghaus C., Rosswog S., Thielemann F. K., 1999, *ApJ*, 525, L121
- Freire P. C. C., Ransom S. M., Bégin S., Stairs I. H., Hessels J. W. T., Frey L. H., Camilo F., 2008, *ApJ*, 675, 670
- Fryer C. L., Kalogera V., 2001, *ApJ*, 554, 548
- Fryer C. L., Woosley S. E., Hartmann D. H., 1999, *ApJ*, 526, 152
- Fryer C. L., Belczynski K., Wiktorowicz G., Dominik M., Kalogera V., Holz D. E., 2012, *ApJ*, 749, 91
- Fryer C. L., Belczynski K., Ramirez-Ruiz E., Rosswog S., Shen G., Steiner A. W., 2015, *ApJ*, 812, 24
- Fuller J., Ma L., 2019, *ApJ*, 881, L1
- Furlong M. et al., 2015, *MNRAS*, 450, 4486
- Galaudage S., Talbot C., Thrane E., 2020, *Phys. Rev. D*, 102, 083026
- Ge H., Hjellming M. S., Webbink R. F., Chen X., Han Z., 2010, *ApJ*, 717, 724
- Ge H., Webbink R. F., Chen X., Han Z., 2015, *ApJ*, 812, 40
- Gennaro M. et al., 2018, *ApJ*, 855, 20
- Gerosa D., Berti E., O'Shaughnessy R., Belczynski K., Kesden M., Wysocki D., Gladysz W., 2018, *Phys. Rev. D*, 98, 084036
- Gessner A., Janka H.-T., 2018, *ApJ*, 865, 61
- Giacobbo N., Mapelli M., 2018, *MNRAS*, 480, 2011
- Giacobbo N., Mapelli M., Spera M., 2018, *MNRAS*, 474, 2959
- Goldberg D., Mazeh T., 1994, *A&A*, 282, 801
- Gomez S. et al., 2019, *ApJ*, 884, L55
- Gompertz B. P., Levan A. J., Tanvir N. R., 2020, *ApJ*, 895, 58
- Goodman J., 1986, *ApJ*, 308, L47
- Goriely S., Bauswein A., Janka H.-T., 2011, *ApJ*, 738, L32
- Götberg Y., de Mink S. E., Groh J. H., Kupfer T., Crowther P. A., Zapartas E., Renzo M., 2018, *A&A*, 615, A78
- Hamann W. R., Koesterke L., 1998, *A&A*, 335, 1003
- Hamers A. S., Thompson T. A., 2019, *ApJ*, 883, 23
- Han M.-Z., Tang S.-P., Hu Y.-M., Li Y.-J., Jiang J.-L., Jin Z.-P., Fan Y.-Z., Wei D.-M., 2020, *ApJ*, 891, L5
- Hannam M., Schmidt P., Bohé A., Haegel L., Husa S., Ohme F., Pratten G., Pürrer M., 2014, *Phys. Rev. Lett.*, 113, 151101
- Harris C. R. et al., 2020, *Nature*, 585, 357–362
- Hayashi C., Nakano T., 1963, *Prog. Theor. Phys.*, 30, 460
- Hinshaw G. et al., 2013, *ApJS*, 208, 19
- Hoang B.-M., Naoz S., Kremer K., 2020, *ApJ*, 903, 8
- Hobbs G., Lorimer D. R., Lyne A. G., Kramer M., 2005, *MNRAS*, 360, 974
- Hogg D. W., 1999, preprint ([arXiv:astro-ph/9905116](https://arxiv.org/abs/astro-ph/9905116))
- Hotokezaka K., Piran T., 2015, *MNRAS*, 450, 1430
- Hotokezaka K., Nissanke S., Hallinan G., Lazio T. J. W., Nakar E., Piran T., 2016, *ApJ*, 831, 190
- Huang K., Hu J., Zhang Y., Shen H., 2020, *ApJ*, 904, 39
- Humphreys R. M., Davidson K., 1994, *PASP*, 106, 1025
- Hunter J. D., 2007, *Comput. Sci. Eng.*, 9, 90
- Hurley J. R., Pols O. R., Tout C. A., 2000, *MNRAS*, 315, 543
- Hurley J. R., Tout C. A., Pols O. R., 2002, *MNRAS*, 329, 897
- Husa S., Khan S., Hannam M., Pürrer M., Ohme F., Forteza X. J., Bohé A., 2016, *Phys. Rev. D*, 93, 044006
- Igoshev A. P., 2020, *MNRAS*, 494, 3663
- Ivanova N., Taam R. E., 2004, *ApJ*, 601, 1058
- Ivanova N., Heinke C. O., Rasio F. A., Belczynski K., Fregeau J. M., 2008, *MNRAS*, 386, 553
- Ivanova N. et al., 2013, *A&A Rev.*, 21, 59
- Janka H.-T., 2013, *MNRAS*, 434, 1355
- Just O., Bauswein A., Ardevol Pulpillo R., Goriely S., Janka H. T., 2015, *MNRAS*, 448, 541
- Justham S., Podsiadlowski P., Han Z., 2011, *MNRAS*, 410, 984
- Kalogera V., Baym G., 1996, *ApJ*, 470, L61
- Kasen D., Metzger B., Barnes J., Quataert E., Ramirez-Ruiz E., 2017, *Nature*, 551, 80
- Katz J. I., 1975, *Nature*, 253, 698
- Kawaguchi K., Shibata M., Tanaka M., 2020, *ApJ*, 893, 153
- Khan S., Husa S., Hannam M., Ohme F., Pürrer M., Forteza X. J., Bohé A., 2016, *Phys. Rev. D*, 93, 044007

- Kimball C. et al., 2021, *ApJ*, 915, L35
- Kippenhahn R., Weigert A., 1967, *ZAp*, 65, 251
- Kiziltan B., Kottas A., De Yoreo M., Thorsett S. E., 2013, *ApJ*, 778, 66
- Klencki J., Nelemans G., 2019, *IAU Symp.*, 346, 417
- Klencki J., Moe M., Gladysz W., Chruslinska M., Holz D. E., Belczynski K., 2018, *A&A*, 619, A77
- Klencki J., Nelemans G., Istrate A. G., Pols O., 2020, *A&A*, 638, A55
- Kluiver T. et al., 2016, in *ELPUB*. p. 87
- Kobulnicky H. A., Fryer C. L., 2007, *ApJ*, 670, 747
- Kobulnicky H. A. et al., 2014, *ApJS*, 213, 34
- Kochanek C. S., 2014, *ApJ*, 785, 28
- Kowalska-Leszczynska I., Regimbau T., Bulik T., Dominik M., Belczynski K., 2015, *A&A*, 574, A58
- Kramer M., Backer D., Cordes J., Lazio T., Stappers B., Johnston S., 2004, *New Astron. Rev.*, 48, 993
- Kreidberg L., Bailyn C. D., Farr W. M., Kalogera V., 2012, *ApJ*, 757, 36
- Kremer K. et al., 2020, *ApJ*, 903, 45
- Kroupa P., 2001, *MNRAS*, 322, 231
- Kruckow M. U., Tauris T. M., Langer N., Szécsi D., Marchant P., Podsiadlowski P., 2016, *A&A*, 596, A58
- Kruckow M. U., Tauris T. M., Langer N., Kramer M., Izzard R. G., 2018, *MNRAS*, 481, 1908
- Kushnir D., Zaldarriaga M., Kollmeier J. A., Waldman R., 2016, *MNRAS*, 462, 844
- Kyutoku K., Kiuchi K., Sekiguchi Y., Shibata M., Taniguchi K., 2018, *Phys. Rev. D*, 97, 023009
- Kyutoku K., Fujibayashi S., Hayashi K., Kawaguchi K., Kiuchi K., Shibata M., Tanaka M., 2020, *ApJ*, 890, L4
- Lackey B. D., Kyutoku K., Shibata M., Brady P. R., Friedman J. L., 2012, *Phys. Rev. D*, 85, 044061
- Lamberts A. et al., 2018, *MNRAS*, 480, 2704
- Langer N., Norman C. A., 2006, *ApJ*, 638, L63
- Laplace E., Götzberg Y., de Mink S. E., Justham S., Farmer R., 2020, *A&A*, 637, A6
- Lattimer J. M., Schramm D. N., 1974, *ApJ*, 192, L145
- Lattimer J. M., Schramm D. N., 1976, *ApJ*, 210, 549
- Lauterborn D., 1970, *A&A*, 7, 150
- Lawrence S., Tervala J. G., Bedaque P. F., Miller M. C., 2015, *ApJ*, 808, 186
- LIGO Scientific Collaboration, 2015, *Class. Quantum Gravity*, 32, 074001
- LIGO Scientific Collaboration, 2018, LIGO Algorithm Library - LALSuite, free software (GPL). Available at <https://git.ligo.org/lscsoft/lalsuite>
- Li L.-X., Paczyński B., 1998, *ApJ*, 507, L59
- Linares M., 2020, in *Multifrequency Behaviour of High Energy Cosmic Sources - XIII*. 3-8 June 2019, Palermo. p. 23
- Lipunov V. M., Postnov K. A., 1987, *SvA*, 31, 228
- Lück H. et al., 2010, *J. Phys. Conf. Ser.*, 228, 012012
- Lyne A. G., Lorimer D. R., 1994, *Nature*, 369, 127
- Ma X., Hopkins P. F., Faucher-Giguère C.-A., Zolman N., Muratov A. L., Kereš D., Quataert E., 2016, *MNRAS*, 456, 2140
- Madau P., Dickinson M., 2014, *ARA&A*, 52, 415
- Madau P., Fragos T., 2017, *ApJ*, 840, 39
- Maeder A., 1992, *A&A*, 264, 105
- Mandel I., 2016, *MNRAS*, 456, 578
- Mandel I., Broekgaarden F. S., 2021, preprint ([arXiv:2107.14239](https://arxiv.org/abs/2107.14239))
- Mandel I., de Mink S. E., 2016, *MNRAS*, 458, 2634
- Mandel I., Farmer A., 2018, preprint ([arXiv:1806.05820](https://arxiv.org/abs/1806.05820))
- Mandel I., Fragos T., 2020, *ApJ*, 895, L28
- Mandel I., Müller B., 2020, *MNRAS*, 499, 3214
- Mandel I., O’Shaughnessy R., 2010, *Class. Quantum Gravity*, 27, 114007
- Mandel I., Müller B., Riley J., de Mink S. E., Vigna-Gómez A., Chattopadhyay D., 2021, *MNRAS*, 500, 1380
- Mapelli M., 2016, *MNRAS*, 459, 3432
- Mapelli M., Giacobbo N., 2018, *MNRAS*, 479, 4391
- Mapelli M., Giacobbo N., Ripamonti E., Spera M., 2017, *MNRAS*, 472, 2422
- Mapelli M., Giacobbo N., Santoliquido F., Artale M. C., 2019, *MNRAS*, 487, 2
- Marchant P., Langer N., Podsiadlowski P., Tauris T. M., de Mink S., Mandel I., Moriya T. J., 2017, *A&A*, 604, A55
- Marchant P., Renzo M., Farmer R., Pappas K. M. W., Taam R. E., de Mink S. E., Kalogera V., 2019, *ApJ*, 882, 36
- Margalit B., Metzger B. D., 2017, *ApJ*, 850, L19
- Martynov D. V. et al., 2016, *Phys. Rev. D*, 93, 112004
- Massevitch A., Yungelson L., 1975, *Mem. Soc. Astron. Italiana*, 46, 217
- Mazeh T., Goldberg D., Duquennoy A., Mayor M., 1992, *ApJ*, 401, 265
- McKernan B., Ford K. E. S., O’Shaughnessy R., 2020, *MNRAS*, 498, 4088
- Mennekens N., Vanbeveren D., 2016, *A&A*, 589, A64
- Metzger B. D., 2017, *Living Rev. Relativ.*, 20, 3
- Metzger B. D., Berger E., 2012, *ApJ*, 746, 48
- Miller M. C., Miller J. M., 2015, *Phys. Rep.*, 548, 1
- Miller M. C. et al., 2019, *ApJ*, 887, L24
- Miyaji S., Nomoto K., Yokoi K., Sugimoto D., 1980, *PASJ*, 32, 303
- Moe M., Di Stefano R., 2017, *ApJS*, 230, 15
- Moriya T. J. et al., 2017, *MNRAS*, 466, 2085
- Müller B., Heger A., Liptai D., Cameron J. B., 2016, *MNRAS*, 460, 742
- Müller B., Gay D. W., Heger A., Tauris T. M., Sim S. A., 2018, *MNRAS*, 479, 3675
- Nakar E., Piran T., 2011, *Nature*, 478, 82
- Neijssel C. J. et al., 2019, *MNRAS*, 490, 3740
- Nelemans G., Tauris T. M., van den Heuvel E. P. J., 1999, *A&A*, 352, L87
- Nissanke S., Holz D. E., Hughes S. A., Dalal N., Sievers J. L., 2010, *ApJ*, 725, 496
- Nitz A. H. et al., 2020, *ApJ*, 891, 123
- Nomoto K., 1984, *ApJ*, 277, 791
- Nomoto K., 1987, *ApJ*, 322, 206
- O’Leary R. M., Kocsis B., Loeb A., 2009, *MNRAS*, 395, 2127
- O’Shaughnessy R., Kalogera V., Belczynski K., 2010, *ApJ*, 716, 615
- Olejak A., Fishbach M., Belczynski K., Holz D. E., Lasota J. P., Miller M. C., Bulik T., 2020, *ApJ*, 901, L39
- Olejak A., Belczynski K., Ivanova N., 2021, *A&A*, 651, A100
- Öpik E., 1924, *Publ. Tartu Astrofizika Obs.*, 25, 1
- Özel F., Freire P., 2016, *ARA&A*, 54, 401
- Özel F., Psaltis D., Narayan R., McClintock J. E., 2010, *ApJ*, 725, 1918
- Özel F., Psaltis D., Narayan R., Santos Villarreal A., 2012, *ApJ*, 757, 55
- Paczynski B., 1986, *ApJ*, 308, L43
- Paczyński B., Sienkiewicz R., 1972, *AcA*, 22, 73
- Pan Y., Buonanno A., Taracchini A., Kidder L. E., Mroué A. H., Pfeiffer H. P., Scheel M. A., Szilágyi B., 2014, *Phys. Rev. D*, 89, 084006
- Pani P., Loeb A., 2014, *J. Cosmology Astropart. Phys.*, 2014, 028
- Pannarale F., Ohme F., 2014, *ApJ*, 791, L7
- Pannarale F., Tonita A., Rezzolla L., 2011, *ApJ*, 727, 95
- Panter B., Heavens A. F., Jimenez R., 2004, *MNRAS*, 355, 764
- Pavlovskii K., Ivanova N., 2015, *MNRAS*, 449, 4415
- Pavlovskii K., Ivanova N., Belczynski K., Van K. X., 2017, *MNRAS*, 465, 2092
- Pejcha O., Thompson T. A., 2015, *ApJ*, 801, 90
- Pejcha O., Metzger B. D., Tomida K., 2016, *MNRAS*, 455, 4351
- Perez F., Granger B. E., 2007, *Comput. Sci. Eng.*, 9, 21
- Peters P. C., 1964, *Phys. Rev.*, 136, 1224
- Pfahl E., Rappaport S., Podsiadlowski P., 2002, *ApJ*, 571, L37
- Pfahl E., Podsiadlowski P., Rappaport S., 2005, *ApJ*, 628, 343
- Piran T., Nakar E., Rosswog S., 2013, *MNRAS*, 430, 2121
- Podsiadlowski P., Langer N., Poelarends A. J. T., Rappaport S., Heger A., Pfahl E., 2004, *ApJ*, 612, 1044
- Pols O., Hurley J., Tout C., 1998, in *IAU Symp.* p. 607
- Portegies Zwart S. F., McMillan S. L. W., 2000, *ApJ*, 528, L17
- Qin Y., Fragos T., Meynet G., Andrews J., Sørensen M., Song H. F., 2018, *A&A*, 616, A28
- Rastello S., Mapelli M., Di Carlo U. N., Giacobbo N., Santoliquido F., Spera M., Ballone A., Iorio G., 2020, *MNRAS*, 497, 1563
- Renzo M. et al., 2019, *A&A*, 624, A66
- Renzo M., Farmer R. J., Justham S., de Mink S. E., Götzberg Y., Marchant P., 2020, *MNRAS*, 493, 4333
- Repetto S., Nelemans G., 2015, *MNRAS*, 453, 3341
- Repetto S., Davies M. B., Sigurdsson S., 2012, *MNRAS*, 425, 2799
- Rodríguez C. L., Chatterjee S., Rasio F. A., 2016, *Phys. Rev. D*, 93, 084029
- Román-Garza J. et al., 2021, *ApJ*, 912, L23

- Rosswog S., Liebendörfer M., Thielemann F. K., Davies M. B., Benz W., Piran T., 1999, *A&A*, 341, 499
- Roulet J., Zalzarriaga M., 2019, *MNRAS*, 484, 4216
- Rude G., Orosz J. A., McClintock J. E., Torres M. A. P., 2010, in *American Astronomical Society Meeting Abstracts #215*. p. 419.05
- Safarzadeh M., Berger E., Leja J., Speagle J. S., 2019, *ApJ*, 878, L14
- Samsing J., Hotokezaka K., 2020, preprint ([arXiv:2006.09744](https://arxiv.org/abs/2006.09744))
- Sana H., 2017, in *Eldridge J. J., Bray J. C., McClelland L. A. S., Xiao L., eds, Proc. IAU Symp. 329, The Lives and Death-Throes of Massive Stars*. p. 110
- Sana H., Evans C. J., 2011, in *Neiner C., Wade G., Meynet G., Peters G., eds, Proc. IAU Symp. 272, Active OB Stars: Structure, Evolution, Mass Loss, and Critical Limits*. p. 474
- Sana H. et al., 2012, *Science*, 337, 444
- Santoliquido F., Mapelli M., Bouffanais Y., Giacobbo N., Di Carlo U. N., Rastello S., Artale M. C., Ballone A., 2020, *ApJ*, 898, 152
- Santoliquido F., Mapelli M., Giacobbo N., Bouffanais Y., Artale M. C., 2021, *MNRAS*, 502, 4877
- Sarin N., Lasky P. D., Ashton G., 2020, *Phys. Rev. D*, 101, 063021
- Savaglio S. et al., 2005, *ApJ*, 635, 260
- Schechter P., 1976, *ApJ*, 203, 297
- Scheel M. A., Giesler M., Hemberger D. A., Lovelace G., Kuper K., Boyle M., Szilágyi B., Kidder L. E., 2015, *Class. Quantum Gravity*, 32, 105009
- Schneider F. R. N., Izzard R. G., Langer N., de Mink S. E., 2015, *ApJ*, 805, 20
- Schneider F. R. N. et al., 2018, *Science*, 359, 69
- Schröder S. L., MacLeod M., Loeb A., Vigna-Gómez A., Mandel I., 2020, *ApJ*, 892, 13
- Schutz B. F., 1986, *Nature*, 323, 310
- Schwab J., Podsiadlowski P., Rappaport S., 2010, *ApJ*, 719, 722
- Secunda A. et al., 2020, *ApJ*, 903, 133
- Sigurdsson S., 2003, in *Bailes M., Nice D. J., Thorsett S. E., eds, ASP Conf. Ser. Vol. 302, Radio Pulsars*. Astron. Soc. Pac., San Francisco, p. 391
- Silsbee K., Tremaine S., 2017, *ApJ*, 836, 39
- Smarr L. L., Blandford R., 1976, *ApJ*, 207, 574
- Soberman G. E., Phinney E. S., van den Heuvel E. P. J., 1997, *A&A*, 327, 620
- Somiya K., 2012, *Class. Quantum Gravity*, 29, 124007
- Spera M., Mapelli M., 2017, *MNRAS*, 470, 4739
- Spera M., Mapelli M., Giacobbo N., Trani A. A., Bressan A., Costa G., 2019, *MNRAS*, 485, 889
- Srinivasan G., 1989, *A&A Rev.*, 1, 209
- Stephan A. P. et al., 2019, *ApJ*, 878, 58
- Stevenson S., Vigna-Gómez A., Mandel I., Barrett J. W., Neijssel C. J., Perkins D., de Mink S. E., 2017a, *Nature Commun.*, 8, 14906
- Stevenson S., Berry C. P. L., Mandel I., 2017b, *MNRAS*, 471, 2801
- Stevenson S., Sampson M., Powell J., Vigna-Gómez A., Neijssel C. J., Szécsi D., Mandel I., 2019, *ApJ*, 882, 121
- Strolger L.-G. et al., 2004, *ApJ*, 613, 200
- Suwa Y., Yoshida T., Shibata M., Umeda H., Takahashi K., 2015, *MNRAS*, 454, 3073
- Taam R. E., Sandquist E. L., 2000, *ARA&A*, 38, 113
- Talbot C., Thrane E., 2018, *ApJ*, 856, 173
- Tang P. N., Eldridge J. J., Stanway E. R., Bray J. C., 2020, *MNRAS*, 493, L6
- Tauris T. M., Dewi J. D. M., 2001, *A&A*, 369, 170
- Tauris T. M., Takens R. J., 1998, *A&A*, 330, 1047
- Tauris T. M., van den Heuvel E. P. J., 2006, *Formation and evolution of compact stellar X-ray sources*. Cambridge Univ. Press, Cambridge, UK, p. 623
- Tauris T. M., Langer N., Moriya T. J., Podsiadlowski P., Yoon S. C., Blinnikov S. I., 2013, *ApJ*, 778, L23
- Tauris T. M., Langer N., Podsiadlowski P., 2015, *MNRAS*, 451, 2123
- Tauris T. M. et al., 2017, *ApJ*, 846, 170
- Taylor S. R., Gerosa D., 2018, *Phys. Rev. D*, 98, 083017
- Team COMPAS, 2021, preprint ([arXiv:2109.10352](https://arxiv.org/abs/2109.10352)) (C21)
- Thompson T. A. et al., 2019, *Science*, 366, 637
- Thorne K. S., Zytkov A. N., 1977, *ApJ*, 212, 832
- Timmes F. X., Woosley S. E., Weaver T. A., 1996, *ApJ*, 457, 834
- Tout C. A., 1991, *MNRAS*, 250, 701
- Tout C. A., Pols O. R., Eggleton P. P., Han Z., 1996, *MNRAS*, 281, 257
- Tout C. A., Aarseth S. J., Pols O. R., Eggleton P. P., 1997, *MNRAS*, 291, 732
- Troja E., King A. R., O'Brien P. T., Lyons N., Cusumano G., 2008, *MNRAS*, 385, L10
- Tutukov A. V., Yungel' Son L. R., 1993a, *Astron. Rep.*, 37, 411
- Tutukov A. V., Yungelson L. R., 1993b, *MNRAS*, 260, 675
- Tutukov A. V., Yungelson L. R., 1994, *MNRAS*, 268, 871
- Valentim R., Rangel E., Horvath J. E., 2011, *MNRAS*, 414, 1427
- van den Heuvel E. P. J., De Loore C., 1973, *A&A*, 25, 387
- van den Heuvel E. P. J., Yoon S. C., 2007, *Ap&SS*, 311, 177
- van den Heuvel E. P. J., Portegies Zwart S. F., de Mink S. E., 2017, *Mon. Not. Roy. Astron. Soc.*, 471, 4256
- van Kerkwijk M. H., Breton R. P., Kulkarni S. R., 2011, *ApJ*, 728, 95
- van Rossum G., 1995, *Technical Report CS-R9526, Python tutorial*. Centrum voor Wiskunde en Informatica (CWI), Amsterdam
- van Son L. A. C. et al., 2020, *ApJ*, 897, 100
- Venumadhav T., Zackay B., Roulet J., Dai L., Zalzarriaga M., 2020, *Phys. Rev. D*, 101, 083030
- Verbunt F., Cator E., 2017, *JA&A*, 38, 40
- Verbunt F., Phinney E. S., 1995, *A&A*, 296, 709
- Verbunt F., Igoshev A., Cator E., 2017, *A&A*, 608, A57
- Vigna-Gómez A. et al., 2018, *MNRAS*, 481, 4009
- Vigna-Gómez A. et al., 2020, *PASA*, 37, e038
- Vigna-Gómez A., Schröder S. L., Ramirez-Ruiz E., Aguilera-Dena D. R., Batta A., Langer N., Wilcox R., 2021a, preprint ([arXiv:2106.12381](https://arxiv.org/abs/2106.12381))
- Vigna-Gómez A., Toonen S., Ramirez-Ruiz E., Leigh N. W. C., Riley J., Haster C.-J., 2021b, *ApJ*, 907, L19
- Vinciguerra S. et al., 2020, *MNRAS*, 498, 4705
- Vink J. S., de Koter A., 2005, *A&A*, 442, 587
- Vink J. S., de Koter A., Lamers H. J. G. L. M., 2000, *A&A*, 362, 295
- Vink J. S., de Koter A., Lamers H. J. G. L. M., 2001, *A&A*, 369, 574
- Virtanen P. et al., 2020, *Nature Methods*, 17, 261
- Vitale S., Chen H.-Y., 2018, *Phys. Rev. Lett.*, 121, 021303
- Vitale S., Lynch R., Sturani R., Graff P., 2017, *Class. Quantum Gravity*, 34, 03LT01
- Voss R., Tauris T. M., 2003, *MNRAS*, 342, 1169
- Waskom M., the seaborn development team, 2020, *mwaskom/seaborn*. Available at <https://doi.org/10.5281/zenodo.592845>
- Webbink R. F., 1984, *ApJ*, 277, 355
- Wes McKinney, 2010, in *van der Walt S., Millman J., eds, Proceedings of the 9th Python in Science Conference*. p. 56
- Wex N., 2014, preprint ([arXiv:1402.5594](https://arxiv.org/abs/1402.5594))
- Wex N., Kopeikin S., 1999, *Astrophys. J.*, 514, 388
- Whyte C. A., Eggleton P. P., 1985, *MNRAS*, 214, 357
- Wiktorowicz G., Wyrzykowski Ł., Chruslinska M., Klencki J., Rybicki K. A., Belczynski K., 2019, *ApJ*, 885, 1
- Wong K. W. K., Gerosa D., 2019, *Phys. Rev. D*, 100, 083015
- Wong K. W. K., Breivik K., Kremer K., Callister T., 2021, *Phys. Rev. D*, 103, 083021
- Wongwathanarat A., Janka H. T., Müller E., 2013, *A&A*, 552, A126
- Woosley S. E., 2017, *ApJ*, 836, 244
- Woosley S. E., 2019, *ApJ*, 878, 49
- Woosley S. E., Heger A., 2021, *ApJ*, 912, L31
- Woosley S. E., Weaver T. A., 1995, *ApJS*, 101, 181
- Woosley S. E., Heger A., Weaver T. A., 2002, *Rev. Mod. Phys.*, 74, 1015
- Wyrzykowski Ł., Mandel I., 2020, *A&A*, 636, A20
- Wyrzykowski Ł. et al., 2016, *MNRAS*, 458, 3012
- Wysocki D., Gerosa D., O'Shaughnessy R., Belczynski K., Gładysz W., Berti E., Kesden M., Holz D. E., 2018, *Phys. Rev. D*, 97, 043014
- Wysocki D., Lange J., O'Shaughnessy R., 2019, *Phys. Rev. D*, 100, 043012
- Xu X.-J., Li X.-D., 2010a, *ApJ*, 716, 114
- Xu X.-J., Li X.-D., 2010b, *ApJ*, 722, 1985
- Yang Y., Gayathri V., Bartos I., Haiman Z., Safarzadeh M., Tagawa H., 2020, *ApJ*, 901, L34
- Ye C. S., Kremer K., Chatterjee S., Rodriguez C. L., Rasio F. A., 2019, *ApJ*, 877, 122

- Ye C. S., Fong W.-f., Kremer K., Rodriguez C. L., Chatterjee S., Fragione G., Rasio F. A., 2020, *ApJ*, 888, L10
- Zackay B., Dai L., Venumadhav T., Roulet J., Zaldarriaga M., 2019a, preprint (arXiv:1910.09528)
- Zackay B., Venumadhav T., Dai L., Roulet J., Zaldarriaga M., 2019b, *Phys. Rev. D*, 100, 023007
- Zahn J. P., 1977, *A&A*, 500, 121
- Zahn J. P., 2008, in Goupil M. J., Zahn J. P., eds, EAS Publications Series Vol. 29, Tidal dissipation in binary systems. EDP Sciences, p. 67
- Zappa F., Bernuzzi S., Pannarale F., Mapelli M., Giacobbo N., 2019, *Phys. Rev. Lett.*, 123, 041102
- Zdziarski A. A., Mikolajewska J., Belczynski K., 2013, *MNRAS*, 429, L104
- Zevin M. et al., 2020a, *ApJ*, 910, 152
- Zevin M., Spera M., Berry C. P. L., Kalogera V., 2020b, *ApJ*, 899, L1
- Zhou X., Li A., Li B.-A., 2020, *ApJ*, 910, 62
- Zhu J.-P. et al., 2020, *ApJ*, 917, 24
- Ziosi B. M., Mapelli M., Branchesi M., Tormen G., 2014, *MNRAS*, 441, 3703

APPENDIX A: CALCULATING THE COSMOLOGICAL MERGER RATES

In practice we approximate the integral in equation (4) with the Monte Carlo estimate

$$\mathcal{R}_{\text{det}} = \sum_{z_m^j} \sum_{z_i^k} \left(\int_0^{t_m^j} dt_{\text{delay}} \mathcal{R}_{\text{form}}(Z_i^k, t_{\text{delay}}) \text{SFRD}(Z_i^k, z_{\text{form}}) \right) \times \frac{D_c^2(z_m^j)}{E(z_m^j)} \frac{1}{1+z_m^j} \frac{4\pi c}{\mathcal{H}_0} P_{\text{det}}(m_{1,f}, m_{2,f}, z_m^j) \Delta z_m^j \Delta Z^k, \quad (\text{A1})$$

where we sum over 100 equally divided redshift bins $z_m^j \in [0, z_{\text{max}}]$ where we choose $z_{\text{max}} = 6$, which is a conservative upper limit for the maximum redshift out to which DCOs are detectable with an LVK GW network at design sensitivity¹²; see fig. 3 of Martynov et al. 2016, the last columns of tables 3 and 4 of Belczynski et al. (2020) and Abbott et al. 2018a. We also sum over our 53 metallicity bins Z_i^k distributed approximately log-uniform in the range of 0.0001–0.03,

¹² $z = 0.50$ is equal to a luminosity distance of $D_L \approx 3 \cdot 10^3$ Mpc.

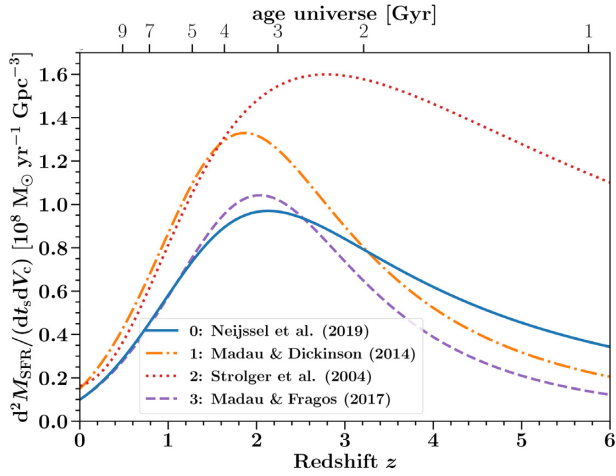
corresponding to the Z_i range in Hurley et al. (2000). The metallicity grid points are shown with black scatter points in Fig. 5. We use t_m^j as short-hand notation for $t_m(z_m^j)$, the merger time at redshift z_m^j , and also write the short-hand notation $\Delta z_m^j = (z_m^{j+1} - z_m^j)$ and $\Delta Z_i^k = (Z_i^{k+1} - Z_i^k)$. We also use z_{form} as a short-hand notation for $z(t_{\text{form}} = t_{\text{delay}} - t_m^j)$. D_c and E are functions of redshift given in Hogg (1999) and \mathcal{H}_0 is the Hubble constant at redshift $z = 0$.

APPENDIX B: METALLICITY-SPECIFIC STAR FORMATION RATE PRESCRIPTIONS

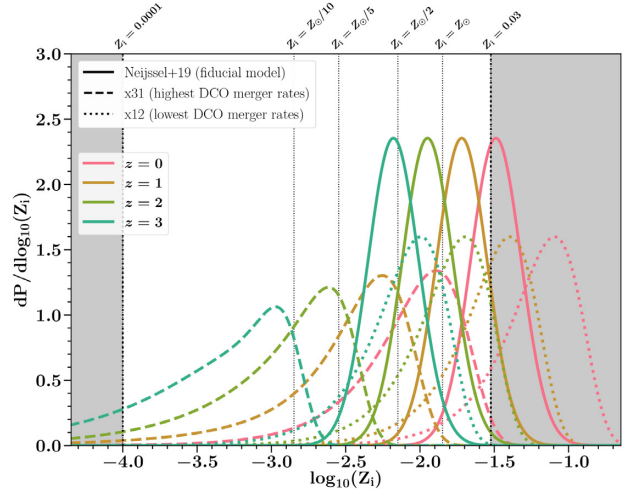
In Fig. B1 we show the distributions of the prescriptions that build up our SFRD(Z_i, z) models in more detail. As discussed in Section 2.3 (and schematically shown in Fig. 2), we construct our 28 SFRD(Z_i, z) models from an SFRD and metallicity distribution function dP/dZ_i . The 28 ($3 \times 3 + 1$) combinations are summarized in Table 3.

Fig. B1(a) shows the used SFRD prescriptions. It can be seen that the Madau & Fragos (2017) and Neijssel et al. (2019) SFRDs prescriptions give lower yields, particularly for redshifts $z \lesssim 3$, compared to the Madau & Dickinson (2014) and Strolger et al. (2004) SFRD. These lower SFRD yields lead to lower predicted merger rates as discussed in Section 4.

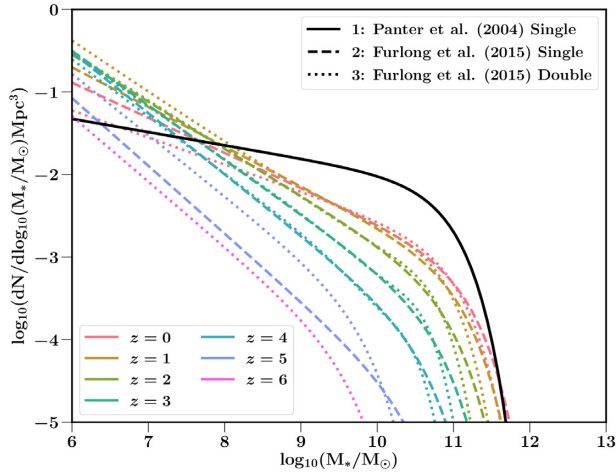
Fig. B1(b) shows three examples of metallicity distributions dP/dZ_i . In all models except our SFRD(Z_i, z) model xyz = 000, the metallicity distribution function is created from convolving a GSMF with an MZR. In model xyz = 000, the dP/dZ_i is constructed from a phenomenological model as presented in Neijssel et al. (2019). The Neijssel et al. (2019) phenomenological metallicity distribution function is shown in solid lines. The metallicity prescriptions yz = 31 (dashed lines) and yz = 12 (dotted lines) are shown as example. These prescriptions correspond to the metallicity distribution models with our Furlong et al. (2015) GSMF and Langer & Norman (2006) MZR and our Panter et al. (2004) GSMF and Langer & Norman (2006) + offset MZR. Section 4 shows that these result in the highest and lowest BHNS merger rates, respectively. The grey areas in the figure show Z_i values outside our modelled metallicity grid (see Table 1). Parts of the metallicity distribution function that fall outside of the Z_i parameter range are added to the edge bins when integrating over metallicities in equation (A1). Fig. B1(c) shows our explored GSMFs, whereas Fig. B1(d) shows our three explored MZRs. See for more details Neijssel et al. (2019).



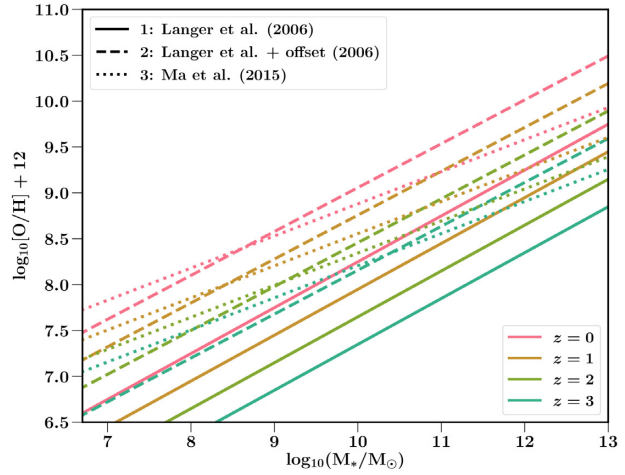
(a) The four different star formation rate density (SFRD) prescriptions studied in this work.



(b) Three examples of metallicity probability distribution functions (dP/dZ_i) used in this work. For each of the prescriptions the metallicity distribution is shown for four different redshifts.



(c) The three different galaxy stellar mass function (GSMF) prescriptions studied in this work shown at seven different redshifts.



(d) The three different Mass-metallicity relation (MZR) prescriptions studied in this work shown at four different redshifts.

Figure B1. Figures showing the components that construct the metallicity-specific star formation rate densities (SFRD(Z_i, z)) that are used in this study. From left to right and top to bottom we show: (a) the SFRDs, (b) the metallicity distributions dP/dZ_i , (c) the GSMFs, and (d) the MZRs. See for more details Table 3 and Section 2.3.

APPENDIX C: ZOOM IN ON FIGURE 15

In Fig. C1, we give a zoom-in of Fig. 15 to show the SFRD(Z_i, z) models that correspond with each bar. The order of the bars, and hence SFRD(Z_i, z) models, is the same throughout all model blocks in Fig. 15.

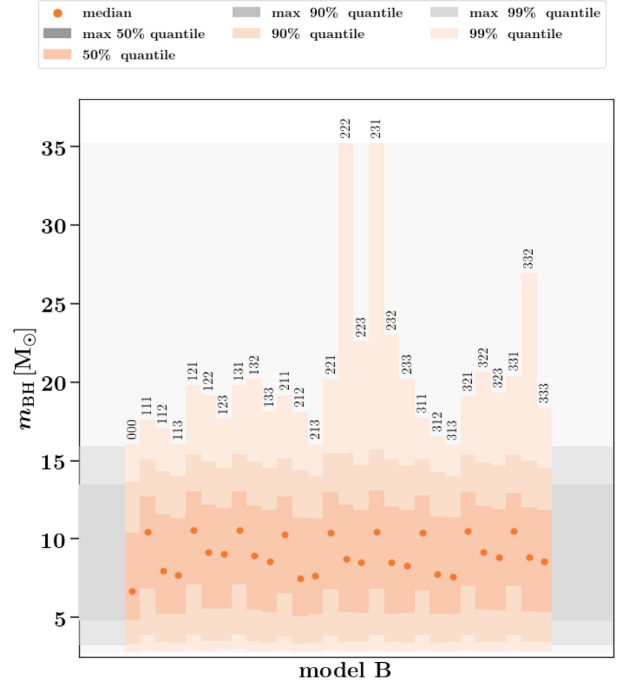


Figure C1. A zoom in of Fig. 15 showing the distribution quantiles for the BH mass distribution for all 28 SFRD(Z_i, z) model variations in combination with the binary population synthesis model B. The figure highlights the SFRD(Z_i, z) bars, adding the SFRD(Z_i, z) label denoted by xyz (see Table 3) on top of the corresponding bar. Coloured bars from dark to light denote the distribution quantiles for 50 per cent, 90 per cent, and 99 per cent of the distribution. Scatter points show the median values of the distribution. In the background, the maximum range of the 50 per cent, 90 per cent, and 99 per cent quantiles over all 420 model variations is shown.

This paper has been typeset from a $\text{\TeX}/\text{\LaTeX}$ file prepared by the author.